AN ABSTRACT OF THE DISSERTATION OF

Eric M. Becker for the degree of Doctor of Philosophy in Radiation Health Physics presented on December 7, 2015.

Title: A Direction-Sensitive Radiation Detector for Low-Altitude, UAV-based Radiological Source Search

Abstract approved: _____

Abi T. Farsoni

Many devices and methods for radiological searches are currently being developed, including scanning using simple detectors, mapping using large-volume detectors, and Compton imaging using 3-D position sensitive detectors. However, these devices are typically expensive and the methods used require long periods of time to generate a direction or location. The Radiation Compass, currently being developed at Oregon State University, is a low-cost detector designed for dynamic use on an unmanned aerial vehicle (UAV) and will generate a most probable source direction that will be used to guide the motion of the UAV. The prototype detection system is composed of sixteen detection elements based on a BGO crystal coupled to a SiPM and arranged in a circular array. A specific detector response pattern of radiation count rates is generated based on the passive masking of detection elements on opposite sides of the array, and each of the detector panels is able to

rotate to optimize its efficiency with respect to the Radiation Compass altitude. Three direction estimation methods were investigated and used to study the performance of the Radiation Compass. The Radiation Compass is able to detect the presence of a 10 µCi ^{137}Cs source in under 8 seconds with 95% confidence at a background rate of 25.5 counts per second at ground level at a distance of 100 cm from the center of the Radiation Compass. The device also achieved an an accuracy of 1.8° and a 95% confidence width of 8.6° for a 12.3 µCi ^{137}Cs source in 60 seconds at ground level, at a background rate of 13.12 counts per second, and a distance of 100 cm from the center of the detector.

A Direction-Sensitive Radiation Detector for Low-Altitude,
UAV-based Radiological Source Search

by

Eric M. Becker

A DISSERTATION

submitted to

Oregon State University

in partial fulfillment of
the requirements for the
degree of

Doctor of Philosophy

Presented December 7, 2015
Commencement June 2016

Doctor of Philosophy dissertation of Eric M. Becker presented on
December 7, 2015.

APPROVED:

_____

Major Professor, representing Radiation Health Physics

_____

Head of the School of Nuclear Science and Engineering

_____

Dean of the Graduate School

I understand that my dissertation will become part of the permanent collection
of Oregon State University libraries. My signature below authorizes release of my
dissertation to any reader upon request.

_____

Eric M. Becker, Author

ACKNOWLEDGEMENTS

TABLE OF CONTENTS

LIST OF FIGURES

LIST OF FIGURES (Continued)

LIST OF FIGURES (Continued)

LIST OF TABLES

Chapter 1: Introduction

1.1 Motivation

There are many scenarios in which the need to search for a radiation source arises, such as emergency response after a natural or human-made disaster, or radiological threat interdiction at a port or in a city. In particular, the National Nuclear Security Administration under the US Department of Energy supports several emergency response teams, such as the Aerial Measuring System [1], the Radiological Assistance Program [2], and the Nuclear Emergency Support Team [3], tasked with search for radiological sources both before and after emergency events [4]. The US Department of Homeland Security Domestic Nuclear Detection Office also supports programs tasked with searching for radiological sources, particularly in urban envrionments [5]. In these scenarios, the location, isotopic compostition, and activity of a source or set of sources may be unknown. The radiation source may also be located in an area hazardous to human life, due to the radiation source itself or factors of the environment in which it is located. Because of these hazards, it is especially advantageous with regard to human risk mitigation and mission success to limit the proximity of human search teams to the search area. An ideal radiological search system would therefore be able to search an area remotely, as well as quickly and accurately.

1.2 Current Radiological Search Methods

Methods used to search for radiological sources can be broadly split into three categories. The first are methods that move a detector to the radiation source (Field Search). This type of search typically takes the form of a human search team member sweeping a simple radiation detector, such as a Geiger-Mueller counter, back and forth over the search area and noting where the count rate is highest. Other categories are those that move the suspected radiation source to the detector (Gate Search), and those that estimate the location of the source remotely (Remote Search). Across all of the above methods, either gamma rays or neutrons are the type of radiation detected since they have the greatest range in air.

Field search methods have a major advantage compared to gate and remote searches because the detector is moved closer to the source. This increases the radiation detection efficiency of the detector, which is inversely proportional to the distance squared, as well as more clearly establishes the location of the radiation source and its surroundings. However, current implementations of the field search method almost always take the form of a human operator who must carry a radiation detector to and around the area. This is non-ideal both because it relies on human intuition to find the source and because it increases the human-borne risk. The gate search methods rely less on human intuition, but much more on the source's movement since it muss pass near the stationary detectors in order to be found. Finally, remote search methods are capable of generating estimates of source locations from a safe operator distance, but require longer counting times

and do not take the user to the actual source site.

1.3 Unmanned Directional Radiological Search System

An ideal radiological search system, as previously described, should encompass three qualities. First, it should have high radiation detection efficiency. This is important in order to more quickly accumulate interaction events and thus record more information about a source in a given amount of time. Higher radiation detection efficiency can be achieved in a number of ways, such as by increasing the detector volume, density, and effective atomic number. However, one method for increasing the radiation efficiency of a detector that can be applied no matter the detector material or size is to decrease the distance between the detector and the radiation source. Since it may be difficult to predict whether a given radiation source will pass close to a stationary detector systiem, a mobile system is more advantageous.

Second, the ideal radiological search system should give some indication of the relative direction in which the radiation source is located. This ability improves the speed with which the source can be found. Without an indication of source direction, mapping methods must be employed, necessitating a sweep of the area with the detection system. While this may be useful for large-area contamination scenarios, it is inefficient when searching for concentrated, non-distributed radiation sources, such as nuclear reactor fuel rods and radiological weapons since it requires moving the detector over the entire search area. If the detector is able to

give an indication of the source direction, the source location can be determined more directly and in less time.

Finally, the ideal system should not require a human operator to remain nearby and thus be able to be remotely operated or autonomous. The search area may be hazardous for a number of different reasons, such as fire, unsafe structures, or even the dose due to the source itself. Being able to send an unmanned system into the hazardous area significantly reduces the risk to human health while still allowing the detector to move closer to the source and increase its radiation detection efficiency.

One technology that can be implemented in a radiation detection system to provide the three qualities listed above is the unmanned vehicle. Robots and other unmanned vehicles are being used more and more to perform dangerous tasks, removing the need to send humans into dangerous situations. They are also often able to perform their task more quickly than their human counterparts. Small, multi-rotor unmanned aerial vehicles (UAVs), often referred to as drones, in addition to rapidly gaining popularity, are an ideal platform for an unmanned radiological detection system. They are relatively inexpensive, agile, and low-flying, enabling them to be cost-effectively deployed, move and change direction quickly, and keep the detector close to the same altitude of the source, thus maximizing the radiation detection efficiency.

1.4   Research Goal and Objectives

The goal of this work is to demonstrate the proof of concept for a low-cost, lightweight, direction-sensitive radiation detector, called the Radiation Compass, that can be mounted on an unmanned multi-rotor UAV. The main objectives that will be completed to achieve this goal are:

1. to fabricate a Radiation Compass prototype,

2. to characterize the detector response to radiation sources in various positions,

3. to implement operating firmware and user interface, and

4. to implement and evaluate direction-estimation algorithms.

Chapter 2: Literature Review

2.1 Scintillator Radiation Detectors

Scintillator materials have been in use in radiation detectors since the 1930's [6], and have remained widely-used. A scintillation-based radiation detector requires two components: the scintillator material and a light-collection device.

2.1.1 Scintillator Detector Principles

Scintillation materials are used in radiation detectors for their ability to convert deposited radiation energy into measurable light. These materials generally fall into two categories: organic scintillators and inorganic scintillators, named for the types of elements of which they are composed. Both materials emit photons in response to stimulation by absorbed energy. However, while organic scintillators become excited at the molecular level, inorganic scintillator materials are excited at the level of electrons. Inorganic scintillators are typically chosen for applications involving the detection of gamma rays since they posses higher effective atomic numbers and higher densities than organic scintillators. They are also more useful for gamma spectroscopy since they generally release more photons per absorbed radiation energy [7].

In inorganic scintillators, there exist three energy bands defined by electron

energy states that arise due to the bonding structure of the constituent atoms for a given material. The valence band is the lowest of the three, and covers the energy range of chemically-bonded electrons. The band gap is above the valence band at an energy range where no quantum energy levels exist for the given material. Finally, the conduction band covers the highest energy range, and is where electrons with sufficient energy are able to freely pass through the crystal lattice. When a radiation interaction releases energy into the scintillator material, electrons in the valence band are excited and pass into the conduction band. These electrons will randomly de-excite back to the valence band with a characteristic half-life. When the electrons de-excite, they release their energy as photons [8].

The energy of the photons emitted is equal to that of the bandgap of the crystal material. However, most pure scintillator materials have bandgaps large enough that the de-excitation photons have wavelengths in the ultraviolet range of the electromagnetic spectrum [9]. In order to shift the wavelength of the photons into the more easily-measured visible range, impurities called "activators" are added to inorganic crystals. An activator introduces energy states in the band gap range that electrons can fall into, thereby emitting photons with less energy than the band gap, which results in photons in the visible range. This effect has the additional benefit of shifting the photons away from the wavelengths at which the scintillator naturally absorbs light most efficiently, allowing significantly more photons to escape the scintillator [8]. This process is illustrated in Figure 2.1. The process of electron excitation, immediate de-excitation, and photon emission is called flourescence and is the primary mode of light generation in inorganic scin-
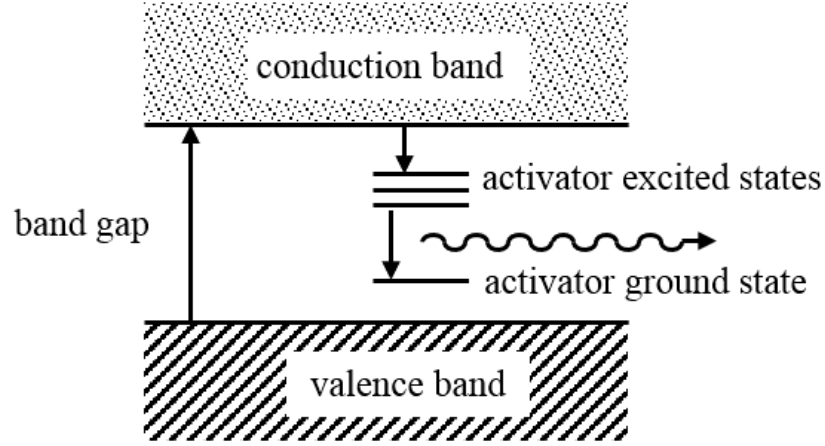
Figure 2.1: Illustration of energy levels in an activator-doped inorganic scintillator material. Reproduced from [8].

tillators. Delayed flourescence is also possible, and operates like fluorescence with the exception of a longer de-excitation half-life. Phosphorescence is another light emission process that electrons can undergo, where the electron reaches an activator site and falls into one of the activator energy-states, but does not possess energy sufficient to fall into the valence band [10]. The additional energy necessary for the electron to transition to the valence band typically comes from thermal energy and the electron will release photons as it does via fluorescence, but with a longer half-life. These light-emitting processes are illustrated in Figure 2.2. Still other processes exist that do not release any photons, such as quenching [8]. Because fluorescence is is the primary mechanism by which most inorganic scintillators emit light, a single time constant is often used to characterize the decay of their light emission after a radiation interaction event. This characteristic decay is described using Equation 2.1:
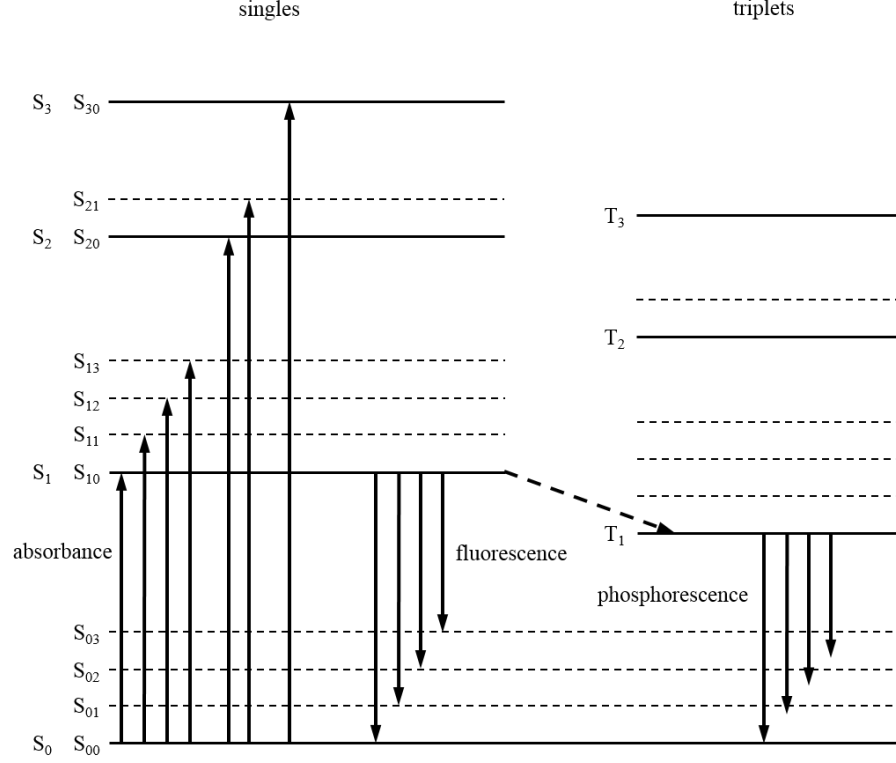
Figure 2.2: Illustration of energy levels in an activator-doped inorganic scintillator material. Reproduced from [8].

$$I = I_0 \cdot (e^{-t/\tau} - e^{-t/\tau_0}), \qquad (2.1)$$

where $I(t)$ is the light intensity at time t, I_0 is the original light intensity, and τ is the characteristic light decay time. This equation also includes the rise time term with a time constant τ_0 that is characteristic the time it takes for electrons to transition to the excited state [8]. These times are important when considering the design of the electronic readout system and the application of the detection system.

2.1.2 Solid-State Photomultipliers

Scintillators release a relatively low number of photons per quantum of energy absorbed, with the best inorganic scintillators releasing tens of thousands of photons per MeV of absorbed radiation energy [8]. Therefore, photodetectors able to detect single photons are required to accurately measure the number of photons emitted from a given scintillator. A comparatively recent type of device that has been developed for this purpose is the Geiger-avalanche photodiode array, more commonly called a solid-state photomultiplier (SSPM). The development of SSPMs started with the development of avalanche photodiodes in the early 1960s [11, 12]. Early versions were not able to distringuish single photons, but improved manufacturing processes and design have led to the current SSPMs, which are also commonly called silicon photomultipliers (SiPMs) since most designs use silicon as the semiconductor material [13, 14]. SSPMs are now considered to be an alternative to PMTs due to their ability to detect single photons, achieve gain comparable to PMTs, and even provide better energy resolution than PMTs due to their superior quantum efficiency [15, 16].

The structure of a SiPM is composed of small "microcells", each one a Geiger avalanche photodiode, all with a common cathode and anode. The basic SiPM structure is illustrated in Figure 2.3. The microcells are themselves composed of one metal contact, resistor, and semiconductor layer each [17]. The semiconductor is setup as a p-n junction, such that each microcell can be described as a diode and resistor in series, and the SiPM device as a collection of microcells in parallel,
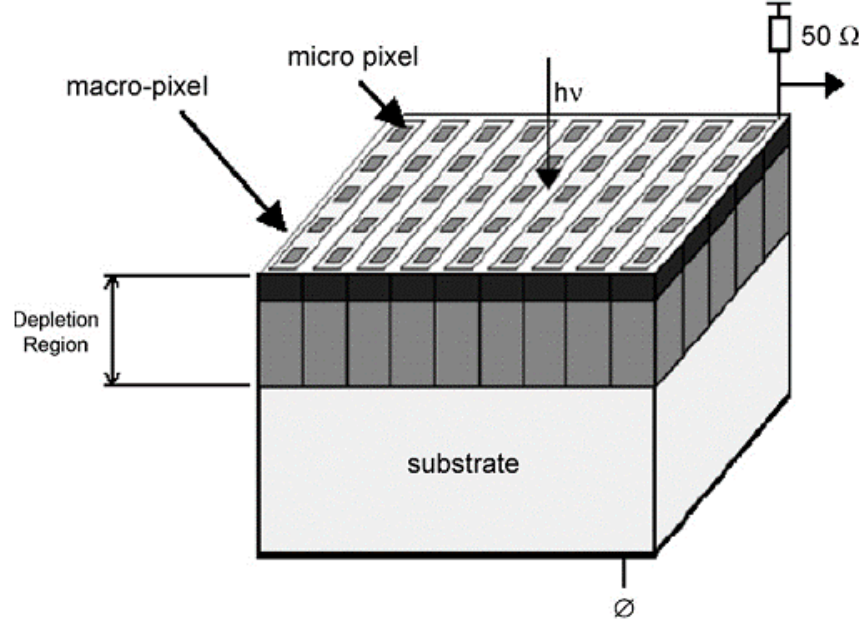
Figure 2.3: Illustration of SiPM microcell structure [13].

as illustrated in Figure 2.4. Photons are ideally absorbed in the semiconductor layer, with the absorbed energy of the photon generating an electron-hole pair. The excited electron and hole, known as charge carriers, begin to move due to the applied electric field. The voltage bias applied to the microcell array is greater than the breakdown voltage, which causes the charge carriers to ionize additional atoms as they move toward their respective electrodes. The multiplication of electron-hole pairs is called a Geiger avalanche, which significantly amplifies the amount of current generated by the absorption of a single photon. The amount of multiplication, or gain, is characteristic for a given voltage bias [13, 14].

The resistor layer is present in order to quench the Geiger avalanche. As the current through the microcell increases, the voltage across quenching resistor also
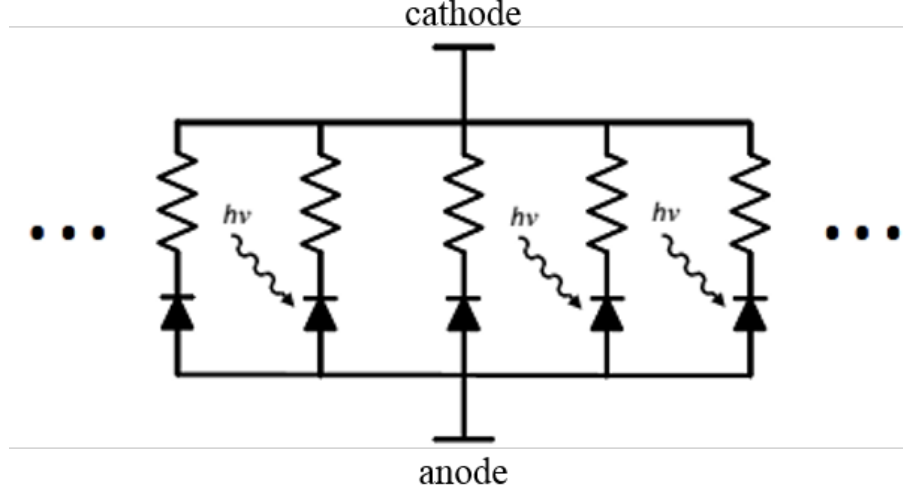
Figure 2.4: Illustration of SiPM electrical equivalent [18].

increases to the point where the voltage across the semiconductor layer drops below the breakdown voltage. Without sufficient voltage, the charge carriers no longer ionize additional atoms, and the Geiger avalanche ceases. Once the current has discharged, the voltages across the resistor and semiconductor layers return to their original states, able to sustain a Geiger avalanche again [13, 14].

Current SiPM technology allows tens of thousands of microcells to be fabricated in a few square millimeters. A larger number of microcells per unit area increases the likelihood that, when coupled to a scintillator, each scintillation photon will trigger a different microcell. This relationship can be described by Equation 2.2:

$$N_{fired} = M(1 - e^{-\frac{PDE \cdot N_{ph}}{M}}),\tag{2.2}$$

where N_{fired} is the number of microcells triggered, M is the total number of mi-

crocells, PDE is the photon detection efficiency of the SiPM, which encompasses the quantum efficiency and geometric efficiency, and N_{ph} is the total number of photons incident on the microcells. For a constant M, as N_{ph} becomes large the number of microcells triggered N_{fired} approaches an asymptote. The reason for this asymptotic behavior is that multiple photons absorbed in a single microcell within the time frame of the Geiger avalanche and quenching still produce only one avalanche [19].

2.2 Radiation Counting Statistics

The decay of radioactive nuclei is a random process, characterized by the given isotope's radioactive half-life. Thus, any measurement of radiation quanta is subject to inherent statistical fluctuation and must be analyzed using counting statistics.

Radioactive nuclei have a certain probability of decaying in a given amount of time. Radioactive decay is characterized by Equation 2.3:

$$\frac{dN}{dt} = -\lambda N, \tag{2.3}$$

where N is the number of radioactive nuclei of a particular isotope, t is the amount of time for which the radioactive nuclei are observed, and λ is the radioactive decay constant [20]. This equation describes the number of radioactive nuclei that decay, on average, in a given amount of time. When solved for N as a function of t, Equation 2.3 becomes Equation 2.4:

$$N(t) = N_0 e^{-\lambda t}, \tag{2.4}$$

where $N(t)$ is the number of radioactive nuclei at time t, and N_0 is the number of radioactive nuclei at time $t = 0$. The term $e^{-\lambda t}$ can also be described as the probability that a given radioactive nucleus will remain un-decayed after time interval t.

The measurement of radiation interactions in a radiation detector can be described as a number of trials equal to the number of radioactive nuclei under observation, where each trial is the observation of a single radioactive nucleus for time interval t. At the end of the time interval t, a given radioactive nucleus will either have decayed or not, resulting in a binary "success" or "failure" outcome of the trial. The trial is considered a "success" when the radioactive nucleus undergoes decay since radiation detectors cannot detect un-decayed nuclei. The probability of success is therefore $1 - e^{-\lambda t}$, and is constant for a given period of time, since λ is constant. The measurement of radiation interactions in a radiation detector can be described as a number of trials, where each trial is the observation of a radioactive nucleus for time interval t. The number of successful trials that will be observed cannot be predicted for certain given the random nature of radioactive decay, but will follow a certain distribution given the binary and constant-probability nature of each trial.

The most general distribution function that describes the probability of observing a given number of successes is the binomial distribution:

$$P(x) = \frac{n!}{(n-x)!x!} p^x (1-p)^{n-x}, \tag{2.5}$$

where $P(x)$ is the probability of observing x successes (decays), p is the probability of success in one trial $(1 - e^{-\lambda t})$, and n is the number of trials (N_0). The binomial distribution is normalized such that the sum of its probabilities is equal to 1, its mean is $\bar{x} = pn$, and its standard deviation is $\sigma = \sqrt{np(1-p)}$ [8].

The binomial distribution can be simplified to the Poisson distribution under the condition that the probability of success be small and constant [8]. If the time interval t in which the detector is measuring radiation interactions is small compared to the half-life of the particular isotope being measured, then the probability of observing a given nucleus decay is very small. In addition, the probability of success of each trial remains constant since the half-life of a given radionuclide is constant. Thus, when radiation counting conditions fulfill these requirements, the distribution of observed successes for repeated measurements can be reduced to the Poisson distribution:

$$P(x) = \frac{(pn)^x e^{-pn}}{x!}. \tag{2.6}$$

The binomial and Poisson distribution share some of the same properties, such as their mean $\bar{x} = pn$, and the fact that they are normalized. However, the Poisson distribution requires that only the mean $\bar{x} = pn$ be known in order to calculate the values of the distribution, and not the probability p of each trial and the number of trials n. The standard deviation of the Poisson distribution is also much simpler

than that of the binomial distribution, and can be shown to be $\sigma = \sqrt{\bar{x}}$.

The Poisson distribution can be further simplified if the mean of the actual distribution is large, 20 being the commonly-accepted threshold [8]. Though not true of all radiation counting experiments, most do detect more than 20 events. The simplification of the Poisson distribution leads to the form of the Gaussian distribution:

$$P(x) = \frac{1}{\sqrt{2\pi\bar{x}}} e^{-\frac{(x-\bar{x})^2}{2\bar{x}}}. \tag{2.7}$$

The Gaussian distribution, like the Poisson distribution it was derived from, has mean $\bar{x} = pn$, has standard deviation $\sigma = \sqrt{\bar{x}}$, and thus also only requires that the mean be known to be able to calculate the values of the distribution. The Gaussian distribution has several other important properties, such as its symmetry around the mean $\bar{x}$.

2.3 Radiological Search Methods

There are many methods, techniques, and detector systems that can be used to search for radiological sources.

2.3.1 Traditional Methods and Devices

The simplest method for locating a source of radiation is to transport a radiation detector back and forth over an area, observing where the count rate is highest.

The radiation detector used for this purpose can range from those that provide the user with only a count rate, such as the Geiger-Mueller counter, to those that can generate an energy histogram and perform isotope identification. While using a simple counting detector might make this method low-cost, this method requires that a human operator enter a potentially hazardous area, especially in the case of an emergency or on the battlefield. These detectors also have no directional indicator, so the search is guided by human intuition and interpretation of the count rate. Thus, the simple search method is time consuming, especially when a large area must be searched.

Another method for locating radionuclides is to place large stationary detectors immediately adjacent to high-traffic areas. The most common embodiment of this method is the radiation portal monitor now used at major sea- and airports, an example of which is shown in Figure 2.5. Other versions include city-wide detector networks and remote, road-side monitors. This method employs large-volume detectors, or multiple smaller detectors to achieve a larger detection volume. Some portal monitors even possess HPGe detectors for high-accuracy radioisotope identification. The main drawback to this method is that sources must pass near the detectors location at a relatively low speed to be detected [21]. In the case of portal monitors, this means that vehicles must pass between the two pillars, which limits the monitors' search capability and slows traffic that must be searched. An actor with malicious intent might even be able to circumvent the detectors altogether by passing behind them or via a route not near enough to the detector for detection. Because these systems usually employ multiple detectors, they are also

Figure 2.5: Photo of a radiation portal monitor [21].

very expensive, with portal monitors costing upwards of USD $1M. Finally, these detectors do not give an indication of the source position inside a vehicle or cargo that has been searched, necessitating an additional search by human personnel, potentialy putting human life at risk.

2.3.2 Advanced Methods and Devices

Many advanced methods for radiation detection have been developed in recent years, mostly for the purpose of locating nuclear detonation or radiological dispersion devices for national security applications.

One method used to search for radionuclides, which has been used for years

but recently increased in popularity, is Compton imaging. This method uses the properties of gamma- and x-ray interaction with matter to generate overlapping cones of probability projected onto a virtual sphere. The locations where many projected cones interact is the most likely direction of the gamma- and x- rays. This method generates an accurate 2D image of the source than can greatly aid the user when overlaid onto an image of the detector's surroundings, shown in Figure 2.6. Indeed, a current, commercially available system is able to localize
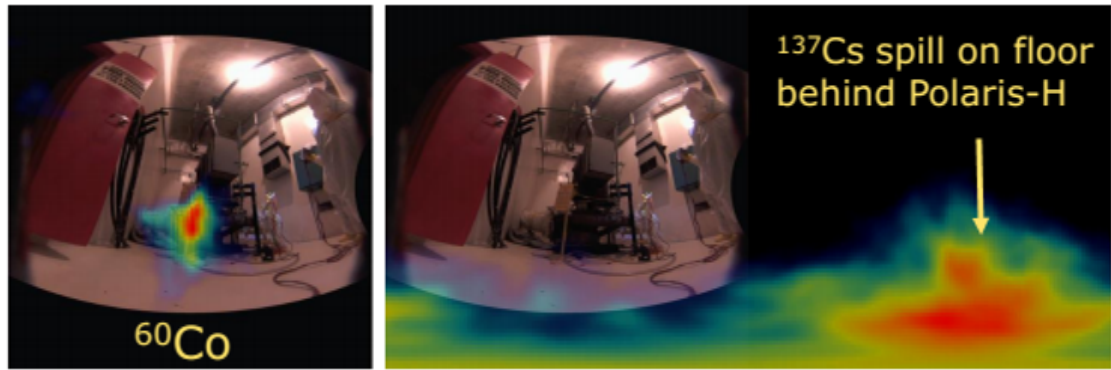
Figure 2.6: Photo of a room at a nuclear power facility with the Compton-generated source images superimposed [22].

a radiological source within 1° with a 4π field of view in under 5 minutes. The device, the "Polaris-H" is shown in Figure 2.7. Compton imaging systems can also measure the energy of the interactions, and thus identify the isotopes present in each source imaged [22]. However, the accuracy of this method comes at the price of time needed to build a source image because recording Compton scatter events is inefficient even for materials with a high atomic number (high-Z), such as CZT, which has an intrinsic Compton interaction efficiency of just 2% for a 20
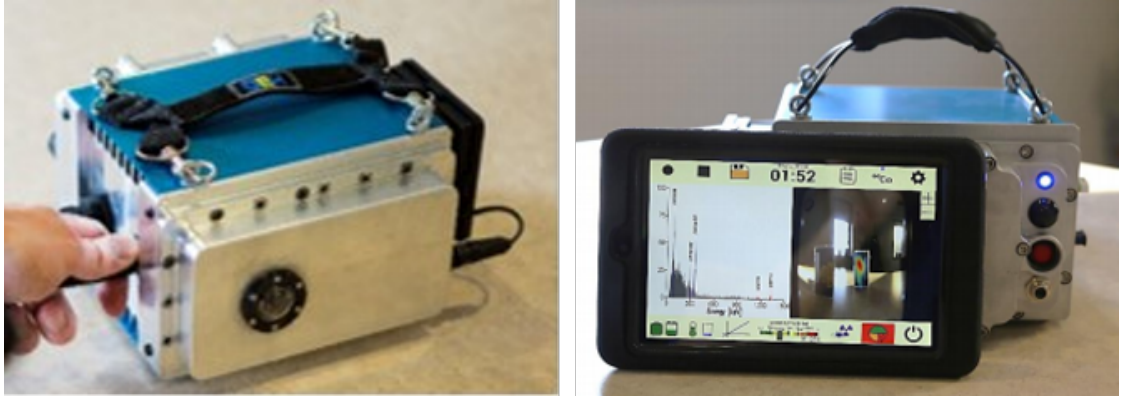
Figure 2.7: Photo of the Polaris-H Compton imaging system [22].

x 20 x 15 mm^3 crystal [23]. Though recent improvements to the efficiency of this method have been demonstrated [24], the reported 45% increase still only affords the method a Compton interaction efficiency of approximately 3%. In addition, the Compton imaging device must remain stationary while the Compton events are being measured and recorded, adding to the time needed to locate a source. Finally devices that employ Compton imaging are expensive, either because they use multiple detectors or because of the cost of materials like CZT.

Another detection system consists of one or more directional detector arrays [25], shown in Figure 2.8. Each of the arrays is composed of a cluster of closely-packed radiation detectors arranged in a regular pattern. By observing the count rates among each of the detectors in the directional array, a probability distribution for the direction of the source can be generated using the Maximum Likelihood estimator [26, 27]. By using more directional detector arrays, the most probable location of the source can be determined with increasing accuracy. However, the description of this system indicates that these detector arrays are meant to be
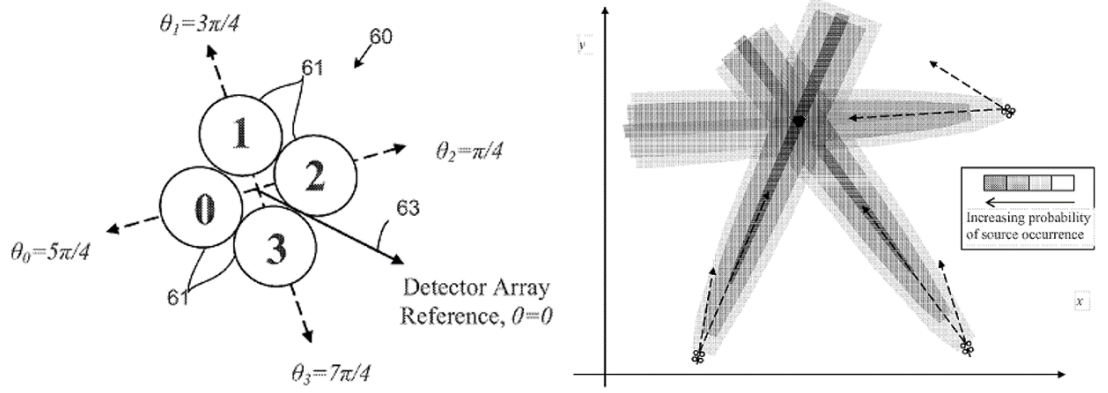
Figure 2.8: Illustrations of the tight-packed radiation detector array [25].

set up in stationary positions around an area since the intended detector size is large. However, using stationary detectors, even direction-sensitive ones, has several significant disadvantages. The first is positioning the detectors close to the source: they can either be positioned at a location near where the source is expected to be, or move to near the source location after the source has moved to the area. If they are set up beforehand, the detectors may become damaged by hazardous events that take place in the area, be sabotaged by malicious forces, or the source may not moved to the predicted area. If an attempt is made to set up the detectors after the source reaches a location, conditions may be too hazardous to set up the detector or environmental factors may prevent the detectors from being set up close enough.

One example of a large-scale mobile detection platform is the RadMAP truck-based system. RadMAP an array of 24 HPGe detectors, an array of 100 NaI(Tl) detectors set up behind a coded-aperture mask, and 16 EJ-309 liquid scintillation counters for neutron detection as shown in Figure 2.9. These detectors,
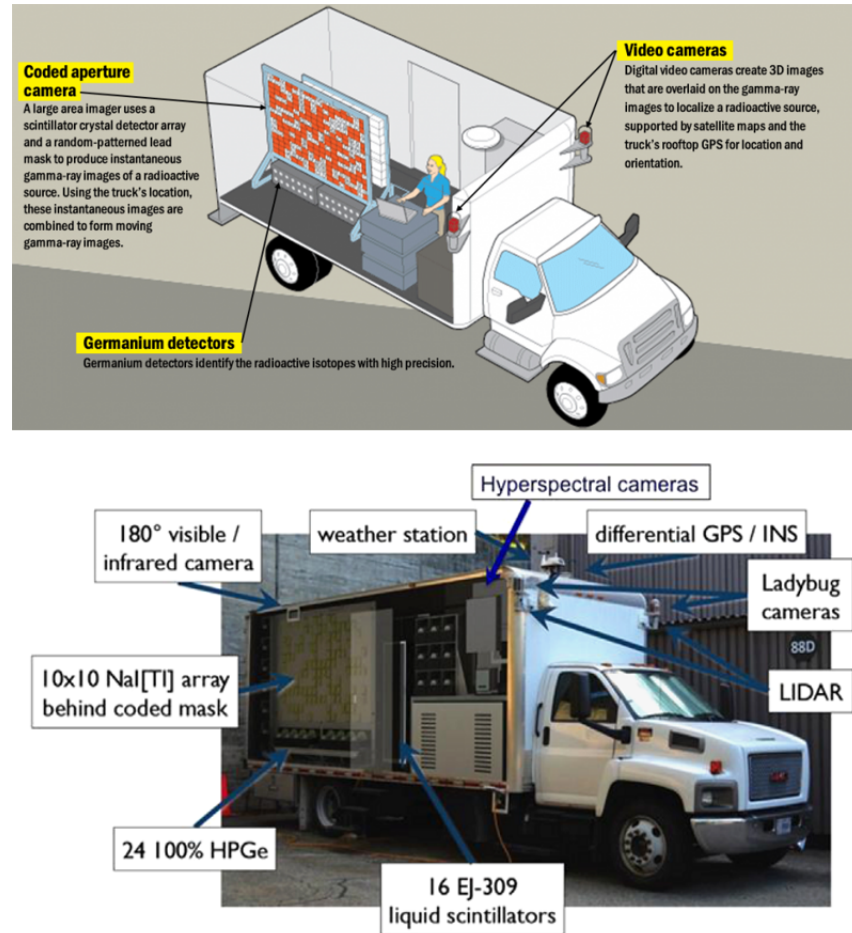
Figure 2.9: Illustration and photo of the RadMAP system mounted in the cargo truck transport [28, 29].

along with visual and hyperspectral (400-1700 nm) cameras, GPS, LIDAR, and a weather station are mounted in a large cargo truck [29]. The truck has been used to transport the system around Alameda and Oakland, CA, and the surrounding areas to cataloge the background radiation signatures observed in these areas [30]. The information gained from all sensors during these surveys is then correlated, giving estimates of the amount and energy of the normal background

radiation generated by certain material and building types [31]. In a radiological search scenario, this information would be used to assist searchers in identifying and locating sources of radiation as the truck is driven through these areas. The prior knowledge of background radiation would allow searchers to dismiss these sources and is important, especially in an urban environment, since the amount of background radiation can change significantly from location to location. Though the system does have a large detection volume, affording it a high detection efficiency, the gamma detectors used do not have particularly high density or atomic number and were instead chosen for their spectroscopic properties. The RadMAP system also represents a significant investment given the large number of detectors and other systems mounted on the truck. The truck is also limited in its search capability since it must drive on streets, which may be too narrow or simply not exist on routes in proximity to a theoretical radiological source. In addition, it has no ability to change its height or the angle of the detectors to better measure sources of radiation that may not be present on the first two to three stories of an urban area.

Another example of radiation search technology are detectors developed for aerial search from helicopter platforms. Some systems are based on a simple bulk detector arrangements and the count rate mapped over the search area [32, 33]. One example of a more sophisticated system is the Aerial Radiation Measurement System (AMS), for which different detectors have been developed. The Airborne Radiological Enhnaced-sensor System (ARES) is a set of four arrays of 26 CsI(Na) detectors each [34]. Each of the arrays is arranged in a staggered pattern shown in

Figure 2.10, with two arrays located in each pod on the helicopter. The detectors
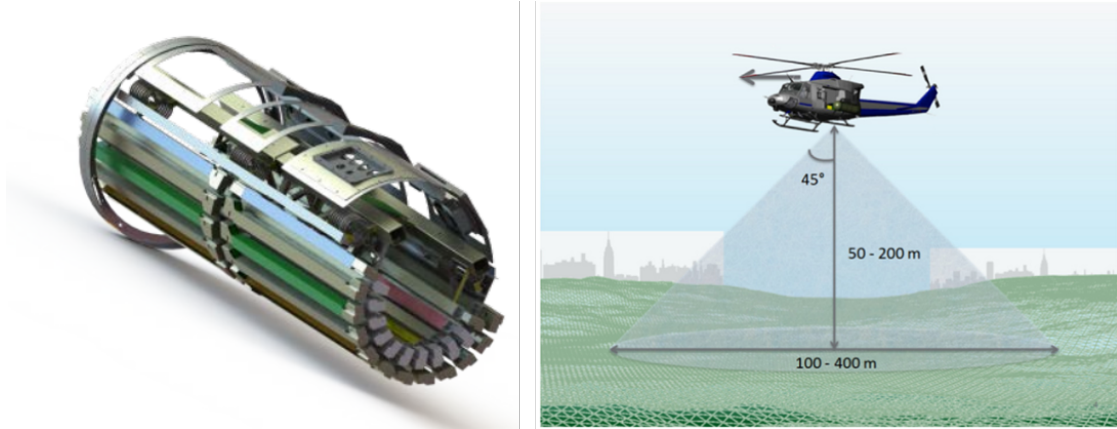
Figure 2.10: Illustrations of the Airborne Radiological Enhanced-sensor System (ARES) and the Aerial Measurement System (AMS) [34].

in the ARES can be counted in three different patterns: individually, sets of four, and all detectors together. Each pattern affords the system a different level of directional sensitivity, with analysis of individual detectors having the highest directional sensitivity, all panels summed the lowest, and groups of four in symmetric positions a compromise between directional sensitivity and computational speed. The directionality is achieved by characterizing the detector response to sources at different distances and angles compared to the detector arrays and then comparing those measurements against measurements taken in the field using Maximum Likelihood estimation. A Bayesian algorithm is then used to compare estimates generated by the detector measurements iteratively, building up the likelihood that a source is located at a given position as the detector system is flown over an area. Since the system is mounted on a helicopter, passes are made at altitudes of 50 - 200 m and generally at relatively high speed (about 36 m/s in [34]). While the

AMS/ARES system can detect and localize sources on the order of millicuries to the order of tens of meters after only a few passes, some radiological search scenarios will involve sources that are on the order of microcuries, such as a shielded nuclear detonation device. In these cases, the search system may need to hover over an area for a longer period of time, exposing the human pilot and any passengers to greater risk. In addition, such a detector system represents a significant investment given the number of detector elements used in each array. Finally, due to its size, this system would only be able to be used outdoors.

One final example of a directional detector search technology is the Octagonal Directional Detector (ODD), an illustration for which is shown in Figure 2.11 [35]. The ODD consists of eight 10 x 20 x 1 cm^3 CsI(Tl) plates arranged in a circular pattern, similar to the detector developed for this work. The ODD was developed to assist in making initial directional measurements for a Compton imaging device in order to be able to obtain a better image faster. The ODD is able to estimate the direction of a source of radiation through a combination of the shape of the scintillator plates and the attenuation of plates on opposite sides of the detector, which produces a detector response pattern for individual plates shown in Figure 2.11. Chi-squared minimization is used as the angle estimation method. While similar in design to the Radiation Compass presented in this work, the ODD has some disadvantages when considered for the same role. First, it is larger, with an estimated diameter of approximately 24 cm, based on the scintillator plate size and arrangement, and would therefore need to be mounted on a larger UAV, possibly limiting it to outdoor use. Second, it uses CsI(Tl) crystal which are not as efficient
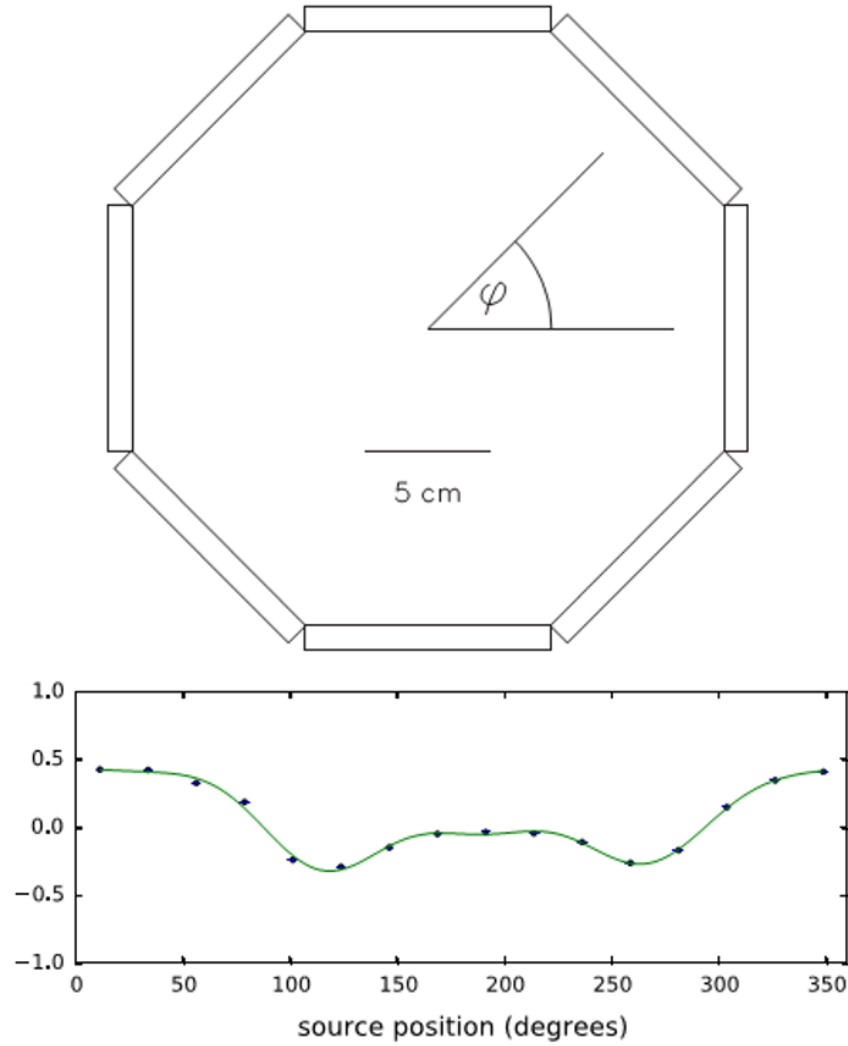
Figure 2.11: Illustration of the Octagonal Directional Detector and the response of one of the CsI(Tl) plates for different source angles around the device [35].

for gamma-ray detection compared to other scintillation materials such as BGO. The ODD also uses PMTs, which are bulky, heavy, and expensive. Finally, the indended use for the ODD is to optimize the initial angle of a Compton imager

that will perform the main source location estimation, and thus uses two separate detectors instead of just one.

2.3.2.1   UAV Specific Devices

The concept of using a UAV with a radiation detector to search for radiation sources is not a new idea, nor is using a detector with directional capability. Several systems that have been already been conceived for the purpose of finding radiation source remotely are outlined here, and their merits and demerits discussed.

One technology that could be used to detect radiation from a UAV is a type of paint that changes properties when subjected to a dose of radiation [36]. Such a paint could easily be applied to the outside of a vehicle, as shown in Figure 2.12. The property of the paint that changes with exposure to radiation could
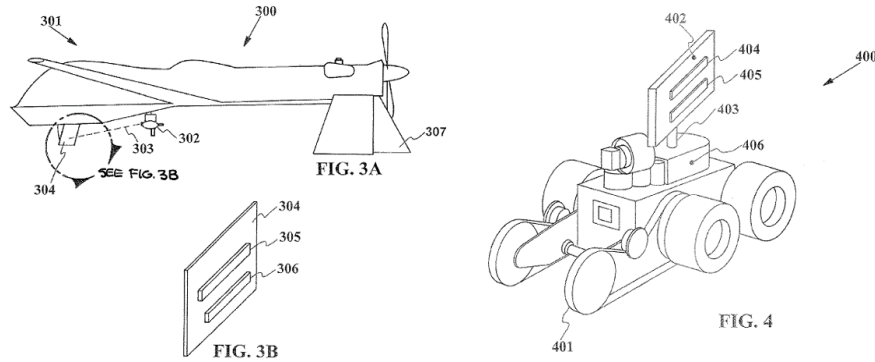
Figure 2.12: Illustration of the application of the radiosensitive paint to different unmanned vehicles [36].

then be measured and relayed to human monitors. For example, the paint might be made to change color when exposed to radiation, and then be recorded by an

on-board camera. This solution is low-weight and would likely be low-cost, as well. However, it has several major shortcomings. First and most importantly, the paint would only be able to give a general direction at best, corresponding to the side of the vehicle on which a change was observed. The paint would act like a simple detector, capable only of detecting the presence of radiation and not the direction in which it originated nor the radionuclides it is composed of, thus failing two of the most important requirements of the detector. In addition, being a paint or coating, it would be very thin, and thus inefficient for radiation detection. Since the paint relies on a non-reversible change in material property to detect radiation, it would only be able to be used once. Overall, this solution is better suited to the simple detection of radiation, and not any accurate measure of the direction or amount.

Another type of detection system that could be used is a structurally-integrated detector, two examples of which are shown in Figure 2.13 [37, 38]. Such a system would have the radiation-sensitive material volume integrated into the structure of the vehicle, presumably as a part of the general load-bearing structure. This way, the detector is not actually a payload, but part of the empty-weight of the vehicle, making it lighter and in the case of an aircraft, capable of longer flight times. This can also afford the detector a large volume, making it more efficient for detecting radiation, and ultimately yielding a faster search time. As mentioned in the source documents, the best choice of detection material for this system would be one or more scintillation materials since they can be manufactured to have large sizes. However, this approach has several major disadvantages. Firstly, this size
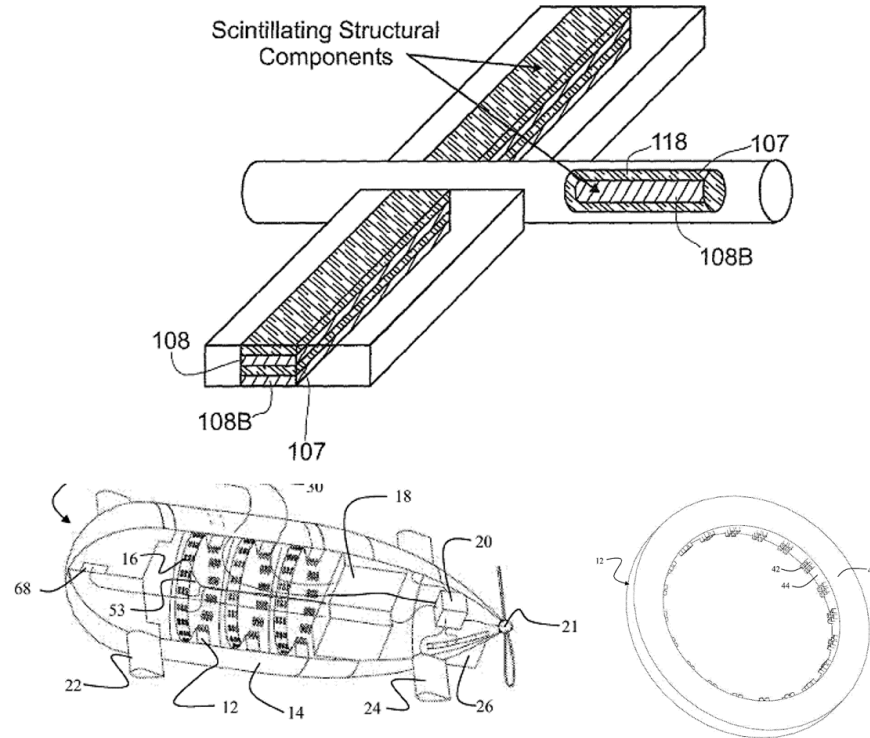
Figure 2.13: Illustrations of detector materials integrated into the structural components of unmanned vehicles [37, 38].

of the detector suggested by the figures included in the source documents means that the scintillation material would need to be an organic, which typically take the form of plastics or polymers. Though these materials are lightweight, they are not rugged or particularly strong in terms of tensile or compressive strength. Rough weather or even high-acceleration aerial maneuvers could overly stress these components, causing them to break or malfunction. For example, turbulence could cause the scintillator to become misaligned with its light readout device, causing the system to severely underestimate the number of valid radiation interactions.

In addition, the detector volume would only truly be large enough to outperform other approaches when integrated into an airframe of a large aircraft. Smaller aircraft, such as the popular quadrotor, a four-propeller rotor-bladed UAV, do not require such large airframes. This drastically reduces the detector volume, and negates the advantage of using scintillation material as part of the vehicle. Conversely, if a larger aircraft is used, the advantage of a larger detection volume will be counteracted by the need of the UAV to fly at higher altitudes. In addition, plastic scintillators have low efficiency for gamma rays, and typically have poor energy resolution. Finally, this type of system provides weak directionality at best and is more suited to radiation mapping.

The High-Efficiency Multimode Imager (HEMI) is a CZT-based radiation detector system designed to assist in locating radiological sources [29]. Shown in Figure 2.14, the HEMI system is designed with two planes of coplanar 1 cm^3 CZT detectors. In the front plane, 32 CZT elements are arranged in a coded aperture mask with 8 x 8 positions and 64 CZT elements are arranged in an 8 x 8 grid. As its title suggests, the HEMI is capable of both Compton and coded-aperture imaging techniques in real time, as well as isotope identification. While Compton imaging is effective at higher energies, at lower energies coded aperture imaging becomes more effective. A 24-detector implementation was found to have 11° FWHM angular resolution for ^{137}Cs with the planes separated by 7.5 cm, though the separation between the planes is adjustable to optimize the efficiency and accuracy of the imager [39]. The full 96-element imager was mounted on a RMAX remotely-controlled helicopter and used to scan contaminated areas in Fukushima. It was
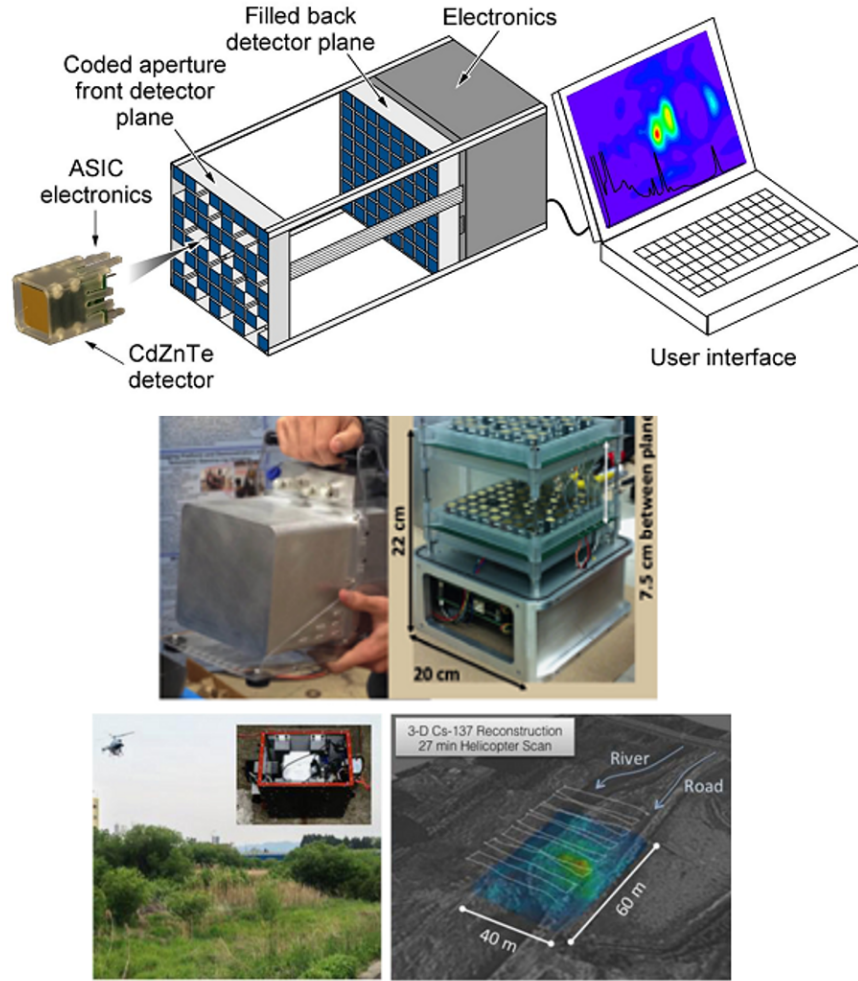
Figure 2.14: Illustrations of the HEMI device, along with photos of the complete device and aerial search photo and source map [29, 39].

able to achieve 10° FWHM angular resolution at 662 keV, and used Simultaneous Location and Mapping (SLAM) to correlate the radiation measurements to the terrain the helicopter flew over [29]. Despite these advantages, the HEMI system employed on the helicopter was 8 lbs (approximately 3.6 kg), which is heavy for

an airborne vehicle, hence the fairly large unmanned helicopter. Though such an unmanned helicopter is capable of carrying the detector, a lighter detector would still be preferrable since the helicopter would then be able to remain airborne for a longer period of time. The large helicopter and the CZT material, like the Polaris and ARES instruments, represent significant investments and must therefore be deployed with care, which may not be possible in a given scenario.

A final, and recent, example of existing radiological source localization is the Advanced Airborne Radiation Monitoring (AARM) system [40]. The system encompasses a solid-state radiation detector mounted on the underside of a rotor-blade UAV that can autonomously perform radiation mapping and identification tasks [41, 42], as shown in Figure 2.15. This system fulfills many of the parameters of an ideal radiological search system: it removes the need for human operators on-site, can identify radionuclides, and can be maneuvered close to the source. However, there are some key aspects of the ideal system that the AARM still lacks. The first is a directional indicator. The radiation detector does not possess a means to detect where the radiation source might be, and must instead travel back and forth over an area to map it out first, and then determine the source location based on this map. As previously mentioned, this method can be time-consuming. In addition, large-volume semiconductor detectors are difficult to manufacture. The largest semiconductor volumes currently available are made from silicon and germanium, which are low-atomic-number elements, and therefore inefficient for gamma-ray detection.
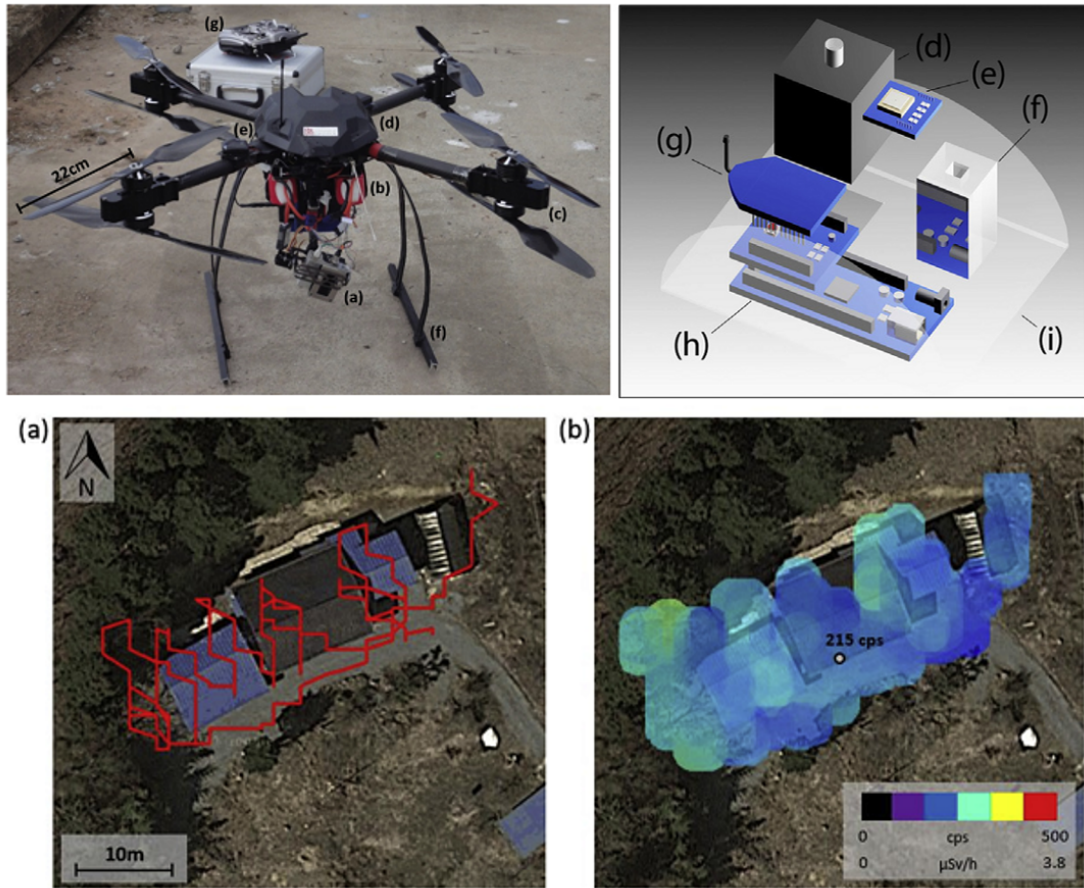
Figure 2.15: Illustrations and photos of the AARM system, as well as screen captures of its mapping software output [41, 42].

Chapter 3: Materials and Methods

3.1   The Radiation Compass

3.1.1   Detector Design

The Radiation Compass is a radiation detector designed to provide an estimate of the radiation source direction relative to the location of the detector from an aerial drone platform. The Radiation Compass was thus designed around a set of detector qualities that fulfill a set of system qualities.

3.1.1.1   System and Detector Qualities

First, the detector was designed to be efficient for detecting gamma radiation. When measuring any characteristic of a radiological source, be it energy, activity, decay time, direction relative to the detector, or other, observing a larger number of measured radiation quanta is always preferred because of the random nature of radioactive decay and its statistical properties as described in Chapter 2. Thus, using a detector with a higher chance of radiation interaction will yield better statistical results in a given amount of counting time. Of the four radiation types of interest when searching for radiological sources, alpha particles, beta particles, gamma rays, and neutrons, gamma rays and neutrons travel the farthest in air.

Since gamma rays are easier to detect than are neutrons, the Radiation Compass is designed to be efficient for detecting gamma rays in order to be able to accumulate counts more quickly, and thus find the radiological source more quickly. The system could, however, be converted to a neturon detector by simply replacing the scintillation material. Stilbene [8] is a popular scintillation material for the detection of fast neutrons, and materials like Cs_2YLiCl_6:Ce or boron- or lithium-doped plastics can be used to gain sensitivity to thermal neutrons.

Second, the detector was designed to be direction-sensitive. The advantage of this feature when searching for a radiological source is significant compared to a simple detector. To search using a simple detector, one must transport the detector across the search area, recording the count rate at each specific location, and then interpreting the count rate map to determine where the count rates are highest. Using this method, a large swathe of the search area must be covered and the count rate accumulated for a some amount of time at each position. A direction-sensitive detector would be able to guide the search to the location of the radiological source more quickly, covering a distance closer to the minimum of that between the search starting point and the radiological source location. The advantage of using a direction-sensitive detector is illustrated in Figure 3.1, where the simple detector must comb the area, and even measure past the actual location of the source in order to verify the position does in fact possess the highest count rate. The direction-sensitive detector, though initially incorrect in its directional estimate, still finds the source while covering less distance compared to the simple detector.
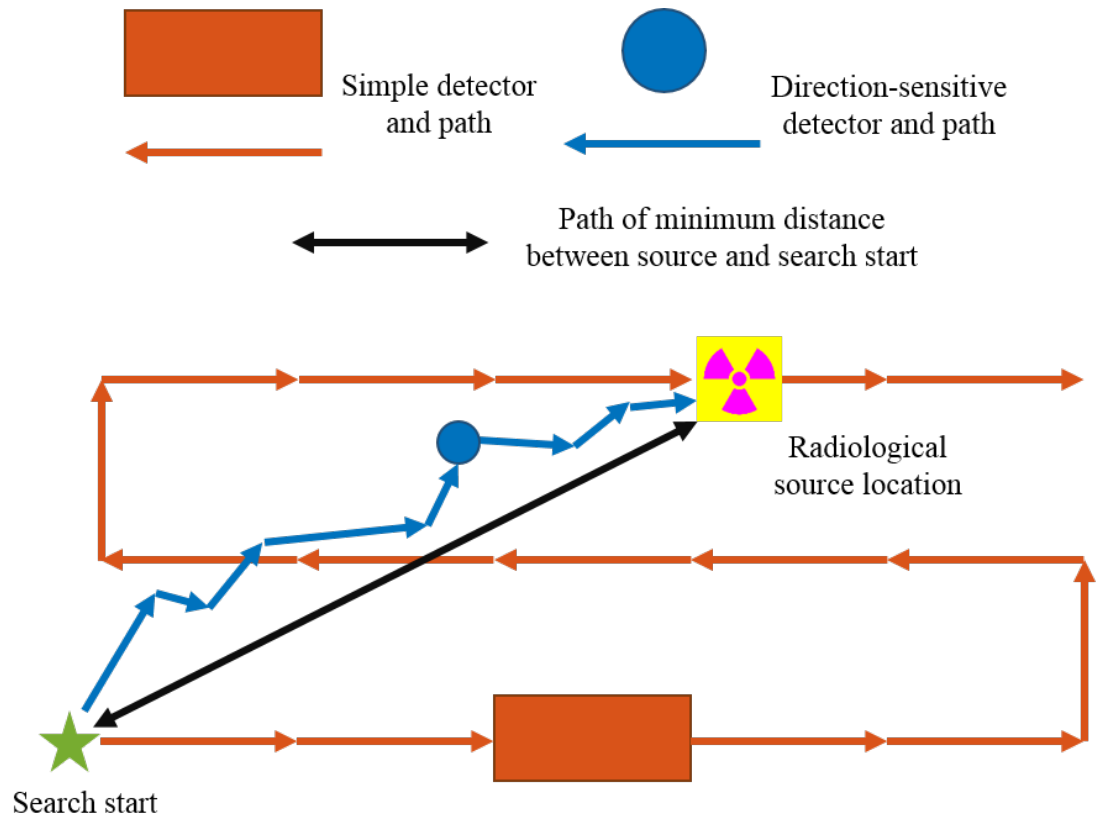
Figure 3.1: Illustration of the search path of a simple, non-directional detector versus a direction-sensitive detector in relation to the minimum distance between the search starting location and the location of the radiological source.

Third, the detector was designed to be low-cost. As mentioned previously, the system is intended to be deployed into situations which may be hazardous to human search teams. However, the situation or environment may also be hazardous to the drone and its radiation detector payload. The system may be damaged and even lost in the search area due to adverse weather conditions, for example. The organization conducting the radiological search might be reluctant to send a high-cost system into the search area since it would represent a significant invest-

ment, forcing decision-makers to choose to either wait until conditions improve, delaying the search, or risk possibly their only unmanned search capability, which, if damaged or disabled, would then necessitate deploying human search teams. By making the detector, and system as a whole, low-cost, decision-makers are more likely to subject the system to situations in which it can be damaged or disabled because they are able to replace the system or even have a spare system as a backup. This concept is illustrated in Figure 3.2 as a decision tree. Being able to afford more than one unmanned search system also gives the organization conducting the search the option of deploying more than one system at a time and coordinating their searches to decrease the amount of time needed to find the radiological source.

Fourth and finally, the detector was designed to be lightweight. The Radiation Compass is intended for use on a commercial or hobbyist UAV, or drone. Drones have limited flight times, with a typical current value being approximately twenty minutes with a 500 g payload. Since the flight time decreases as the drone's payload increases, the detector payload should be kept as light as practical in order to ensure that the source can be found within the flight time-frame.

3.1.1.2   Unmanned Vehicles

The three parameters of an ideal system for radiological search system can all be fulfilled with the implementation of one key technology: unmanned vehicles. Robots and remotely-controlled vehicles have been slowly but surely removing the

```
Use single, high-cost                                    Use multiple, low-cost
radiological search system                               radiological search systems

        │                                                        │
        ▼                                                        ▼
┌─────────────────┐                                    ┌─────────────────┐
│ High risk of damage │                                │ High risk of damage │
└─────────────────┘                                    └─────────────────┘
        │                                                        │
        ▼                                                        ▼
       Wait                                            ┌─────────────────┐
 Wait  ◇ until conditions ◇  Risk damage               │ Deploy one search │
       ◇ improve, or risk ◇                            │  system anyway   │
       ◇    damage?      ◇           Risk damage       └─────────────────┘
        │              │                                        │
        ▼              ▼                                        ▼
┌──────────────┐  ┌──────────────┐                    ┌─────────────────┐
│ Search is delayed │ │ System is damaged │            │ System is damaged │
└──────────────┘  └──────────────┘                    └─────────────────┘
Source may move        No unmanned       More unmanned         │
outside search area    systems left      systems available     ▼
        │              │                               ┌─────────────────┐
        ▼              ▼                               │  Deploy backup   │
┌──────────────┐  ┌──────────────┐                    │     system      │
│ Source not    │  │ Deploy human  │                    └─────────────────┘
│ found, wider  │  │ search team   │
│ search begins │  └──────────────┘
└──────────────┘
```

Figure 3.2: Illustration of a comparison between decision trees relating to a high-cost detection system and a low-cost detection system.

need to send humans into dangerous areas and situations. The remotely-controlled submersible Argo and the attached submersible robot Jason were used to first find the wreck of the Titanic in 1985. They also enabled the search to be conducted much more quickly, since the method used to find the wreck was to perform a visual search for debris on the ocean floor [43]. Some of the earliest unmanned vehicles were the satellites put into earth's orbit and beyond. The Mars Exploration Rovers A and B, named Spirit and Opportunity, explored the surface of Mars as directed by human operators at NASA [44]. Various other types of unmanned vehicles exist, from multi-pedal vehicles meant to carry heavy loads over uneven terrain [45] to airborne vehicles used for covert aerial surveillance [46] .

The type of unmanned vehicle most well suited to the task of locating a source of radiation is dependent upon where the search will take place, and what environmental conditions are present on-site. The situations considered in this work will be limited to surface operations. Given this constraint, the optimal vehicle for the vast majority of cases will be an unmanned aerial vehicle, or UAV. UAVs are faster and more agile than ground-based vehicles, and can simply fly above the majority of obstacles.

UAVs typically have either a fixed-wing or rotor-blade configuration. While fixed-wing UAVs typically have greater top speeds and longer flight times than rotor-bladed UAVs, they also possess several key disadvantages compared to rotor-bladed craft when searching for radionuclides. First, rotor-bladed UAVs are more agile, meaning they can more quickly change their heading, and thus more quickly make position adjustments during a search that ultimately results in a shorter search time. It also means that rotor-bladed UAVs can hover over an area in order to accumulate more counts in the detector, affording it a more accurate measure of the source direction. Second, while fixed-wing UAVs have a higher thrust-to-weight ratio and can thus carry heavier payloads, their payloads must must maintain the streamlined shape of the aircraft. Rotor-bladed UAVs, however, can mount a payload of nearly any shape as long as it can be mounted to the bottom of the UAV, and can keep it in a stable position with the use of a gimbal. Finally, the rotor-bladed UAV's ability to hover means it can fly very close to the ground, meaning it can position the attached detector closer to the source than a fixed-wing craft [47]. As stated previously, positioning the detector close to the source

is a key parameter for the ideal system. Cameras can also be fitted to the UAV to provide a visual confirmation that the source has been found, as well as give a visual map to the source's location.

More detailed specifications for the UAV include considerations of size and cost. The UAV should be small enough to fly through spaces that humans cannot, such as a partially-collapsed building for example. Also, the UAV may be sent into areas with hazardous conditions that may damage the system. For this reason, the UAV should be low-cost so that the risk of damage or loss of the system is not cost-prohibitive.

One key aspect of the DSRD is the ability to guide a UAV through a radiation field autonomously. While human operators could be used to guide the aircraft remotely based on the DSRD's measurements, a search algorithm that uses data from DSRD to autonomously locate a source could locate a source more quickly and precisely, and allow human observers to be located further from a potentially hazardous area of operation (AO) since only data signals, and not control signals, would need to be transmitted.

To be able to operate with autonomy, the UAV would not only need a method for navigating a radiation field, but be able to navigate terrain and physical obstacles, as well. There are several methods for achieving autonomous low-altitude UAV flight. One is to use the Global Positioning System, GPS. This system uses a network of satellites to triangulate the position of a receiving unit on the UAV to communicate its position on the Earth [48]. Another method is to use highly-reflective spheres attached to the UAV. Motion capture cameras are then set up

around the AO that track the sphere. The camera system then communicates the UAV's relative position. This can be used to perform complicated flight trajectories by telling the UAV not only its position, but the position of certain obstacles [49].

However, both of these systems have major flaws when it comes to hazardous environment applications. To use GPS effectively, the GPS receiver must communicate with four satellites, which requires line-of-sight to those satellites. If the UAV is required to enter a building or underground area, the GPS signal may be lost leaving the UAV unable to navigate. In a hazardous situation, GPS could prove unreliable and would make the system ineffective. Similarly, if using the motion-capture technique, the UAV must stay in line of sight of the cameras. If the view is obstructed, the system is not able to observe or communicate the UAVs position to it, and would therefore be ineffective. Setting up such cameras at the site of the radiation source search would be impractical, both before and after an emergency event. True autonomy requires that all the sensors needed for navigation be mounted on the UAV itself so that no outside signals are necessary.

Fortunately, this is an active and growing area of research for unmanned vehicles, and is currently referred to as Simultaneous Location and Mapping (SLAM) [50]. This technique can use any number of a variety of sensors, such as ultrasound, infrared, laser, optical, gyroscopic, accelerometer, radar, and lidar to name a few. These sensors communicate the distance from the UAV to surrounding obstacles, such as walls, furniture, trees, and the ground, for example. The UAV can then maneuver around these obstacles without the use of GPS or motion-tracking cameras by generating a navigational image of its immediate surroundings, and

storing and concatenating these images in a continuous fashion as it moves about to generate a map of the areas it has travelled through. While this can be used for exploration purposes, in the case of a radiological search, a SLAM navigation system would be used primarily for obstacle avoidance while the DSRD would provide the direction for the UAV to travel.

3.1.1.3 Operational Principle

The Radiation Compass prototype is shown in Figure 3.3, and a diagram of the design shown in Figure 3.4 from the top.   It essentially consists of a set of sixteen
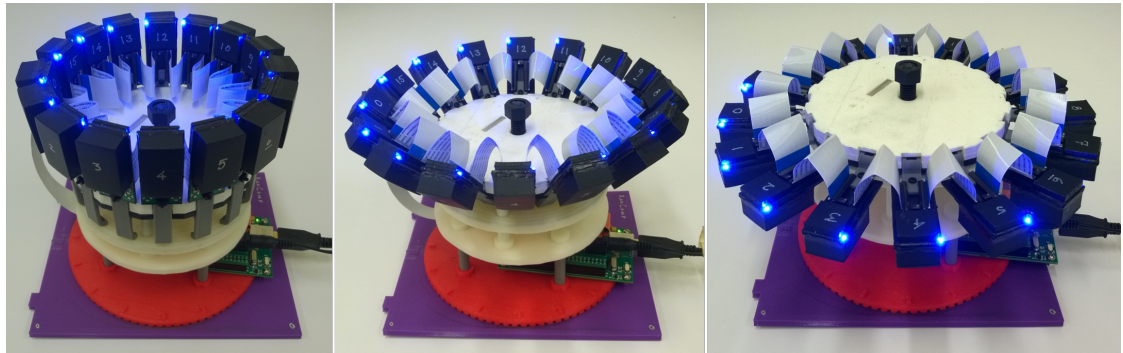
Figure 3.3: Radiation Compass prototype assembled in the Advanced Radiation Instrumentation Laboratory at OSU.

radiation detector panels arranged in a circular configuration. The detector panels are also able to change their pitch in a 90° arc thanks to an articulation platform to which the panels are mounted, also shown in Figures 3.3 3.4, affording the detector sensitivity to the distance of the source relative to the detector. Though the complete radiological search system includes a UAV and a detection system
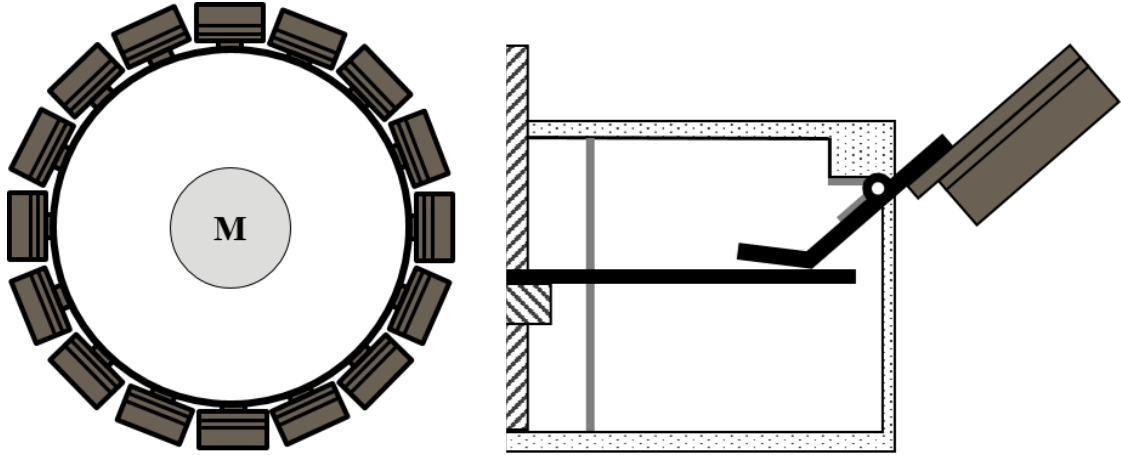
Figure 3.4: Illustration of the Radiation Compass design both a) from the top, and b) a cutaway view from the side.

capable of estimating the source direction and identifying the source upon finding it, the Radiation Compass does not perform the spectroscopy and identification duties of this system. Source identification is handled by a separate gamma ray spectrometer that will be discussed at the conclusion of this work (Chapter 5). The Radiation Compass center is defined as the vertical center of the BGO elements, as shown by the dot in Figure 3.5a, and as the center of the circle of the detector panels in the horizontal plane, shown by the dot in Figure 3.5b.

The basic mechanism behind the direction-sensitivity of the Radiation Compass is that of a passive mask, the concept of which is illustrated in Figure 3.6. When a radiological point source is located on the vertical center line amongst all of the detector panels, the count rate of all panels is equal within the bounds of radiation counting statistics since the panels have identical counting geometry and detector material, as shown in Figure 3.6a. However, when the same point source
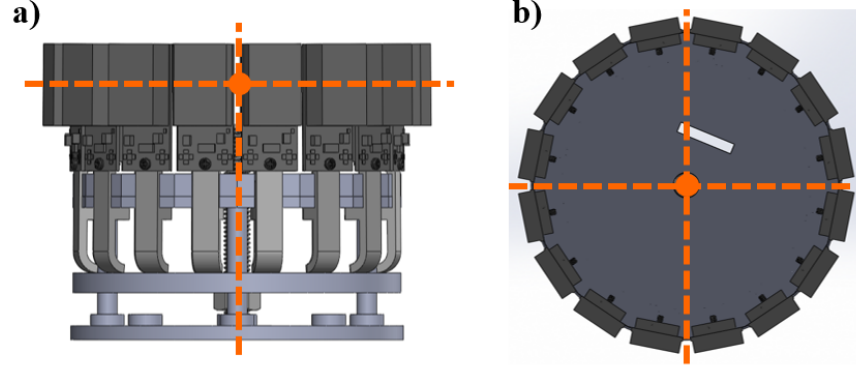
Figure 3.5: Illustration of the Radiation Compass, illustrating the center in the a) vertical and b) horizontal planes by the location of the dots.

is moved away from the Radiation Compass, outside the circle of detector panels, those detector panels closer to the source attenuate the gamma ray flux from the source, and thus show a higher count rate than those on the opposite side of the detector, shown in Figure 3.6b. The pattern of count rates reflects the effect of the attenuation of the gamma ray flux and changes depending on the source location relative to the established detector orientation, marked in Figure 3.6a.

Since the Radiation Compass system does not need to estimate the emission intensity of the radiological source it is used to search for, the detector count rate pattern is simplified from the count rate in each panel to the ratio of the count rate in each panel to the total count rate among all panels:

$$d_i = \frac{R_i}{\sum_i R_i}, \tag{3.1}$$

where d_i is the detector panel weight, and R_i is the count rate in panel i. The
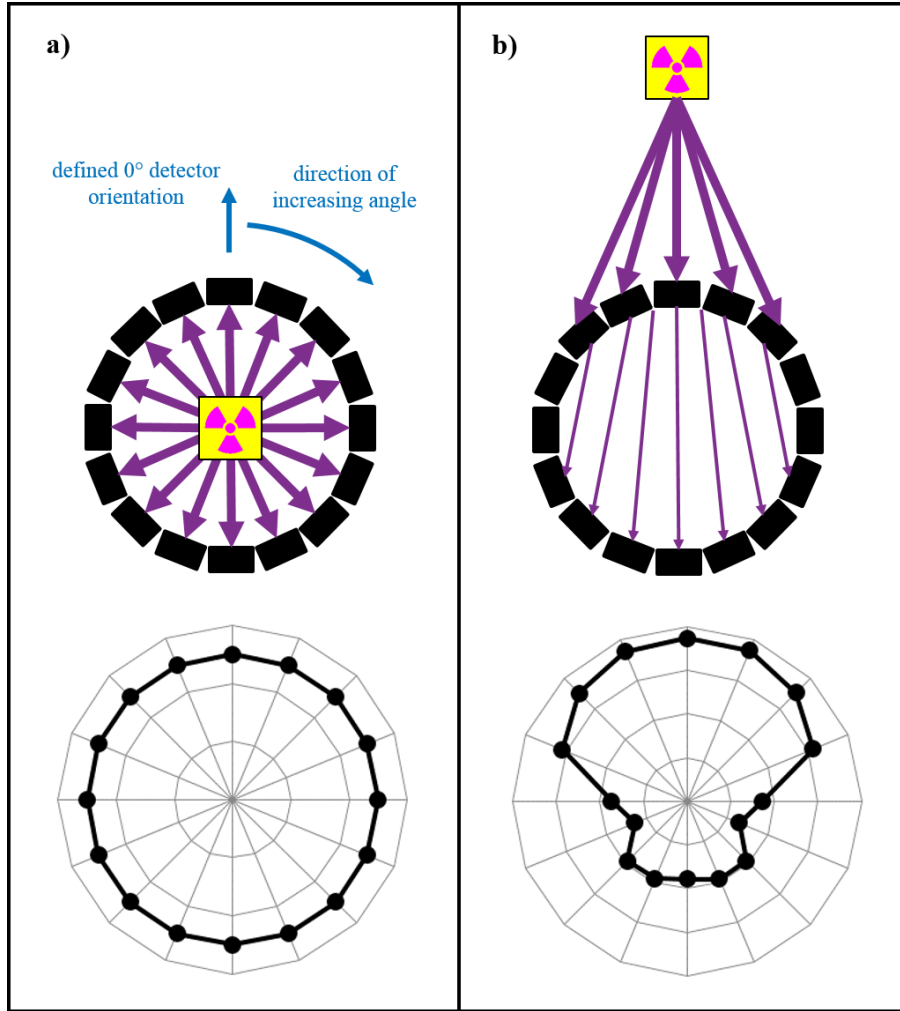
Figure 3.6: Illustration of the passive mask concept with source both a) point source centered amongst all panels, and b) point source located outside the circle of detector panels.

set of detector panel weights generated by the Radiation Compass in response to the presence of a radiological source is referred to as the "detector response".

The following sections detail the fabrication, assembly, simulation, and characterization of the Radiation Compass, as well as a description of the direction

estimation methods applied to the detector.

3.1.2 Assembly

3.1.2.1 Detector Panels

Each detector panel is comprised of a detection element and readout electronics all mounted on a printed circuit board (PCB). The detection element consists of a 25 x 15 x 8 mm^3 BGO scintillator crystal optically coupled to a surface-mounted SiPM. BGO was chosen as the detector material since it has a high effective atomic number and high density, affording it high gamma ray detection efficiency in a small volume compared to other scintillation materials, such as CsI(Tl). In addition, BGO does not need to be sealed against moisture since it is not hygroscopic, and is a currently-available, off-the-shelf scintillator material that has been used for decades and is relatively low-cost since the manufacturing process is well known. Since the panels do not perform energy spectroscopy, the comparatively poor energy resolution of BGO was not a concern. Other detector materials can be used, but all possess significant disadvantages: single-element semiconductors, gas-based detectors, and organic scintillators are not as efficient for gamma ray detection, and multi-element semiconductors are much more expensive. As mentioned previously, the detector panels can be made sensitive to neutrons by changing the scintillator element used should a particular scenario or application warrant it. Neutron-sensitive elements were not used in the design

presented here since neutron-sensitive materials like Stilbene and CLYC are less efficient for gamma ray detection.

The SiPM was chosen as the light-collection device for the detector panels over the more traditional PMT for a number of reasons, including its smaller size, lower weight, and better durability. SiPMs also use a lower bias voltage than PMTs, are insensitive to magnetic fields, and cost less than PMTs. In addition, more recent SiPM models are able to be surface-mounted to PCBs, further saving space and weight. When compared to the design qualities listed above, the SiPM is revealed to be a much more appropriate choice for the Radiation Compass than the PMT. The SiPM used on the Radiation Compass detector panels was the SensL MicroFB-60035 series blue-sensitive model [51], which was well-suited to the blue-emitting BGO. Figure 3.7 shows the photon detection efficiency (PDE) of the SiPM compared to the emitted light wavelength distribution from the BGO [52,53]. The specifications of SiPM and the BGO crystal are listed in Tables 3.1 and 3.2, respectively [51, 52].

Table 3.1: Table of SiPM specifications.

SiPM parameter	value
density	7.13 g/cm^3
decay constant	300 ns
peak scintillation wavelength	480 nm
photons/MeV	8,500

The SiPM and accompanying readout electronics were implemented on a 20 x 45 mm^2 PCB, shown in Figure 3.8. The PCB was itself designed as part of the structure of the Radiation Compass, and possesses a 2.5 mm diameter hole
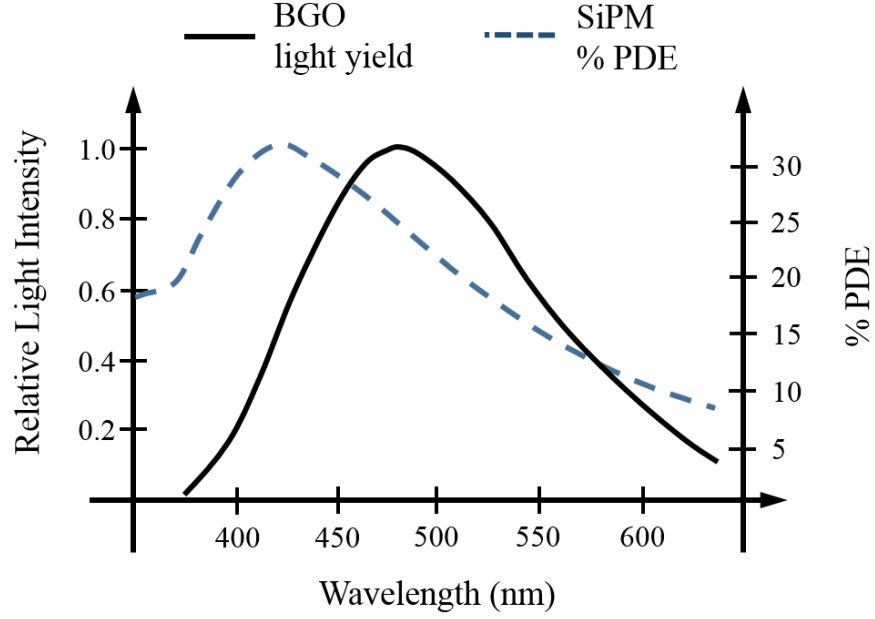
Figure 3.7: Illustration of BGO light yield [52] and SiPM percent PDE [51] as functions of wavelength.

Table 3.2: Table of BGO specifications.

BGO parameter	value
breakdown voltage (typ.)	24.5 V
number of microcells	18980
fill factor	64%
wavelength of peak PDE	420 nm
PDE at peak sensitivity (2.5 V_{ov})	31%
gain	$3x10^6$
dark current (typ/max)	10 μA / 24 μA
crosstalk probability (2.5 V_{ov})	10%

at one end as a mounting point to the articulation array. Figure 3.8 also shows some electronic components whose purpose in the readout electronics is explained in Section 3.1.3 but which are referenced as physical components in this section,
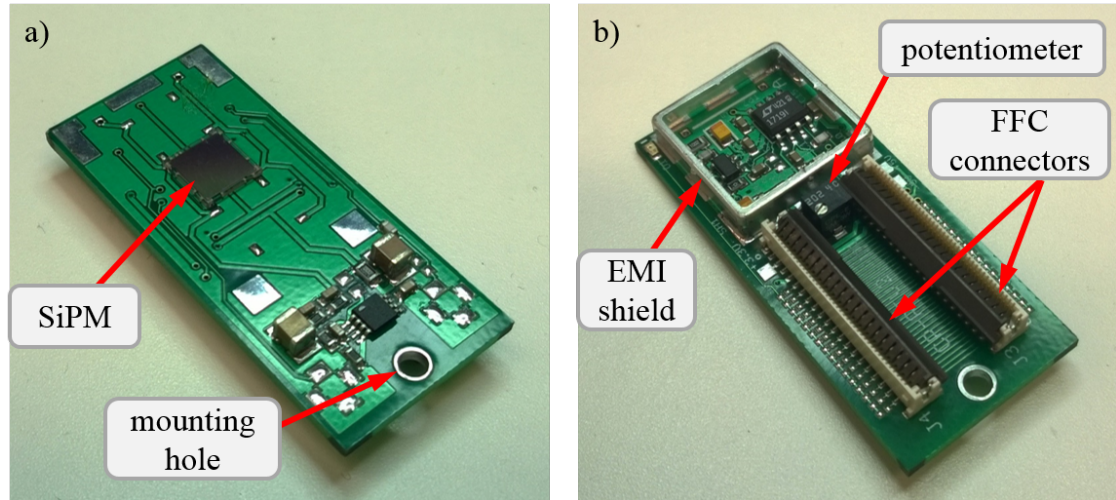
Figure 3.8: Photos of a detector panel PCB, showing the light readout, electronics, and structural components.

including the electromagnetic interference (EMI) shield, potentiometer, and flat, flexible cable (FFC) connectors.

Because the direction-sensitivity of the device is based on the detector panels having a uniform detector response, within radiation counting statistics, to a radiological source at the Radiation Compass center, it was of paramount importance that the panels be designed and assembled using the same procedure and techniques on each one. Therefore, the assembly of each detector panel followed a specific set of procedures in order to achieve the best practical uniformity of detector response across all detector panels.

The first procedure was that of wrapping the BGO crystal in a diffuse reflective material in order to improve the light collection efficiency of each panel. Wrapping the BGO was complicated by surface-mounted SiPM since wrapping the entire

PCB was impractical and the SiPM could not be wrapped separately. A reflective spacer was designed in order to resolve this issue. The spacer has a hole large enough for the SiPM at its center, and fits around the SiPM, both providing a large flat surface for the BGO to lie on and providing the reflective material to improve the light collection. The assembly procedure for the reflective spacer is shown in Figure 3.9. Each spacer was first cut from 254 μm white Delrin using a Roland EGX-350 desktop engraver [54] (Figure 3.9a). Double-sided tape was then applied to the spacer to completely cover the spacer surface and the center SiPM hole (Figure 3.9b), and then trimmed to be flush with the spacer outer edges (Figure 3.9c). White, 0.8 mm thick Teflon (PTFE) film [55] was then carefully adhered to the double-sided tape (Figure 3.9d), smoothed over the spacer (Figure 3.9e), and trimmed to be flush with the spacer outer edges (Figure 3.9f). The resulting PTFE-covered spacer (Figure 3.9g) was then flipped over and the center SiPM hole cut from the tape and PTFE layer (Figure 3.9h) resulting in the finished reflective spacer (Figure 3.9i). Reflective plates, identical to the reflective spacers except that it had no hole for the SiPM, were fabricated using the same method as the reflective spacers.

The next step in wrapping the BGO crystal was to place the two plates on either side of the 25 x 15 mm^2 face, and then wrap the sides of the BGO still uncovered with additional PTFE, shown in Figure 3.10. This completed the BGO wrapping procedure.

The next procedure was to optically couple the wrapped BGO to the SiPM as well as secure the crystal to the PCB. The coupling and securing procedure
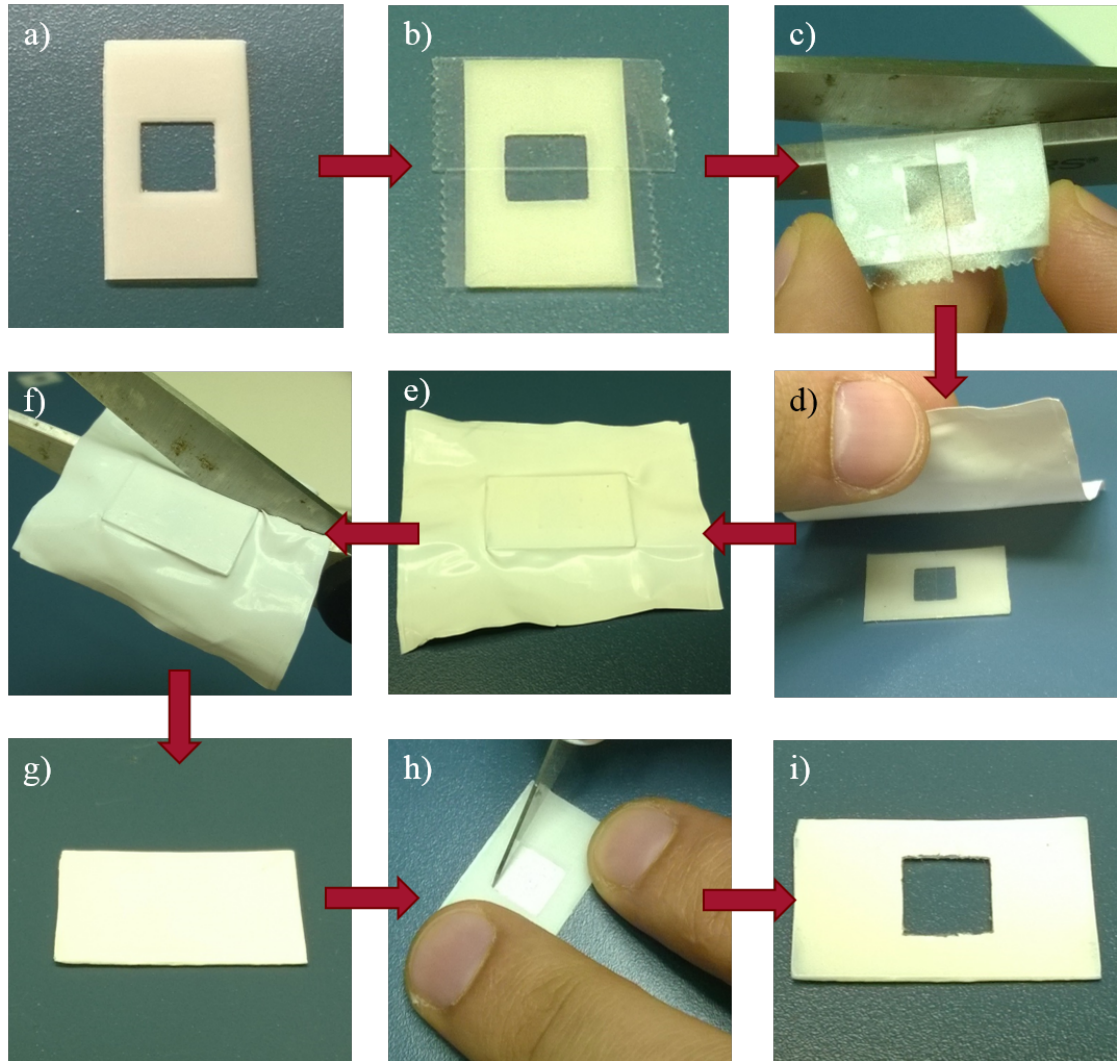
Figure 3.9: Photos of the reflective spacer assembly procedure: a) the spacer cut from 254 µm thick Delrin, b) double-sided tape applied, c) double-sided tape trimmed on outer edges, d) 80 µm thick PTFE applied, e) PTFE pressed smooth against the spacer, f) PTFE trimmed on outer edges, g) trimmed reflective spacer, h) tape and PTFE trimmed from SiPM hole, i) finished reflective spacer.

was again complicated by the surface-mounted SiPM. The coupling and securing

procedure is shown in Figure 3.11. The SiPM was first coated with BC-630 silicone
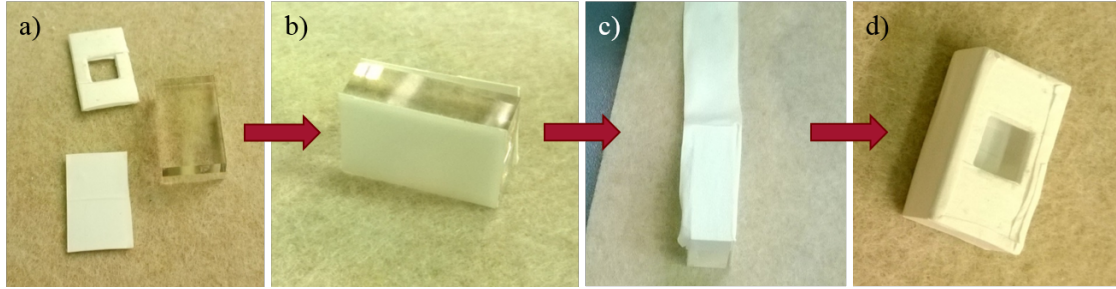
Figure 3.10: Photos of the BGO wrapping process: a) reflective spacer and plate and BGO crystal, b) reflective plate and spacer positioned on either side of the BGO, c) wrapping the BGO sides with PTFE strips, and d) completed reflectively-wrapped BGO crystal.

grease [55] to better match the refractive indexes of the BGO and SiPM window (Figure 3.11a). Optically-opaque black tape [56] was then adhered to the PCB around the SiPM (Figure 3.11b). The BGO crystal was then carefully placed over the SiPM, and the black tape folded over the BGO assembly (Figure 3.11c). The adhesive side of the tape was oriented outward from the BGO so that it would not adhere to the PTFE wrapping and displace it during the assembly process (Figure 3.11d). A 3-D printed cover was then placed over the tape-wrapped crystal assembly and glued directly to the PCB (Figure 3.11e and f). While the original design called for an aluminum cover to be soldered in place on a set of pads on the PCB, the availability of 3-D printing at the OSU school library quickly replaced the original design due to its ease and speed of fabrication, lightweight nature, low atomic number, and low cost.

The final procedure was to light-seal the panel assembly, which is shown in Figure 3.12. Light was found to be able to penetrate the rear of the PCB and reach the SiPM, so the PCB needed to be sealed. Light sealing the panels was again
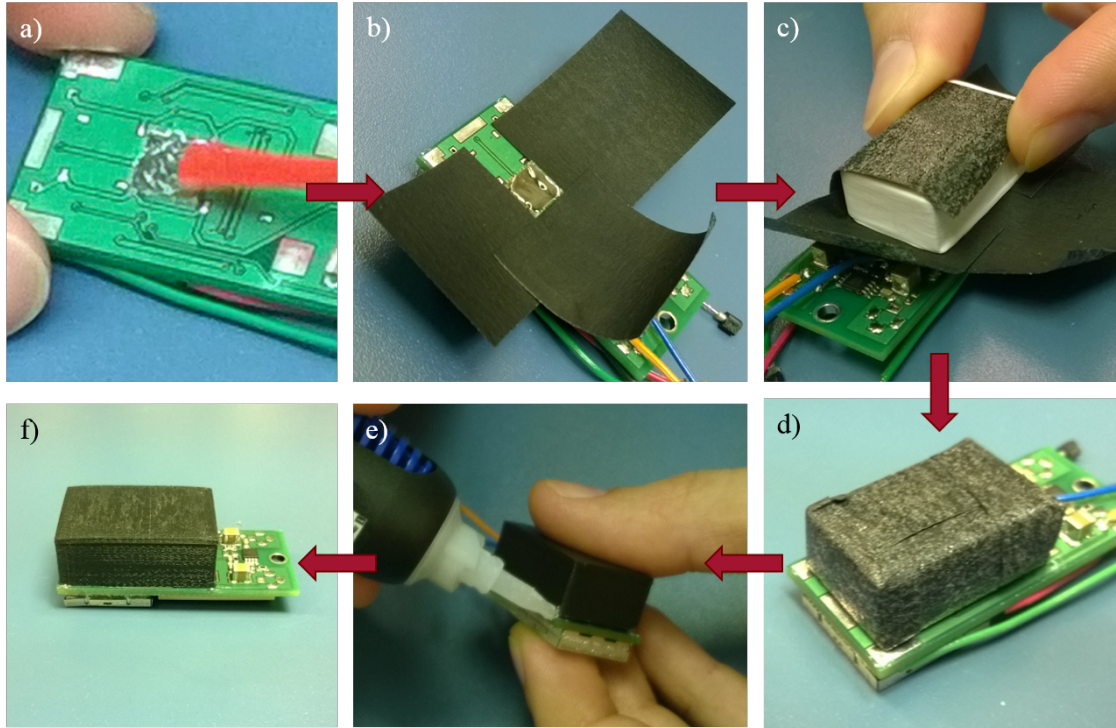
Figure 3.11: Photos of the BGO optical coupling process: a) applying optical grease to the SiPM, b) placement of strips of light-opque black tape, c) mating the wrapped BGO to the SiPM, d) folding and adhering the black tape around the BGO, e) 3-D printed cover placed of the BGO assembly and glued in place, f) panel assembly finished.

a delicate procedure since the connection headers on the PCB needed to remain uncovered in order to be able to connect the detector panels to the readout system. Therefore, the first step in the light-sealing procedure was to apply a low-viscosity black epoxy between the FFC connectors and the PCB (Figure 3.12a) and around the edges of the EMI shield. The next step was to apply several coats of liquid electrical tape to the gap between the 3-D printed cover and the PCB (Figure 3.12b). Finally, sensitive components on the PCB, such as the potentiometer,
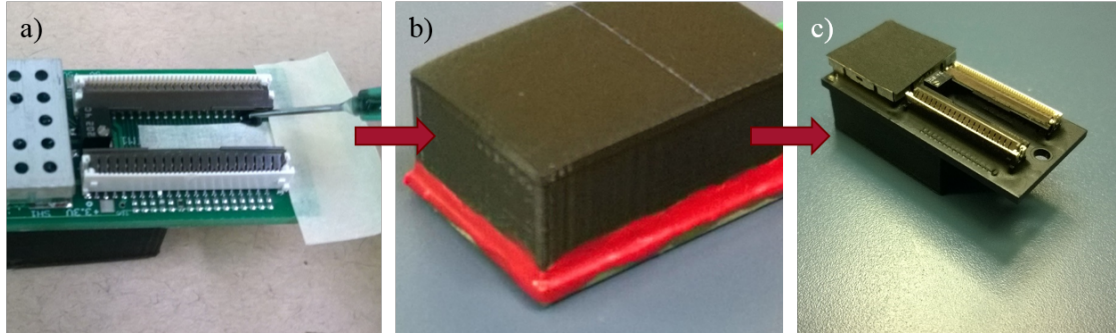
Figure 3.12: Photos of the light-sealing process: a) application of the low-viscosity black epoxy to the FFC connectors, b) application of liquid electrical tape around the edges of the 3-D printed cover, c) final light-sealed panel after application of black paint.

connectors, and LED, were covered with masking tape and the panel sprayed with matte black paint as a final layer of light sealing (Figure 3.12c). The EMI shield covering the readout electronics of the detector panel was also covered with a strip of black tape, so as not to completely seal off the electronics underneath but still seal against light.

3.1.2.2 Articulation Platform

The articulation platform is based on the simplest design for changing the pitch of the detector panels attached to it, shown as an illustration in Figure 3.13. Each detector panel is mounted on a panel lever, which is in turn mounted on a cylindrical articulation frame. The panel lever is held in place only by a pin, creating a fulcrum. A torsion spring is mounted around the pin, and its ends braced against the articulation frame and the lever itself. A threaded rod runs through
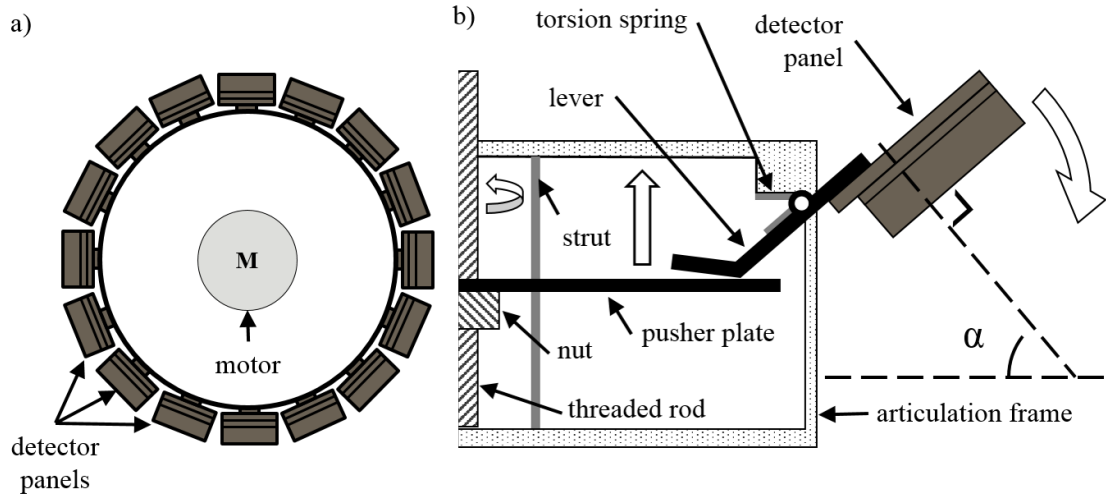
Figure 3.13: Illustration of the articulation platform with attached detector panels a) from the top, and b) from the side, with labeled components.

the middle of the articulation frame. A nut connected to a pusher plate is threaded around the rod. Struts supporting the upper portion of the articulation frame run through the pusher plate, making it unable to rotate. Thus, when the threaded rod is rotated clockwise, the pusher plate is moved upward due to the threading on the nut. The pusher plate presses against the end of the panel lever, rotating it around the fulcrum of the pin, changing the angle of the detector pattern. When the threaded rod is rotated anti-clockwise, the pusher plate is moved downward, removing the pressure against the end of the panel lever. The torque provided by the torsion spring is enough to overcome the weight of the detector panel at the end of the panel lever and return the lever and panel to their original position. The angle of the panel rotation, called the "view angle", is denoted by α in Figure 3.13b and defined as the angle between the line perpendicular to the 25 x 15 mm^2

face of a given panel and the plane of the ground. The view angle is able to be changed continuously between 0° and 90°.

The fabricated articulation platform was designed in SolidWorks [57] and assembled using a combination of 3-D printed pieces and low-cost off-the-self components. The 3-D printed pieces were made using the Oregon State University Valley Library's 3-D printing service, which uses a Makerbot Replicator 2 [58]. 3-D printing, also called additive manufacturing, was used to fabricate pieces of the articulation platform for several reasons. First, the material used, polylactic acid (PLA) [59], is a lightweight, low atomic number plastic, both qualities among the desired detector qualities. Second, the material is low-cost and the fill-factor used for parts on the articulation platform was 30% to save weight and cost, with a hexagonal internal structural pattern generated by the 3-D printer software. Finally, the low cost and fast turn-around time of the 3-D printed parts allowed the design of the articulation platform to undergo rapid prototyping and resulted in a more refined version to ultimately be used.

The articulation platform used in this work is shown in Figure 3.14. Instead of having the articulation frame in Figure 3.13, an articulation plate and base plate, linked by the struts, were used for structural components of the design. This saved additional weight by removing the side walls of the original articulation frame design. An exploded view of the articulation platform components, except for the panel levers, torsion springs, and lever pins, as drawn in SolidWorks is shown in Figure 3.15. The distance between the center of the articulation plate and the center point of the lever rotation is based on the minimum spacing practical
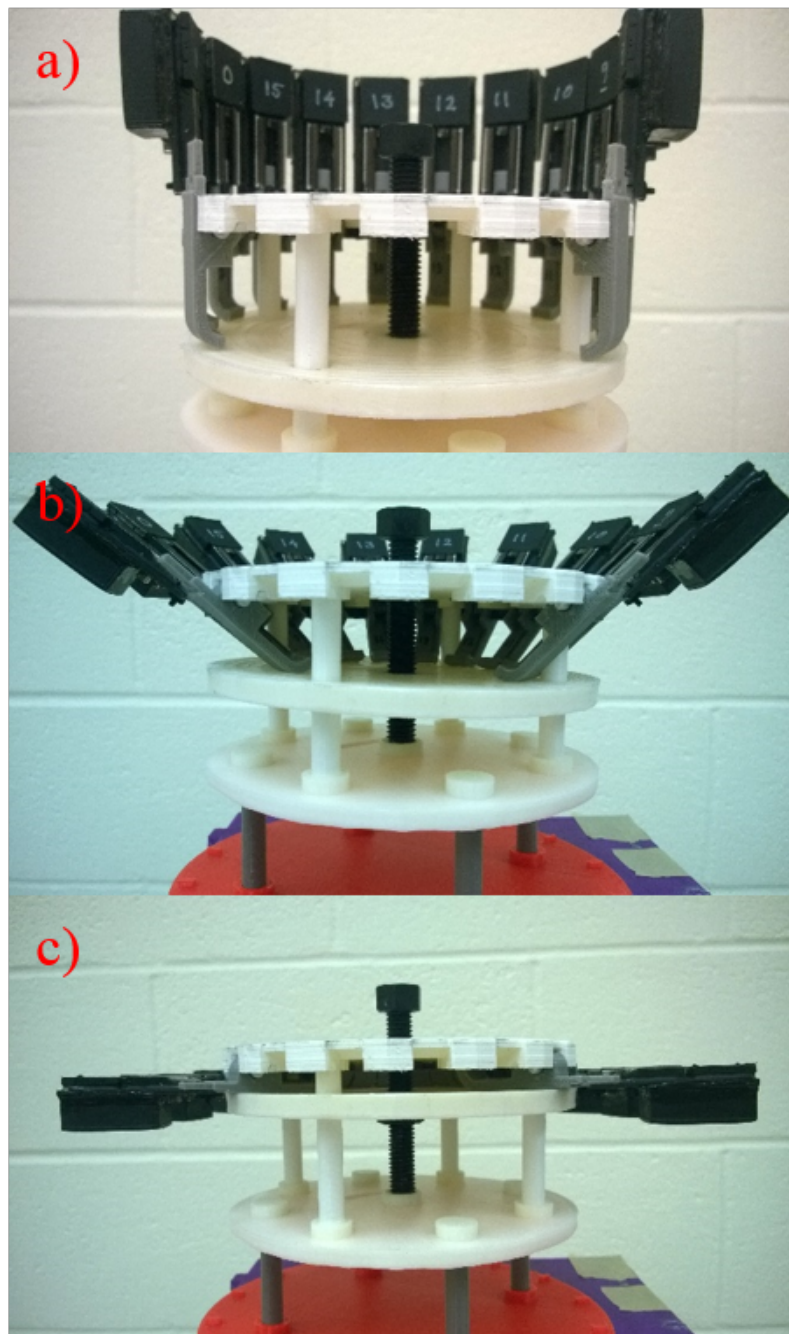
Figure 3.14: Photos of a pseudo-cutaway view of the articulation platform with the levers at the a) 0°, b) 45°, and c) 90° view angles.
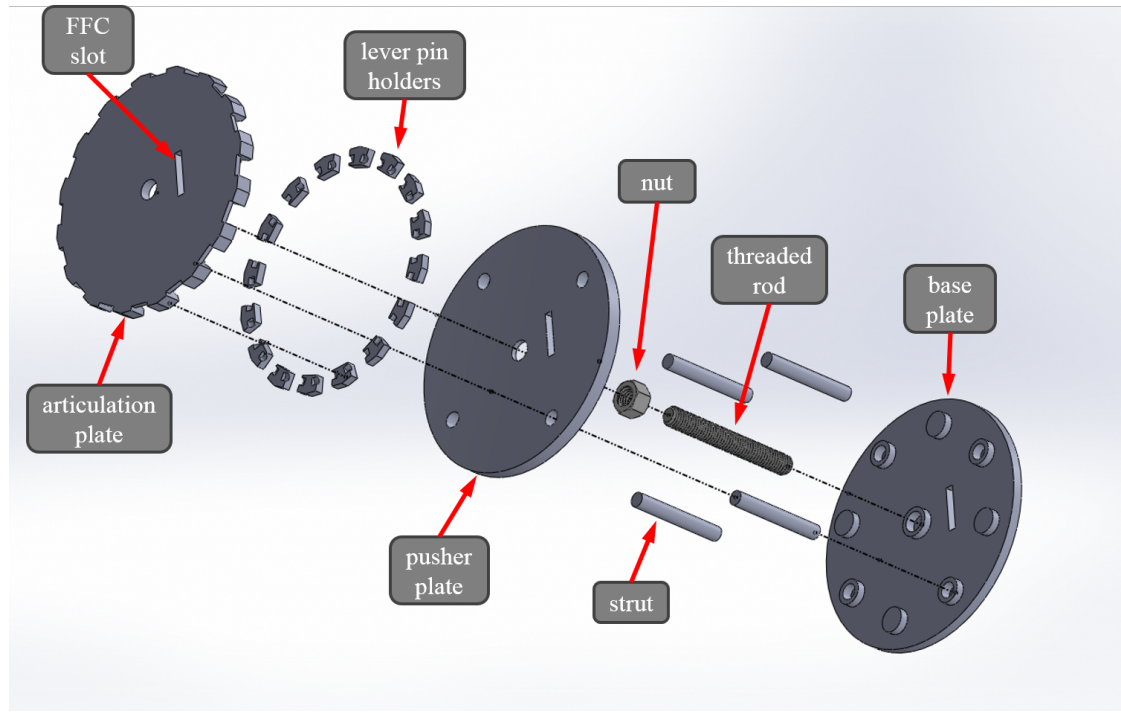
Figure 3.15: Illustration of an exploded view of the articulation platform with all components labeled.

between detector panels. The articulation plate, pusher plate, base plate, and lever pin holders were all 3-D printed. The articulation plate, pusher plate, and base plate have a rectangular slot to accommodate the FFC connecting the panels to the readout electronics, as described in Section 3.1.3.

Figure 3.16 shows both the lever design and one 3-D printed panel lever. The lever main features, marked in Figure 3.16a, are the curved end, the stop-shelf, and the panel mounting point. The curved bottom end provides leverage for the pusher plate to start the rotation of the lever. The stop-shelf prevents the lever from rotating beyond its 90° view angle range. Finally, the panel mounting point
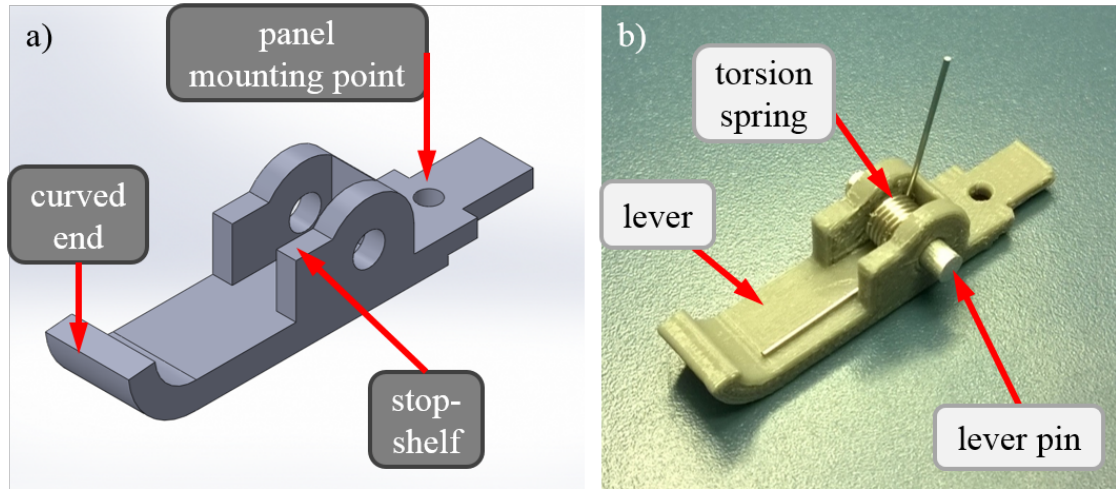
Figure 3.16: Illustration (a) and photo (b) of a panel lever highlighting the design features and components, particularly the torsion spring and lever pin, used for lever rotation and not visible in other illustrations and photos.

consists of the 2.5 mm diameter hole, the same size as the hole on the detector panels, and the extended top. This part of the lever fits between the two FFC connectors, shown in Figure 3.17 on the detector panel and prevents the panel from changing its roll. Figure 3.16b shows the 3-D printed lever with the lever pin and torsion spring in place. The lever pins were made by cutting a 3.175 mm diameter aluminum rod into 16 mm lengths, and the 120°, 0.0373 N-m torsion springs were purchased and used off-the-shelf.

A photo of the partially-assembled articulation platform is shown in Figure 3.18. As shown in the illustration in Figure 3.13, the ends of the torsion spring in Figure 3.18 are braced against the bottom of the articulation plate and the panel itself. The articulation plate shown in Figure 3.18 is from an earlier version of the design that did not include the FFC slot. The articulation platform used in this
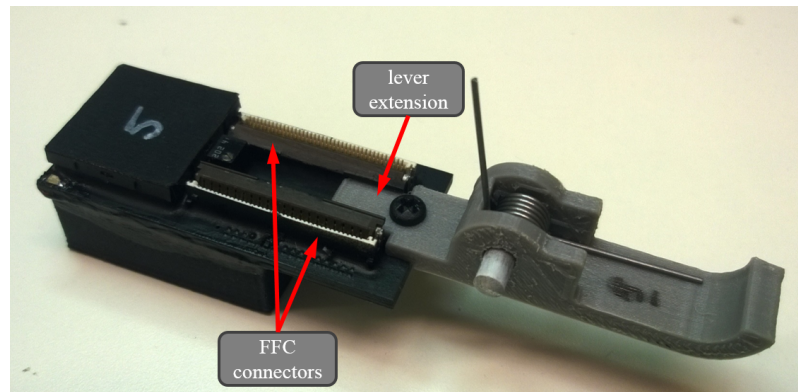
Figure 3.17: Photo of a detector panel mounted to a panel lever. The extension of the panel lever that fits between FFC connectors on the panel prevents the panel from rolling.
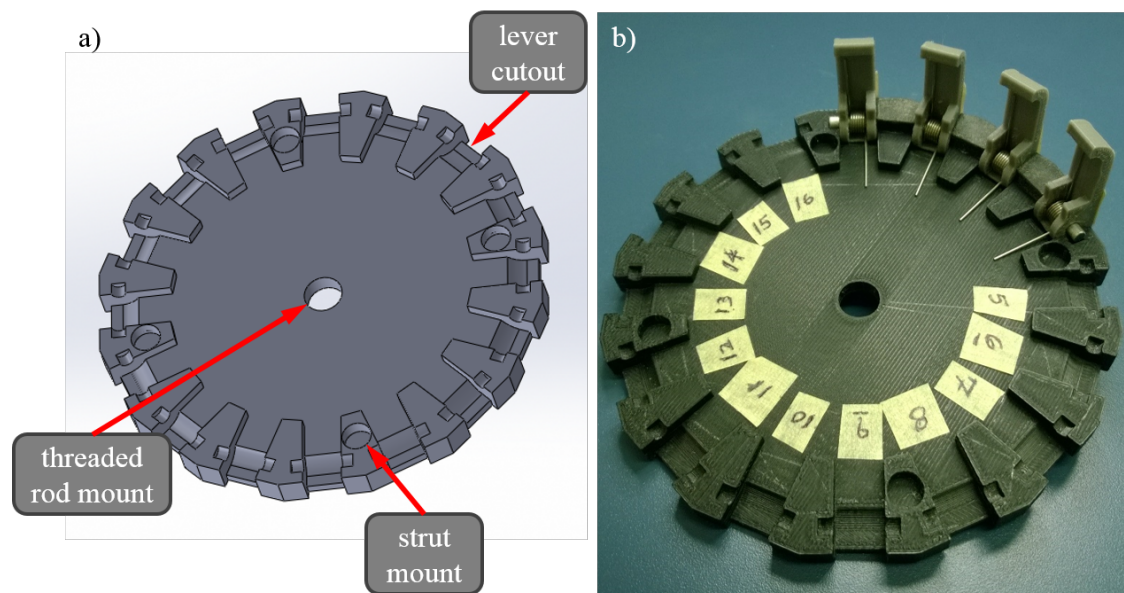
Figure 3.18: Partial assembly of the articulation platform, showing the panel levers secured in place with pins affixed between the articulation plate and lever pin holders.

work did not include the motor shown in Figure 3.13 and the threaded rod was instead turned by hand.

3.1.2.3 Measurement Apparatus

In order to take measurements with more accurate geometric arrangements, several measurement apparatus were designed and 3-D printed. First, an apparatus was designed and printed in order to center a laboratory check source, both vertically and in the circle of panels, as shown in Figure 3.19. The source centering apparatus
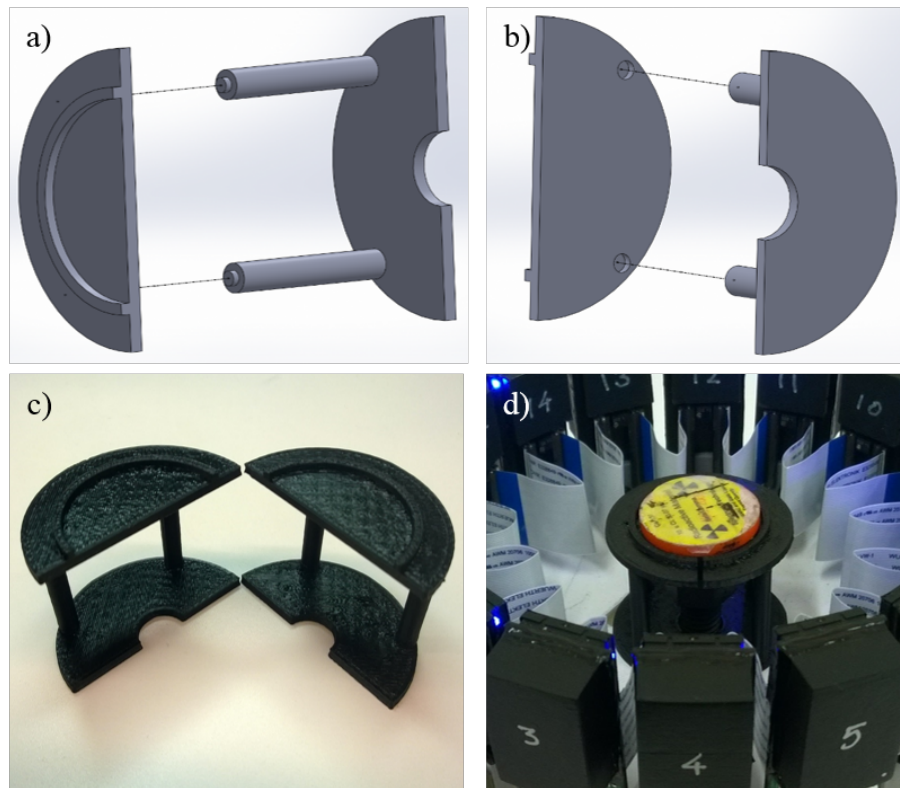
Figure 3.19: Source centering apparatus illustrations and photos.

was printed in two sets of two parts, illustrated in Figure 3.19a and b, and then glued together and used as shown in Figures 3.19c and 3.19d.

The other apparatus consists of a set of parts, shown in Figure 3.20, that enable radioactive laboratory sources to be placed a specific location relative to the center of the Radiation Compass. The detector track and source track establish the set of distances at which a source can be set. Each of the cross-bars of the source track are spaced 5 cm apart. The small rotation pin is placed in the rotation slot of the detector track and into a slot on the bottom of the measurement plate. The measurement plate possesses small cutouts around the bottom edge every 4.5°, with small rectangular ridges on the top indicating the position in front of each detector panel. The combination of features allows the measurement plate to be placed onto the detector track, and cutout in the measurement plate slotted to the angle ridge on the detector track, locking the angle of the Radiation Compass relative to the source. The slot in the detector track allows the Radiation Compass to slide back, rotate, and a cutout along a new angle slotted to the angle ridge. The struts on the measurement plate slot into holes on the underside of the Radiation Compass base plate. The source pedestal has a set of crossed grooves at its base that allows it to be set into position at any of the source track cross-bars. The groove at the top of the source pedestal allows the two source clamp halves to be fitted together and slotted there. The source clamp halves also have holes that are used to fasten them togther, though the screws and nuts used for this purpose are not shown in the illustration.
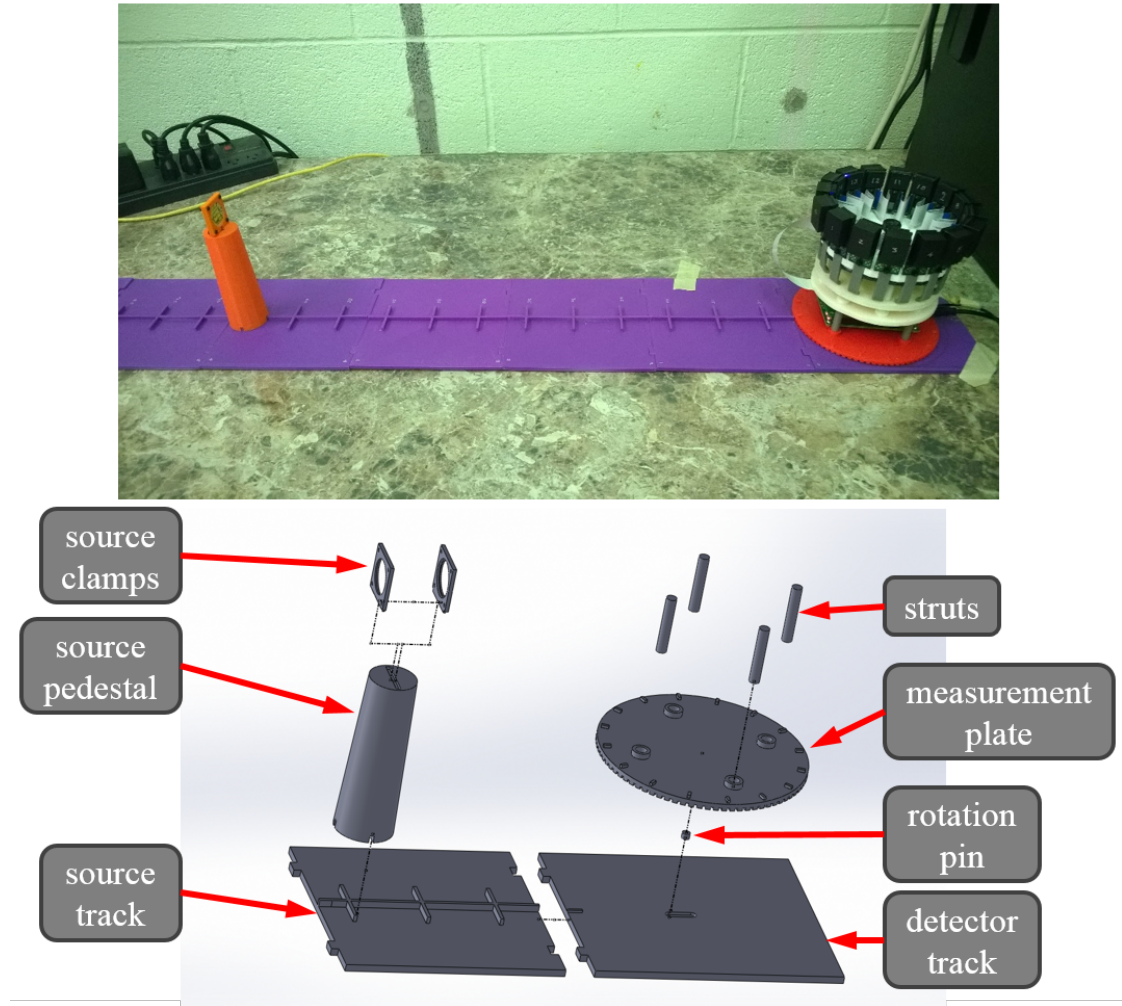
Figure 3.20: Radiation compass measurement apparatus both a) set up in the laboratory and b) in an illustrated, exploded view.

3.1.3 Detector Electronics

The Radiation Compass electronics are illustrated in Figure 3.21, and can effectively be split into two parts: the front-end electronics on each panel, and the panel readout system.

3.1.3.1 Front-End Electronics

The front-end electronics were implemented on the 20 x 45 mm^2 PCBs of each panel. The bias voltage, V_{bias}, is applied to each panel, where it passes through a linear voltage regulator, V_{SiPM} regulator, to reduce the amount of noise applied to the SensL MicroFB 60035-series SiPM [51], as shown in Figure 3.21. The SiPM standard output is connected to a preamplifier with a feedback resistor and capacitor. The preamplifier is based on a FET-input, low-noise (7nV/Hz) operational amplifier. The preamplifier output is connected to the signal input of the comparator. The other comparator input is connected to a voltage threshold that is able to be adjusted by a potentiometer, which is in turn connected to both a
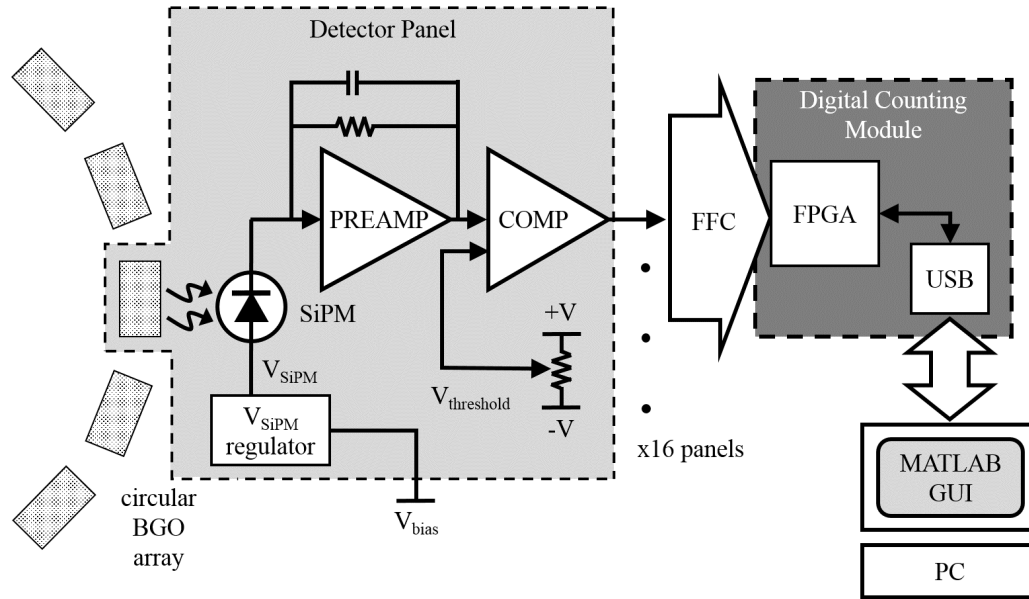
Figure 3.21: Radiation Compass electronics illustration.

+5 V and -5 V DC rail. The comparator has dual-polarity input and a rail-to-rail CMOS output, which can each be operated at separate voltages, as well as external, resistor-adjustable hysteresis. When pulses arrive at the comparator input, the comparator output changes its binary state once the pulse voltage has exceeded the upper voltage threshold. The comparator output changes back to its original binary state once the pulse voltage has decreased below the lower voltage threshold. Example pulses and their relation to the comparator output and threshold voltages are shown in Figure 3.22. The upper and lower voltage thresholds are separated by
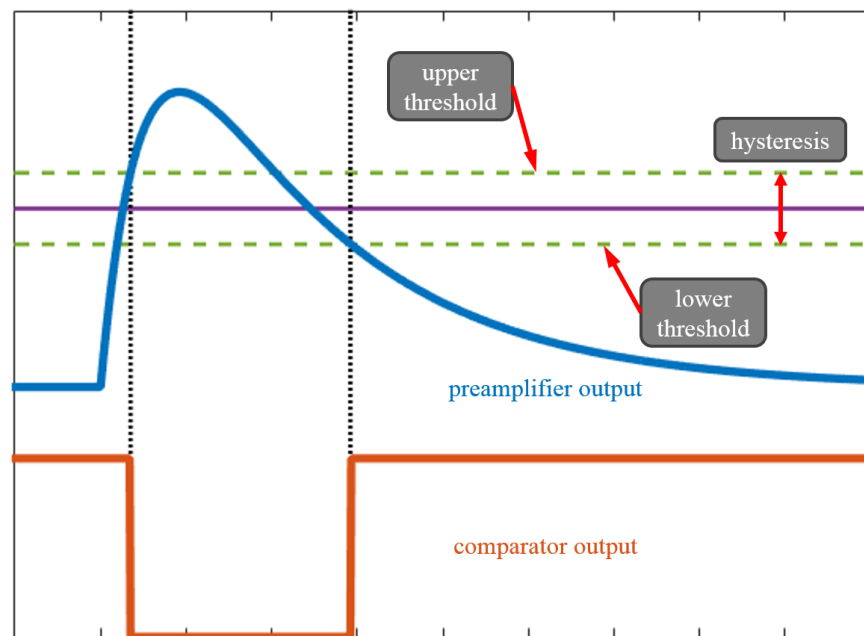
Figure 3.22: Example preamplifier pulse and corresponding example comparator logic pulse output.

the hysteresis voltage, which was set to 50 mV. The preamplifier and comparator thus convert the current pulses from the SiPM into low-voltage CMOS digital pulses. The preamplifier and comparator are both located inside an EMI shield on the side of the PCB opposite that of the SiPM and BGO, shown in Figure 3.23.
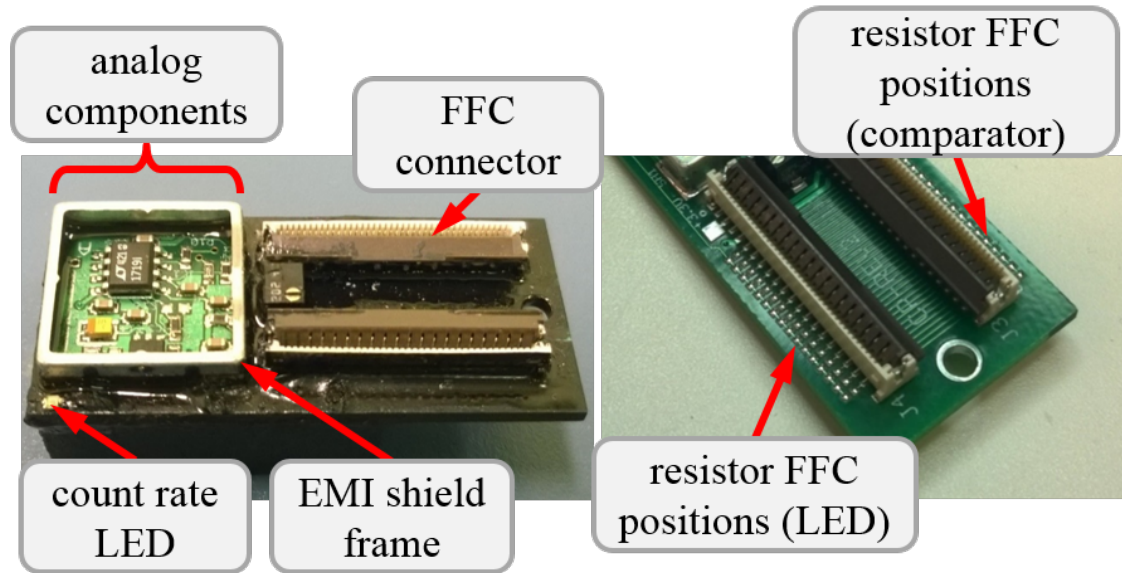
Figure 3.23: Back of a detector panel with the cover of the EMI shield removed to show the components underneath.

Each detector panel mounts two FFC connectors each with 40 positions. The lead on each FFC connector is connected to the corresponding lead on the other FFC connector, creating 40 channels (wires). The comparator output on each panel is connected to its own channel by means of a jumper (0 Ω resistor) soldered into one of sixteen positions on each panel, as shown in Figure 3.23. Each panel also mounts a blue LED to visually indicate the count rate intensity, and each LED is also connected to a different channel on the FCC connectors by a 30 Ω resistor.

The panels are then daisy-chained together with FFCs, with the last panel in the chain connected to the digital counting module. Thus, each channel of the FFC chain carries a different signal: 16 channels carry the comparator output signals from each of the detector panels, 16 channels carry the LED input signal to the detector panels, and the remaining channels carry the panel supply voltages and ground.

3.1.3.2   Panel Readout System

The panel readout system consists of the digital counting module and a PC, as diagrammed in Figure 3.24. The digital counting module, shown in Figure 3.25, consists of an interface board and a FPGA integration module. The interface board was designed in-house and is connected directly to the FPGA integration board via two 50-pin headers. The 50-pin headers on the interface board are connected to the FCC connector in order to connect the panel signals to the FPGA. The interface board also generates the +5 V and -5 V used by the preamplifier and comparator, and the negative bias voltage V_{bias} for the SiPM. As mentioned previously, each comparator panel hosts its own linear regulator for the SiPM bias since the main bias voltage is generated by a switching regulator on the interface board. The power used by each detector panel is 0.17 – 0.19 W, making the total detector power consumption 2.7 – 3.0 W, depending on the number of times the LED is turned on per second.

The FPGA integration board [60] features a Xilinx Spartan 6 FPGA, two 50-pin
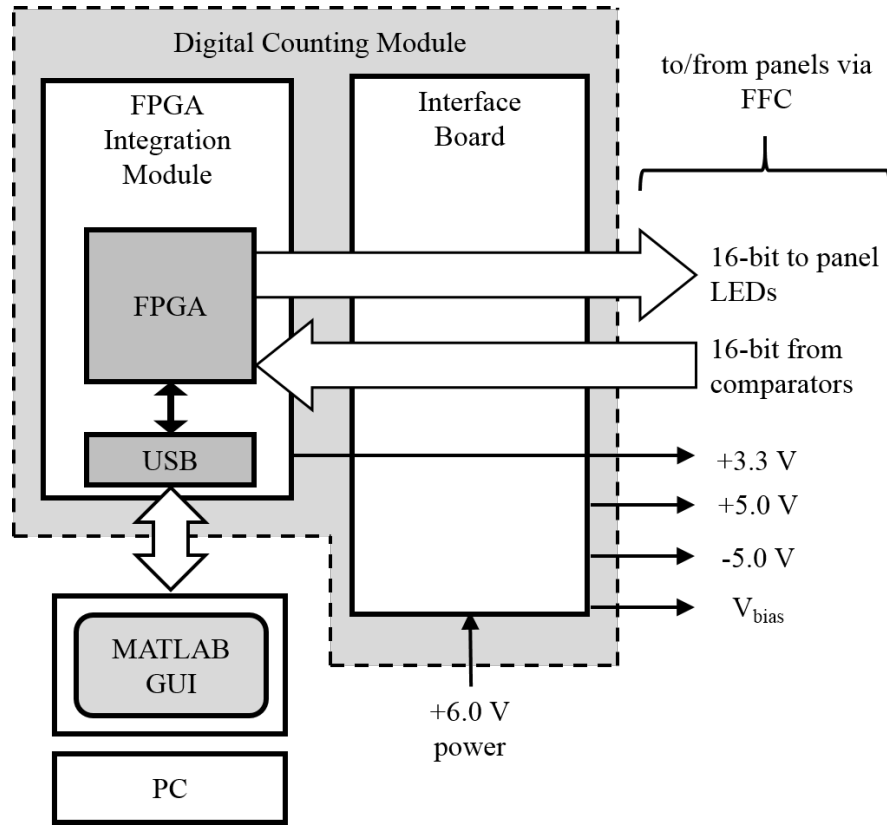
Figure 3.24: Illustration of the components and signal routing of the panel readout system.

headers, and a USB interface port. The two 50-pin headers are connected to the interface board to transfer the comparator and LED signals to and from the panels. The headers also transfer +3.3 V, generated by the FPGA integration board, to the comparator output supply via the adapter board. The FPGA is responsible for counting the number of binary pulses from the comparator outputs, and returning longer binary pulses to the detector panel LEDs. For prototyping purposes, the user is able to communicate with the FPGA via USB interface. This allows the
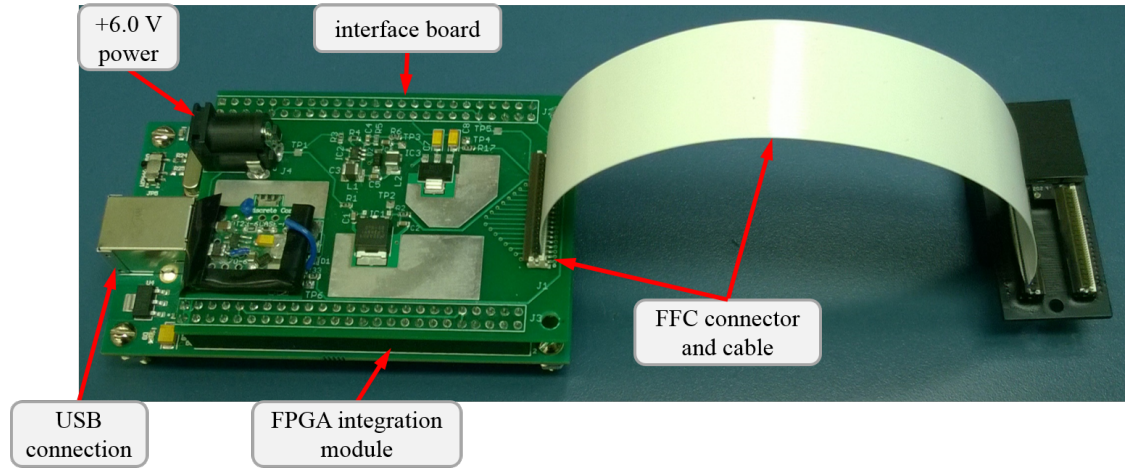
Figure 3.25: Photo of the digital counting module, with the interface board and FPGA integration module.

user to change FPGA firmware settings and collect the data recorded by the FPGA via user interface hosted on a PC, as described in the next section.

3.1.3.3 Readout Firmware and User Interface

The FPGA firmware consists of several modules that count the randomly-occurring binary comparator pulses in parallel. The firmware modules and the output signal of each are illustrated in Figure 3.26. The comparator signals first pass through a synchronizing module which synchronizes the random comparator signals to the 100 MHz FPGA processing firmware. The signals are then routed to a debouncing module to suppress multiple comparator pulses that arise due to ringing associated with fast transition times. The output of the debouncing module is connected to one-shot generator module. The one-shot generator module consists of two
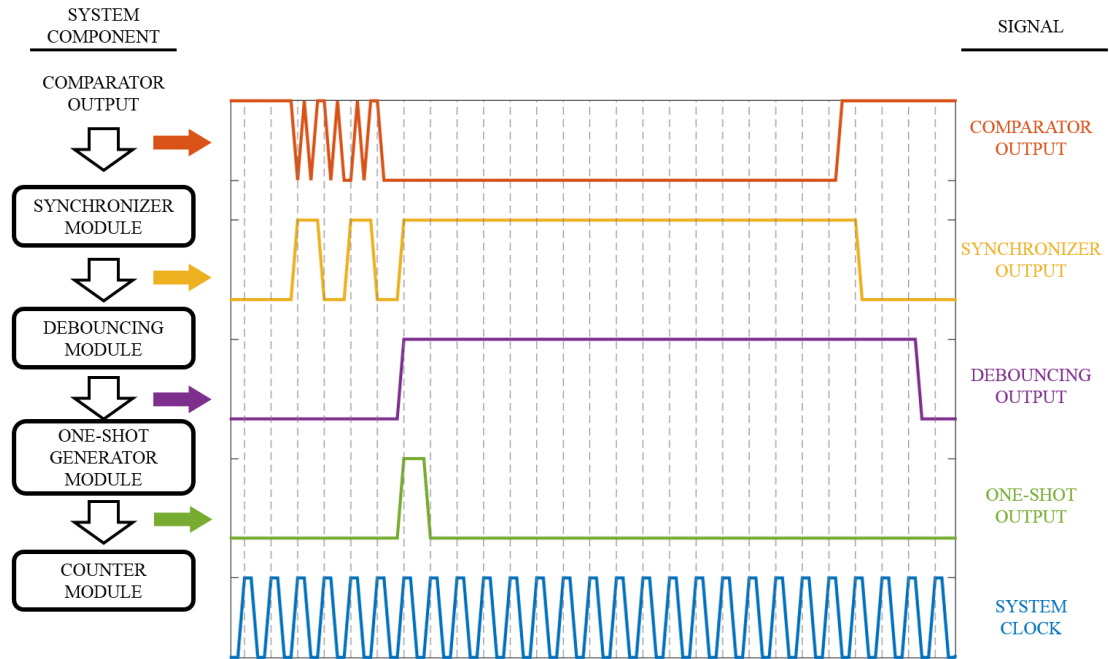
Figure 3.26: Illustration of the FPGA modules and their output signals.

separate sub-modules for each input signal, which are both triggered by the binary pulses from the debouncing module. A "one-shot" module generates single clock-cycle binary pulses and a "LED" module generates a 0.8 ms binary pulse that is routed to the LED of the detector panel that triggered it. The final module in the counting chain is the counting module, which tallies the number of one-shot binary pulses from the trigger module for each channel.

The counting module also records the count rate of each panel, controlled by a continuously-running state machine shown in Figure 3.27. The state machine starts in the "start" state, and enables a register capturing the real time (reg1_en) at that clock cycle and begins a timer (tm_en). The state machine then automatically
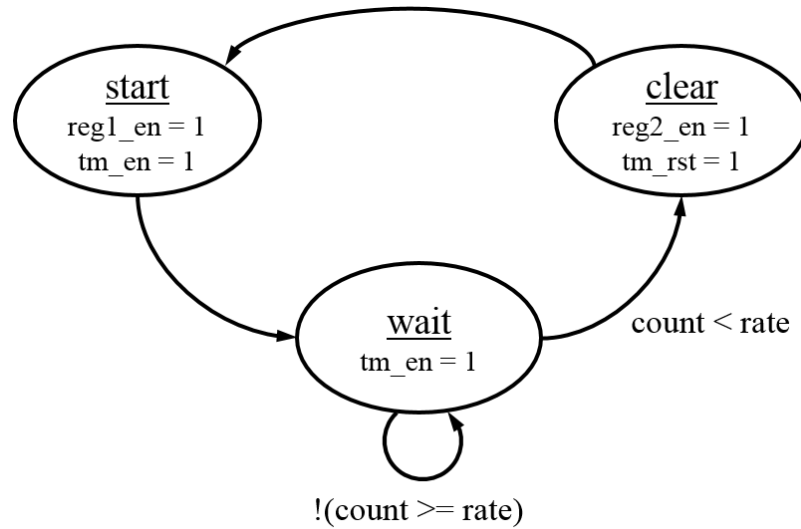
Figure 3.27: Illustration of the main state machine controlling the firmware modules in the FPGA.

moves to the "wait" state, where the timer value (count) is compared to a count rate value chosen by the user (rate), in terms of seconds. Once the timer has reached this value, the state machine moves on to the "clear" state, where a second register captures value in the first register subtracted from the current real time (reg2_en) and the timer is reset (tm_rst). The state machine then moves back to the "start" state, to begin the count rate capture process over again.

The FPGA and PC communicate via host interface firmware in the FPGA and an application programming interface (API) on the PC, both provided by the FPGA integration board manufacturer [60]. The host interface can be depicted as shown in Figure 3.28. Input commands and data are sent using MATLAB [61], through the USB microcontroller, to the host interface, which reads and routes the input signals to certain endpoints, based on the type of signal and a unique
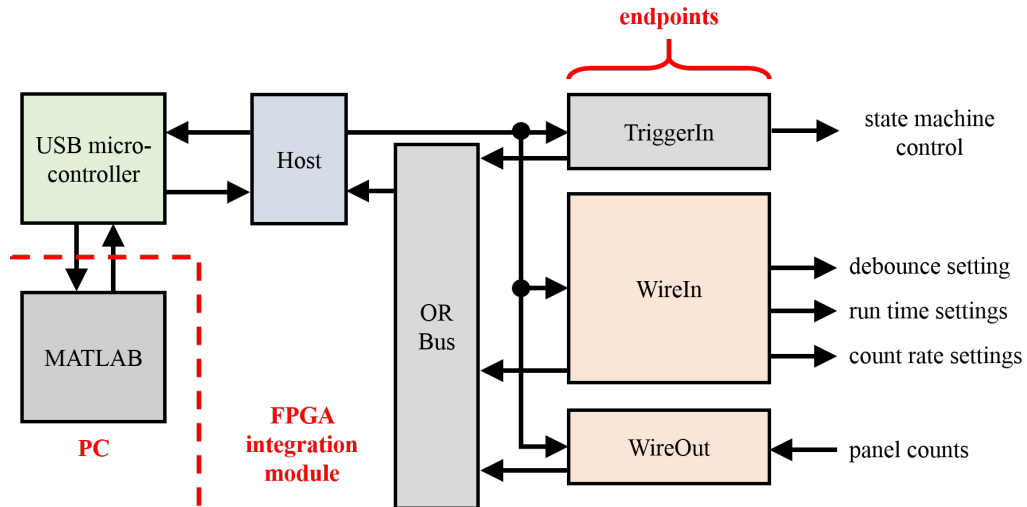
Figure 3.28: Illustration of the communication architecture of the FPGA-MATLAB API.

address. The original input signals can then be read from these endpoints in the FPGA hardware code.

A custom graphical user interface (GUI) was implemented using MATLAB for sending control signals to the FPGA host interface, shown in Figure 3.29. The first section (A) of the GUI allows the user to type four input settings: the name of the file that will be saved with the measurement information, the amount of real time measured by the FPGA in seconds to measure for, the interval over which the count rate is measured in seconds, and the number of debounce cycles.

The next section (B) allows the user to send control signals to the FPGA. The "PROG button establishes a connection between the FPGA and MATLAB and programs the FPGA with the appropriate firmware. The "DEPROG button discontinues the FPGA connection, allowing the firmware to be changed and the
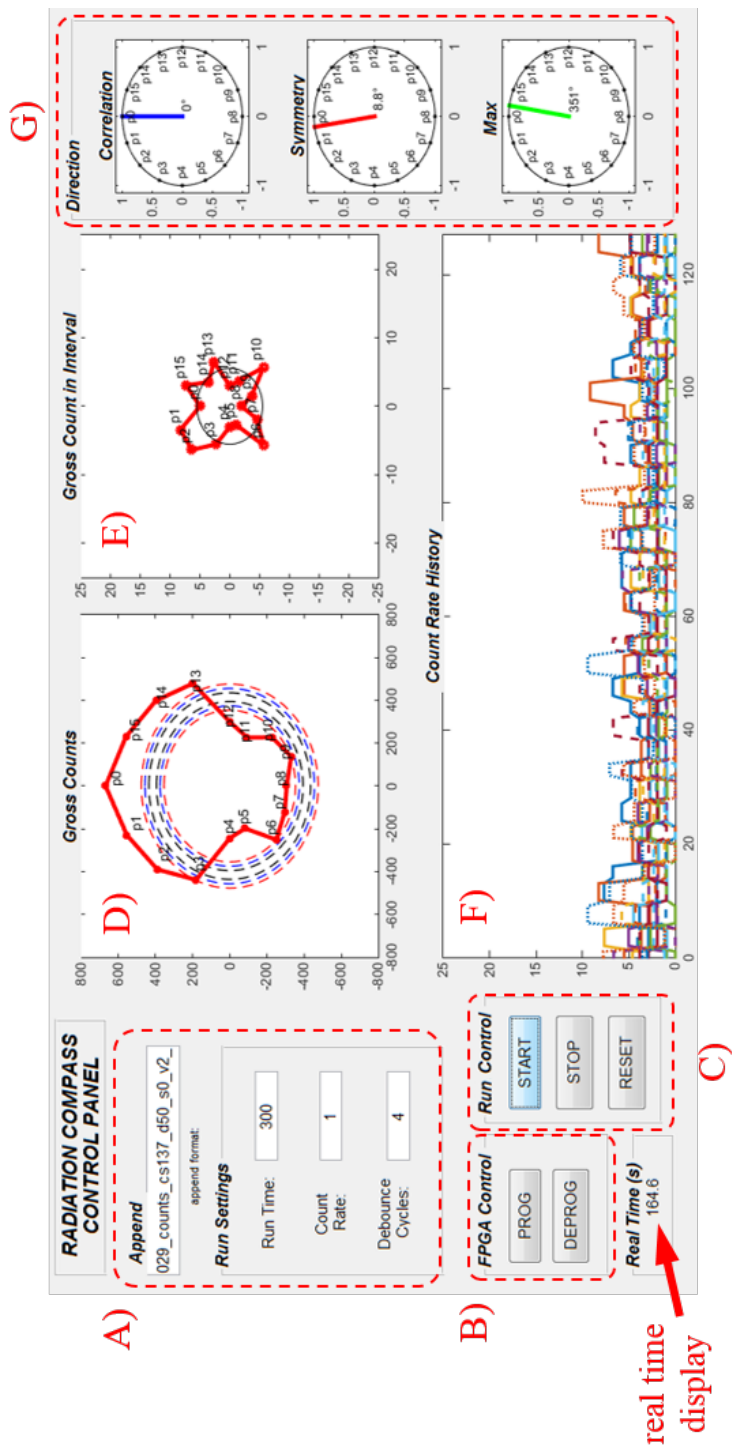
Figure 3.29: Screen capture of the MATLAB graphical user interface showing several distinct sections and plots used during operation.

FPGA reprogrammed. Another section (C) allows the user to control when measurements are started. The "START" button enables the sixteen counters that tally the comparator output pulses. The "STOP" button disables and resets the counters, and resets the real timer. The "RESET" button resets the counters and real timer. The next section (D) shows the gross count recorded in the current measurement. The fifth section (E) shows the number of counts recorded in a certain time window, determined by the count rate measured by the system. A further section (F) shows the measured count rate for the most recent 128 USB data transfers. The final section (G) shows estimates of the source direction given by each of the three direction estimation methods discussed in the next section. The MATLAB script also saves several sets of values for each measurement, including the measurement settings like real time, the number of counts in each panel, and the count rate for each panel.

3.2   Direction Estimation

Three methods were implemented for estimating the direction of the radiological source relative to the Radiation Compass, and compared for accuracy: a symmetry method, Matched Filtering, and Maximum Likelihood.

3.2.1   Symmetry Method

The Symmetry Method is an intuitive method that works by finding a vector of symmetry based on the count rate observed in each detector panel and each detector panel's position. If a radiation point source is not located at the Radiation Compass center point, then its direction relative to the Radiation Compass center point can be drawn as a source vector. The source vector is drawn from the center point of the Radiation Compass to the circle drawn through the centers of the BGO elements on each detector panel. Figure 3.30 provides a visualization of the Radiation Compass center point, circle of BGO center points, and an example of a source vector.

Because of the circular arrangement of detector panels and the fact that the detector panels are all located at the same vertical position, a point source placed at the Radiation Compass center point should produce an equal count rate in each detector panel. Statistical fluctuation is ignored here in order to simplify the explanation of this method. If the point source is not placed at the center of the detector panel circle, then the efficiencies of the panels closer to the source increase, and the efficiency of those panels further from the source decrease. The increases and decreases of efficiency for each detector panel are proportional to the distance of the point source from the Radiation Compass center point. For example, let the source move on a line between the Radiation Compass center point and the center point of panel 0. Let this line be the "X-axis" of a Cartesian coordinate system, and a line perpendicular to it through the Radiation Compass

center point be labeled the "Y-axis", as illustrated in Figure 3.31. As the point source moves toward the detector panel along the X-axis, the efficiencies of the neighboring panels, 1 and 15, will increase by the same amount, as will each pair of panels on opposite sides of the line the source moves on. Because the efficiency of each panel is proportional to the number of counts that will be observed, the number of counts observed in each panel follows the same increase or decrease as that panel's efficiency. Thus, when a source is moved on the line between the panel 0 center point and the Radiation Compass center point, the number of counts in the neighboring panels, 1 and 15, and each pair of symmetric panels will increase or
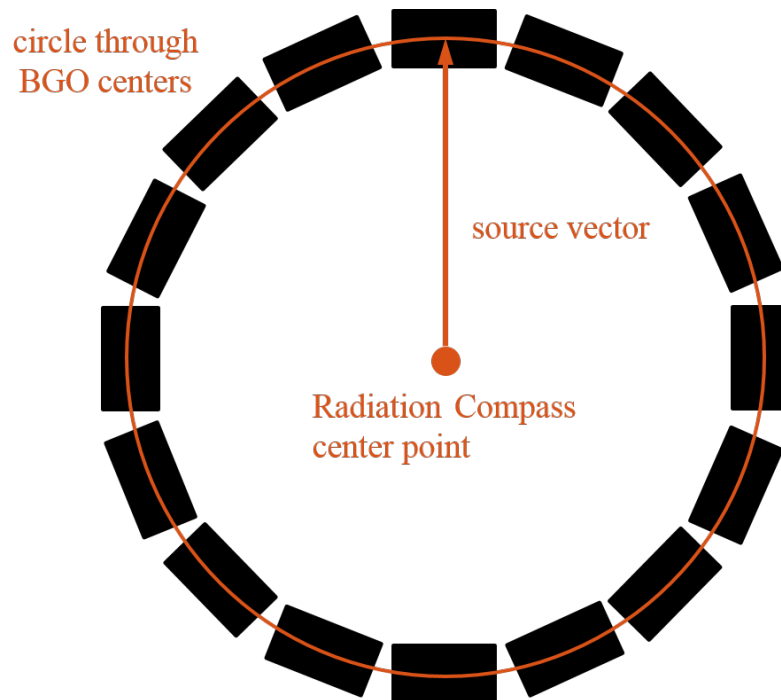
Figure 3.30: Illustration of the Radiation Compass detector panels and their relation to the Radiation Compass center point, the circle through the detector panel center points, and an example source vector.
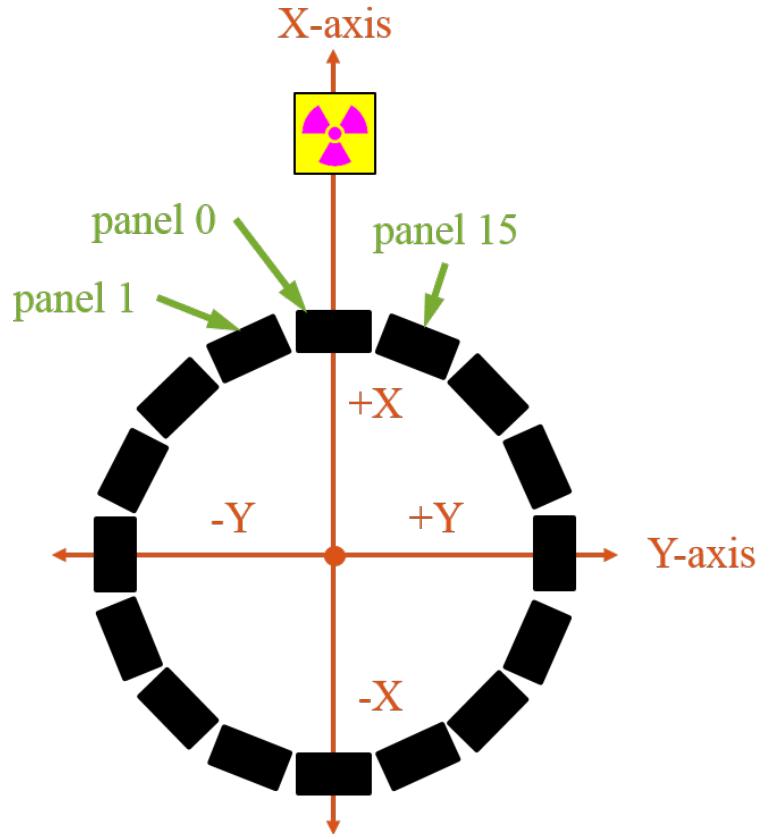
Figure 3.31: Illustration of the Radiation Compass detector panels and the chosen Cartesian X-Y axes orientation, source direction, and panel numbers.

decrease by the same amount. Thus, the number of counts from detector panels on the positive side of the X-axis will equal the number of counts from detector panels on the negative side of the X-axis. However, the number of counts from detector panels on the positive side of the Y-axis will greater than the number of counts from detector panels on the negative side of the Y-axis, introducing asymmetry to the detector response pattern, as seen in Figure 3.6.

The asymmetry in the detector response from a non-centered point source can

be used quantitatively to estimate the direction in which direction a point source lies relative to the Radiation Compass center point. First, the Cartesian two-dimensional coordinate axis with the origin at the Radiation Compass center point in the horizontal plane, as illustrated in Figure 3.31, with is chosen, with the X- and Y-axes oriented in an arbitrary manner, though aligning the X- and Y-axes through the center points of detector panels simplifies the concept. The source vector origin is always at the XY-axes origin. The source vector end point is then calculated using Equations 3.2 and 3.3:

$$W_X = \sum_{i=0}^{15} (d_i \cos(\phi_i)), \tag{3.2}$$

$$W_Y = \sum_{i=0}^{15} (d_i \sin(\phi_i)), \tag{3.3}$$

where W_X and W_Y correspond to the X-axis and Y-axis weights, respectively, d_i is the detector panel weight of panel i, and ϕ_i is the angle between the positive X-axis and the line between the Radiation Compass center point and the center point of panel i, as shown in Figure 3.32. The angle of the source relative to the Radiation Compass center point, with 0° and the direction of increasing angle shown in Figure 3.6, is calculated using Equation 3.4:

$$\theta_s = \tan^{-1} \left(\frac{X}{Y} \right), \tag{3.4}$$

where θ_s is the source angle relative to the defined detector orientation, also depicted in Figure 3.32. The same definition of source angle described here is used
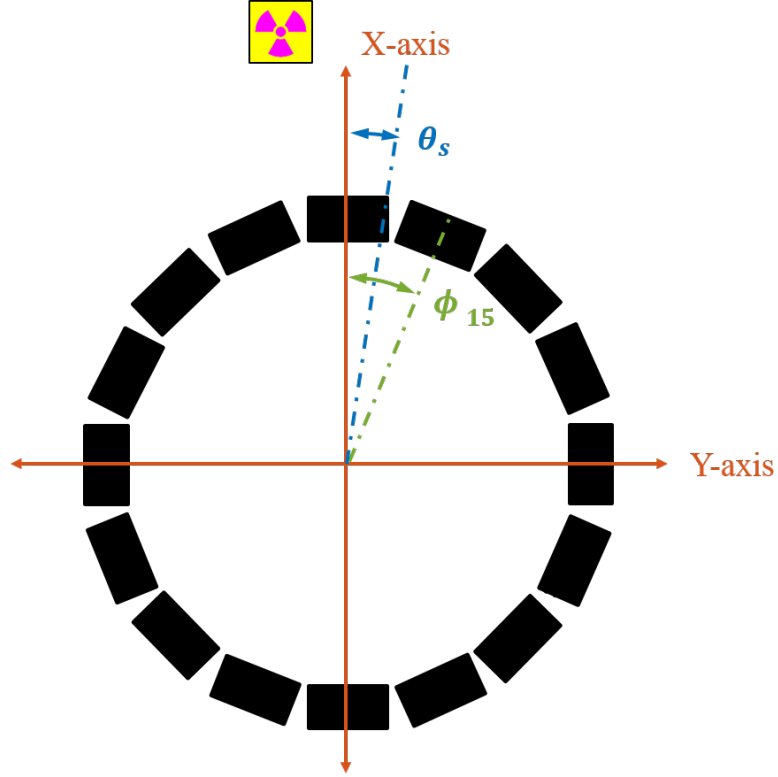
Figure 3.32: Illustration of the Radiation Compass detector panels and the chosen Cartesian X-Y axes orientation in relation to the source angle, θ_s, and the reference angle of panel 15, ϕ_1

throughout this work.

3.2.2 Maximum Likelihood

Maximum Likelihood is a method popular for many applications that require estimation of parameters in noisy environments [62]. Maximum Likelihood finds the probability that a given parameter model corresponds to a real measurement. The basic formulation of Maximum Likelihood is:

$$\hat{\psi} = argmax_{\psi \in \Psi} \mathcal{L}(\psi), \tag{3.5}$$

where $\mathcal{L}(\psi) = f(\bar{x}|\psi)$ is the likelihood that the measurement $\bar{x}$ corresponds to parameter ψ, and Ψ is the parametric model. For radiation detection, the Maximum Likelihood method first involves formulating the probability function of radiation interaction in a radiation detector. The probability function can be found based on the statistical models in Section 2.2: as long as the number of counts in the detector is greater than 20, the Gaussian distribution (Equation 2.7) can be used as the basis, where n is the number of radiation quanta emitted from the radiation source [63]. However, it must be modified to represent the number of radiation quanta detected. Since the Radiation Compass uses the ratio described in Equation 3.1, the number of quanta emitted n is modified to the number of quanta detected in each panel divided by the number of quanta detected in all panels to get the detector panel weights:

$$w_i(\theta_s) = \frac{\eta_i(\theta_s)}{\sum_i \eta_i(\theta_s)} \lambda \Delta t, \tag{3.6}$$

where $w_i(\theta_s)$ is the expected detector panel weight of detector panel i at source angle θ_s, $\eta_i(\theta_s)$ is the efficiency of detector panel i at source angle θ_s , λ is the decay constant, which is also the probability of a given radiological source emitting a radiation quantum per unit time, and Δt is the detector measurement time. The distribution function for a given panel detecting a quantum of radiation is thus:

$$p_i(w_i(\theta_s)|d_i) = \frac{1}{\sqrt{2\pi w_i}} e^{-\frac{1}{2}\frac{(d_i - w_i(\theta_s))^2}{w_i(\theta_s)}}, \tag{3.7}$$

where $p_i(w_i(\theta_s)|d_i)$ is the probability that the detector panel weight d_i observed in panel i corresponds to the expected detector panel weight $w_i(\theta_s)$. The likelihood that the observed detector response D, the set of observed detector panel weights $d_i, i = 0, ..., 15$, corresponds to expected detector response $W(\theta_s)$ for a source angle θ_s, the set of detector panel weights $w_i(\theta), i = 0, ..., 15$, is thus:

$$\mathcal{L}\theta = \prod_{i=0}^{15} p_i(w_i(\theta)|d_i). \tag{3.8}$$

Relating back to 3.9, the estimated source angle is:

$$\hat{\theta} = argmax_{\theta \in \Theta} \mathcal{L}(\theta). \tag{3.9}$$

The parametric model Θ describes all possible source angles θ. However, since the detector response is dependent on the energy of the gamma ray(s) being detected as well as the Radiation Compass altitude relative to the radiological source, the complete model should also include responses that vary for each of these parameters. The number of different source angles, gamma-ray energies, and Radiation Compass altitudes modeled determines the accuracy and resolution of the Radiation Compass direction estimation. The complete model is not used in this work but instead a subset of the complete model focused on the detector response to ^{137}Cs.

3.2.3   Matched Filtering

Matched Filtering is a technique first published in 1963 as the "North filter" after D. O. North, who first introduced it [64]. Matched Filtering works by applying a filter with the expected signal to an input signal and observing when the filter output rises above a certain threshold. Let the measured input signal be $x[n]$ and the filter be $h[n]$. The filter and signal are then convolved as in Equation 3.10 [65]:

$$y[n] = \sum_{k=-\infty}^{\infty} x[k]h[n-k] \tag{3.10}$$

where $y[n]$ is the output of the filter. For the Radiation Compass, the measured signal is of finite length M,

$$x[n] = \begin{cases} W[n] + \epsilon[n], & n = n_s \\ 0, & n = 0, ..., n_s - 1, n_s + 1, ..., M - 1 \,, \\ 0, & \text{otherwise} \end{cases} \tag{3.11}$$

where $\epsilon[n]$ is an independent Gaussian noise variable, and the filter is also of finite length M,

$$h[n] = \begin{cases} W[-n], & n = n_0, ..., n_{M-1} \\ 0, & \text{otherwise} \end{cases} \,. \tag{3.12}$$

The filter $h[n]$ is thus the time-inverted expected detector response for a given set of indexes n corresponding to a set of possible source angles $\theta[n]$, excluding the

noise term $\epsilon[n]$. The term n_s is the index number of the expected detector response $W[n_s]$ that corresponds to the true source angle θ_s. The signal $x[n]$ in 3.11 is the measured detector response D, which is matched to the expected detector response $D = W[n_s]$ for the source angle $\theta[n_s] = \theta_s$.

Substituting the signal 3.11 and filter 3.12 into 3.10, the output $y[n]$ becomes

$$y[n] = \sum_{\theta=0}^{M-1} ((W[k] + \epsilon[k]) \cdot (W[-n + k])) \tag{3.13}$$

Since only one measurement is used, $x[n]$, and therefore $y[n]$, are only non-zero at $k = n_s$, and $y[n]$ becomes

$$y[n] = W[n_s] \cdot W[-n + n_s] + \epsilon[n_s] \cdot W[-n + n_s]. \tag{3.14}$$

The source angle θ_s is then estimated by

$$\hat{n} = argmax_{n \in (M-1)}(y[n]). \tag{3.15}$$

The expression 3.14 is at its maximum when $n = 0$ because all detector responses $W[n]$ are normalized to the total count rate among all panels, so the term $W[n_s]\dot{W}[n_s]$ will be larger than for any other value of n.

3.3 Detector Simulation

3.3.1 MCNP

The Radiation Compass detector responses were simulated using the Monte-Carlo N-Particle transport code (MCNP) [66]. The Radiation Compass was modeled as a circular, evenly-spaced arrangement of sixteen 25 x 15 x 8 mm^3 right parallelepipeds (RPP) with the center point of each RPP 63.19 mm from the center point of all RPPs, as constructed in the real Radiation Compass. The RPPs were then filled with BGO material specified by atomic number. A 662 keV photon point source was used in all simulations to simulate the gamma ray from a ^{137} source. Several sets of simulations were undertaken, varying the source angle, view angle, and distance from the Radiation Compass center point. The F8 tally card was used to obtain the efficiency of each detector panel, with a 20 keV cutoff energy. These simulations had two purposes: one, to provide the expected source and view angle-dependent absolute efficiency of each panel i, $\eta_i(\theta_s)$, and second, to provide a means of simulating the direction-finding methods explained above. The sets of MCNP simulations performed are listed in Table 3.3.

Table 3.3: Table of MCNP simulation parameters.

| Set no. | Parameters | | | |
	Altitude	Distance	View Angle, α	Purpose
1	0 cm	15 cm	0°	detector panel efficiency
2	0 cm	100 cm	0°	direction sensitivity
3	50 cm	0 - 100 cm	0°, 45°, 90°	view angle optimization
4	50 cm	50 cm	0°, 30°, 45°, 60°, 90°	view angle optimization
5	50 cm	100 cm	0°, 30°, 45°, 60°, 90°	view angle optimization

Set 1 was used to study the efficiency of each detector panel, and is illustrated in Figure 3.33. The detector was configured such that the source angle was zero,
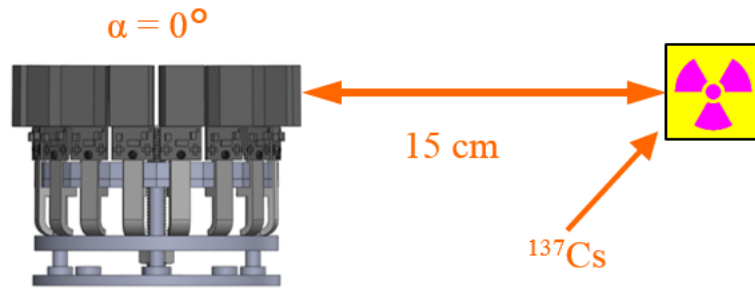
Figure 3.33: Illustration of the Set 1 setup.

$\theta_s = 0$, and the source was directly in line with the center of the 25 x 15 mm^2 face of the detector panel. The ^{137}Cs point source was positioned at the vertical center of the BGO panels 15 cm from the Radiation Compass center point.

Set 2 was used to study the direction sensitivity of the Radiation Compass, and is illustrated in Figure 3.34. The detector was rotated from 0°- 22.5° every
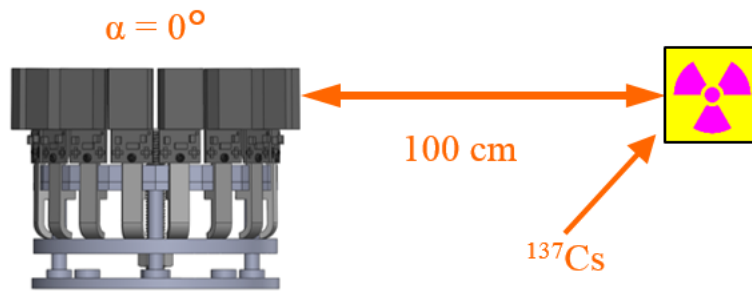
Figure 3.34: Illustration of the Set 2 setup.

4.5° with the detector panels at a view angle of 0°. The ^{137}Cs point source was

positioned at the vertical center of the BGO panels 100 cm from the Radiation Compass center point.

Set 3 was used to study the view angle optimization of the Radiation Compass with distance, and is illustrated in Figure 3.35. The detector panels were set at a
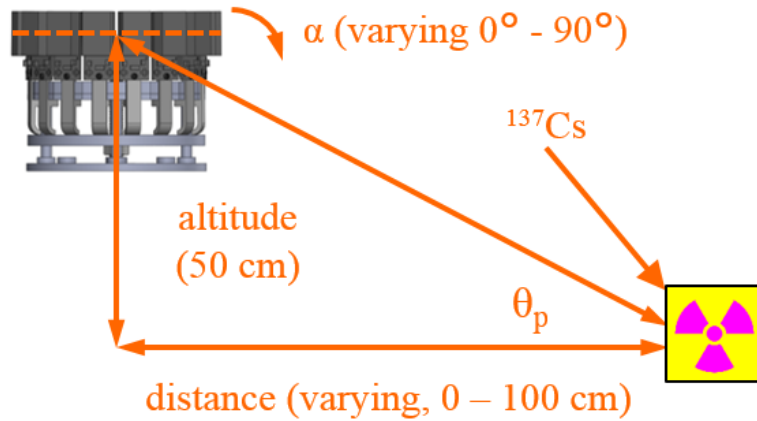
Figure 3.35: Illustration of the Set 3 setup.

view angle of 0°and and a source angle of 0°. The ^{137}Cs point source was positioned 50 cm below the Radiation Center, and the distance from the Radiation Center varied between 0 cm and 100 cm every 10 cm.

Set 4 was used study the view angle sensitivity of the Radiation Compass, and is illustrated in Figure 3.36. The detector panels were rotated to 0°, 30°, 45°, 60°, 90°. The ^{137}Cs point source was positioned 50 cm below and 50 cm from the Radiation Compass center point.

Set 5 was used study the view angle sensitivity of the Radiation Compass, and is illustrated in Figure 3.37. The detector panels were rotated to 0°, 30°, 45°, 60°, 90°. The ^{137}Cs point source was positioned 50 cm below and 100 cm from the
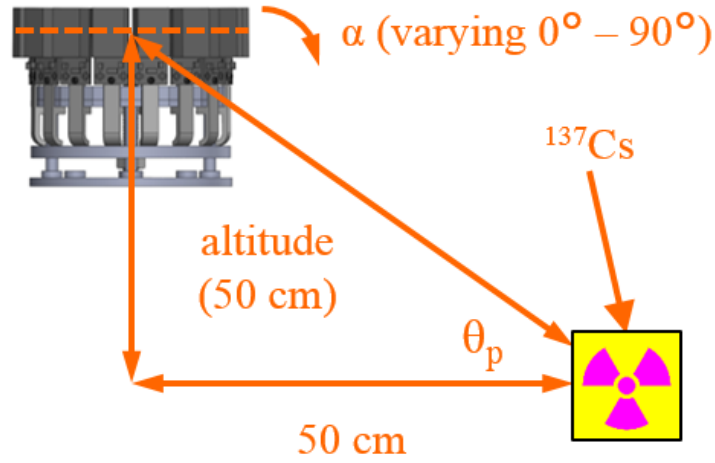
Figure 3.36: Illustration of the Set 4 setup.

Radiation Compass center point.

The expected angle-dependent absolute efficiencies of the panels for each simulation set were compiled into a library of expected detector responses for 360° by shifting the detector responses by one panel every 22.5°. For example, the efficiency for detector panel i at source angle 0° was also used as the efficiency for detector panel $i + 1$ at source angle 22.5°, detector panel $i + 2$ at 45°, and so on. The library for simulation sets that studied direction sensitivity and view angle sensitivity thus each contained 80 detector responses for source angles every 4.5° starting at 0°.
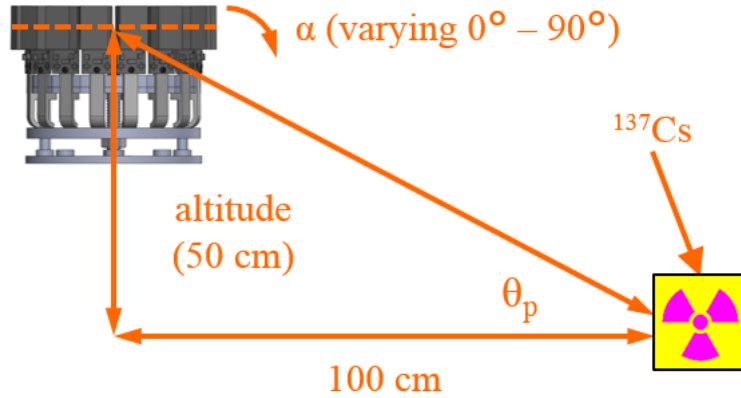
Figure 3.37: Illustration of the Set 5 setup.

3.3.2   Detector Response Simulation

The sensitivity of the Radiation Compass to the source angle, θ_s, distance from the detector, and view angle were simulated using the MCNP results as well as background measurements from the Radiation Compass. Detector measurements were simulated in MATLAB by adding a simulated ^{137}Cs source response to a simulated, randomly-generated background response. A simulated source response was generated for several different source activities in each case, from 1 µCi to 10 µCi in 1 µCi increments. The activity in Bequerels was multiplied by the simulated counting time, 60s, and the gamma-ray yield, 85.10% for the ^{137}Cs 661.657 keV gamma ray [67], to obtain the simulated number of detector emissions. The number of emissions was then multiplied by the absolute efficiency for each panel simulated using MCNP to obtain the number of simulated counts for each detector panel. The background for each panel was simulated by first taking a background

measurement from the Radiation Compass, and averaging the number of counts observed in each detector. The average background count rate based on a 1-hour measurement was 0.82 counts per second per panel, for a total Radiation Compass background rate of 13.12 counts per second. A number of background counts was then randomly generated for each detector panel based on a Gaussian distribution with mean and variance equal to the average measured background counts. The simulated background for each panel was then added to the simulated source counts for the same panel to obtain the simulated detector measurement. The three direction-estimation methods were then applied to the simulated detector measurement and the source angle estimated by each method recorded. The procedure above, generating a random background, adding it to the simulated detector response, and applying the estimation methods, was repeated 10,000 times for each detector and source geometry. The simulation results were used to compare the effectiveness of each method by comparing each method's mean square error (MSE) [68], calculated using Equation 3.16:

$$MSE = \frac{1}{N} \sum_{i=1}^{N} (\hat{\theta}_i - \theta_s)^2, \tag{3.16}$$

where N is the number of measurements or simulations, $\hat{\theta}_i$ is the estimated angle, and θ_s is the true source angle. The MSE is useful for comparing different estimators since it is a measure of both an estimator's accuracy, called the bias, and the estimator's precision, called the variance: $MSE = Bias^2 + Variance$.

Chapter 4: Results and Discussion

4.1 Detector Panel Uniformity

An essential aspect of the Radiation Compass performance is the uniformity of the panels response to radiation exposure. All aspects of the system's fabrication and construction described herein were undertaken with this goal in mind, and the tests and characterizations described in this section undertaken to measure the uniformity of the system.

4.1.1 Analog Electronics Characterization

The first test of the front-end analog electronics was to measure the uniformity of the light collection efficiency. This was tested by measuring the average voltage amplitude of preamplifier pulses from a ^{137}Cs source, which correspond to the 662 keV gamma ray. The oscilloscope averaged the peak voltage from 32 AC-coupled pulses for each panel. The average voltage amplitude measured among all panels was 1.41 V, and the relative standard deviation of the voltage amplitude among all panels was 10.5%.

The comparator voltage threshold for each panel was set based on the noise level of each individual panel. Because the preamplifier outputs carry a DC voltage offset due to the SiPM dark current [51], the true voltage threshold for each pulse is

equal to the comparator threshold voltage input minus the DC offset voltage. The average true voltage threshold was 541 mV, and the relative standard deviation was 12.0%. The true threshold voltages were used to calculate an energy threshold for each panel, based on the peak voltage from ^{137}Cs. The average calculated energy threshold was 255 keV, and the relative standard deviation was 8.2%.

4.1.2 Detector Panel Efficiency

The detector panel absolute efficiency was measured using the parameters in Set 1 from Table 3.3, pictured in Figure 4.1 and described in Section 3.3. The efficiency
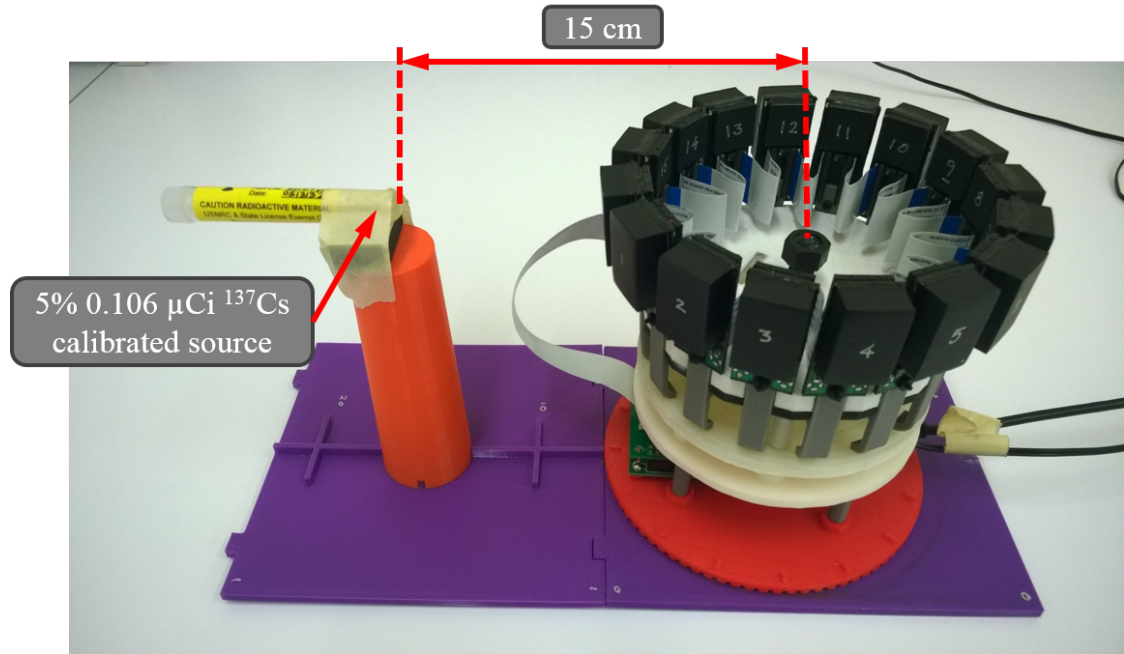
Figure 4.1: Photo of the efficiency counting setup for one panel.

counting measurement was performed for each panel in two steps. First, a 5 minute

background measurement was taken, and then the source was placed 15 cm from the Radiation Compass center point and a 5 minute measurement recorded. The source used was a 5% calibrated 0.106 μCi ^{137}Cs source. The detector system was rotated before each pair of measurements to align the panel being measured with the measurement position.

The ratios of the measured absolute efficiency to the MCNP-generated absolute efficiency for each panel are shown in Figure 4.2. The plotted ratio of measured to
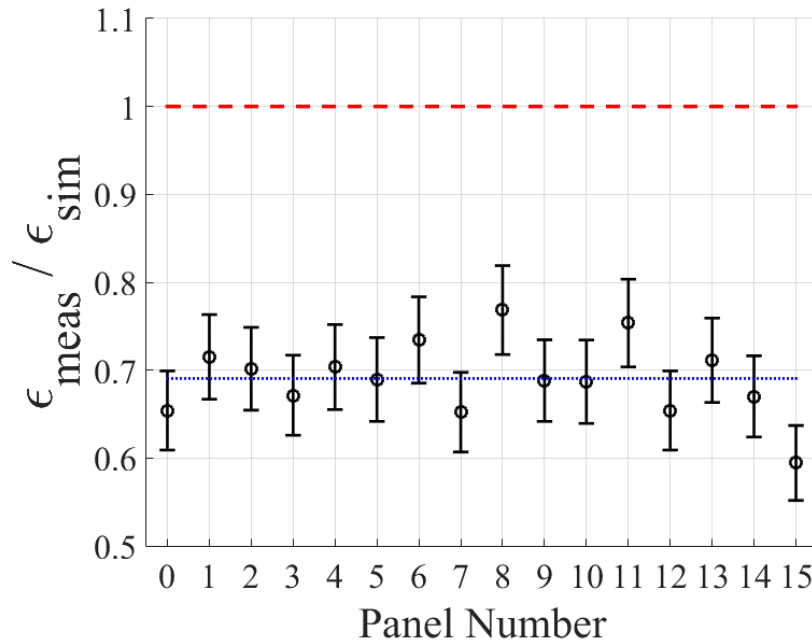
Figure 4.2: Ratio of measured efficiency to simulated efficiency obtained using MCNP. The dashed red line indicates perfect one-to-one agreement, and the blue line is the mean of the calculated ratios.

simulated efficiency averaged 0.7 because of the difference between the simulated panel energy threshold (20 keV) and the estimated real panel energy threshold for

the measurements (255 keV). The system efficiency was measured again using the calibrated ^{137}Cs source, positioned 100 cm from the center of the array in order to measure the minimum detection time for a 10 µCi source using the method first proposed by L. A. Currie [69]. First, the minimum number of counts from a source of radiation that will result in false positive and false negative rates no greater than 5% is calculated using Equation 4.1:

$$N_D = 4.653\sigma_{N_B} + 2.706, \tag{4.1}$$

where N_D is the minimum number of counts from the source needed to satisfy the maximum false-positive and false-negative rates of 5%, and σ_{N_B} is the square root of the number of background counts. Equation 4.1 is also known as the "Currie Equation" [8]. The number of source counts N_D is then used in Equation 4.2:

$$T_{min} = \frac{N_D}{A \cdot \epsilon \cdot Y}, \tag{4.2}$$

where T_{min} is the minimum amount of counting time to ensure that a source with activity A will produce the minimum number of counts N_D from the source needed to satisfy the maximum false-positive and false-negative rates of 5%, when the radioactive emission producing the counts has a yield of Y, and the detector has an absolute efficiency of ϵ. Equations 4.1 and 4.2 were used, along with source and background measurements, to determine that the amount of time needed to detect a 10 µCi ^{137}Cs source with 95% confidence 100 cm from the center of the Radiation Compass was less than 8 s at a total background count rate of 25.5

counts per second. It is important to note that this is a minimum detection threshold indicating that a radiation source greater than background is present, not a measure of direction sensitivity, which is discussed in Section 4.2.

4.1.3 Panel Counting Uniformity

Uniformity in panel radiation counting response is essential for the Radiation Compass since it relies on specific counting patterns to estimate a source direction. The uniformity was measured with respect to the count rate recorded in each panel. One example of a measurement recorded with a 10 µCi ^{137}Cs source at the Radiation Compass center point is shown in Figure 4.3. The count rate from each panel is shown in Figure 4.4, where the relative standard deviation of the count rates among all panels was 4.3%.

In order to increase the accuracy of the Radiation Compass, measurements using the setup depicted in Figure 4.3 were taken before and after measurement sets, and are described along with the measurement sets in Section 4.2 below. The mean of the detector panel count rates, $\bar{R}$, was divided by the count rate of each panel i, R_i, to get a correction factor for each panel $C_i = \bar{R}/R_i$. The correction factor for each panel was applied by multiplying the correction factor by the number of counts recorded by the panel. A demonstration of the effect of correction on the measurement shown in Figure 4.4. Two uniformity measurements were taken one after the other, and then the correction factors calculated using the first measurement were applied to the second measurement, improving the standard
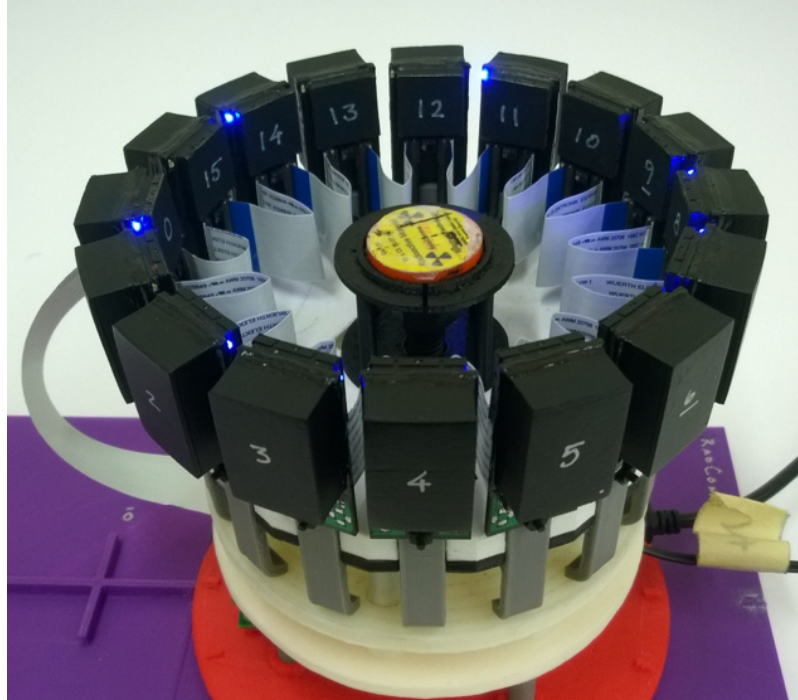
Figure 4.3: Photo of the setup used to take correction data, using the source centering apparatus.

deviation among panel count rates from 4.3% to 1.0% relative standard deviation.
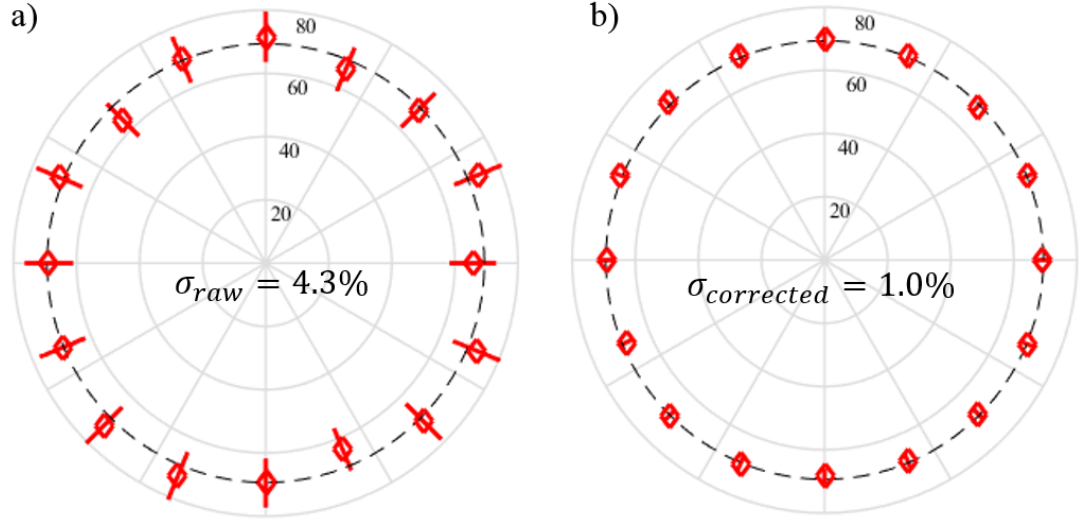
Figure 4.4: Plots demonstrating the effectiveness of the correction factors in improving radiation detector panel uniformity.

4.2 Direction Sensitivity

4.2.1 Simulation

The direction sensitivity of the Radiation Compass was first studied using the simulation results of Set 2 from Table 3.3, as described in Section 3.3. Five source angles were simulated: 0°, 4.5°, 9°, 13.5°, and 18°. The total Radiation Compass absolute efficiency is shown in Figure 4.5 for the same source angles investigated. Though there is some slight variation in the absolute efficiency at different source angles, the total absolute efficiency of the Radiation Compass is relatively constant across the five angles. The minimum total absolute efficiency variation is ideal since the Radiation Compass should not be more sensitive at any specific source angle
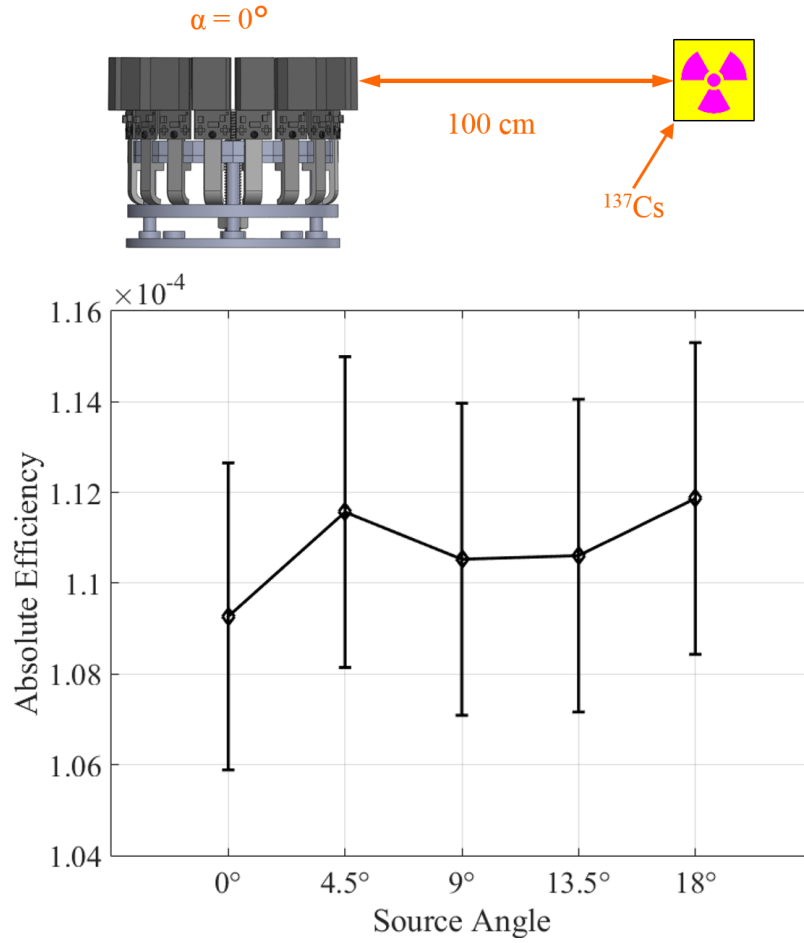
Figure 4.5: Plot of the absolute efficiency of the detector panels summed together, the total Radiation Compass absolute efficiency, simulated using MCNP.

since the initial angle of the device with respect to the source will not be known.

As described in Section 3.3.2, the source angle estimated by each method was recorded for all 10,000 simulations and the MSE calculated for each method. Plots of MSE versus source strength for each estimation method and angle are shown in Figure 4.6, and a plot of MSE versus source angle for each estimation method at

10 µCi is shown in Figure 4.7. An example of the convergence of the estimation methods for increasing source activities is shown in Figure 4.8.

Figure 4.6 shows that the Matched Filter and Maximum Likelihood methods vastly outperform the Symmetry method as the source activity increases. Though the Matched Filter method out-performs the Maximum Likelihood method at source angles 0°, 9°, and 13.5°, the Maximum Likelihood method outperforms the Matched Filter method at source angles of 4.5° and 18°.

Figure 4.7 shows that at 10 µCi, the Matched Filter method shows greater MSE at source angles 4.5° and 18° than the Maximum Likelihood method, but is the overall best method. The MSE of the Symmetry method changes relatively little, all within the same order of magnitude.
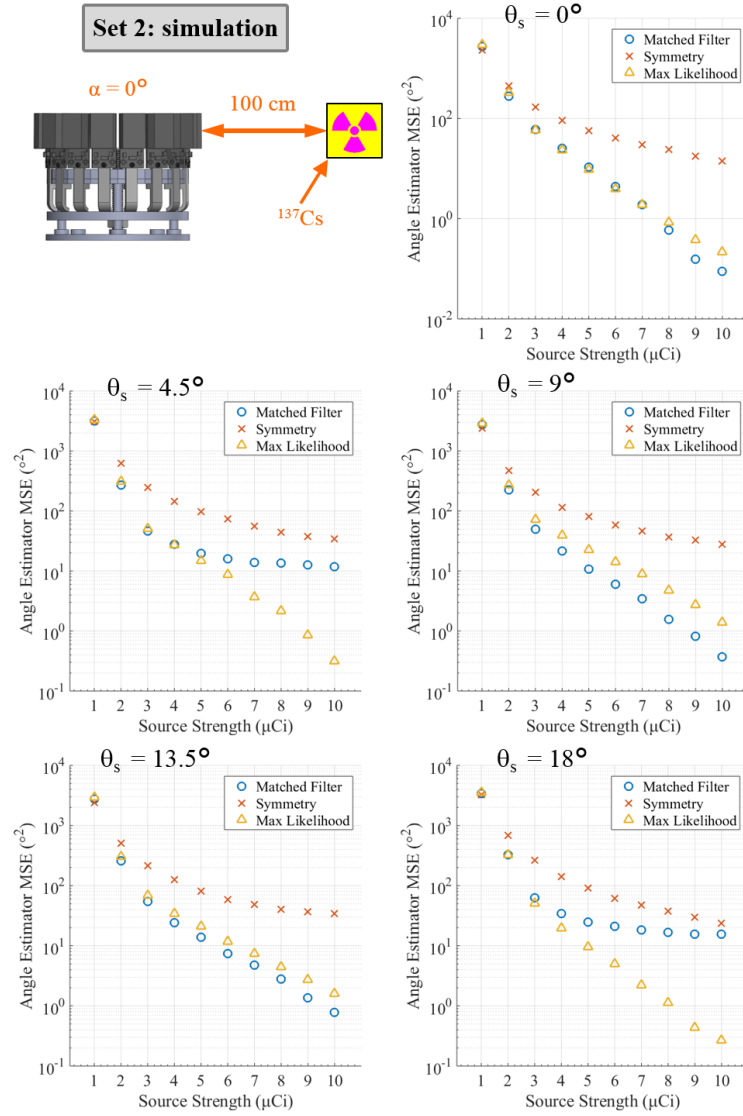
Figure 4.6: Simulated mean squared error of each of the three estimation methods over ten source activities, simulated at five different source angles.
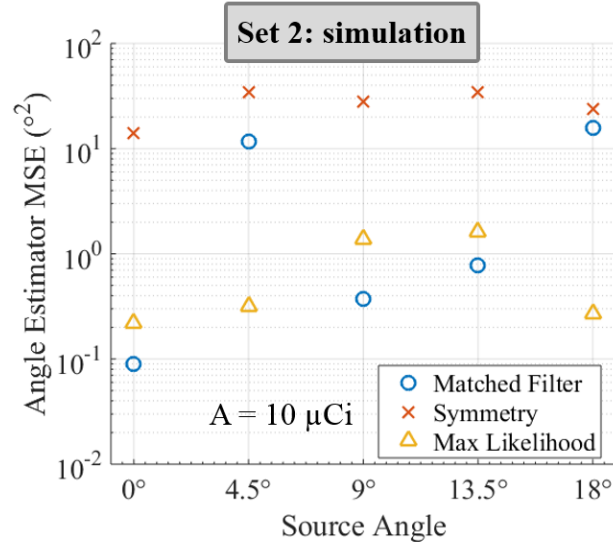
Figure 4.7: Simulated mean squared error of each of the three estimation methods over five different source angles, at 10 µCi.
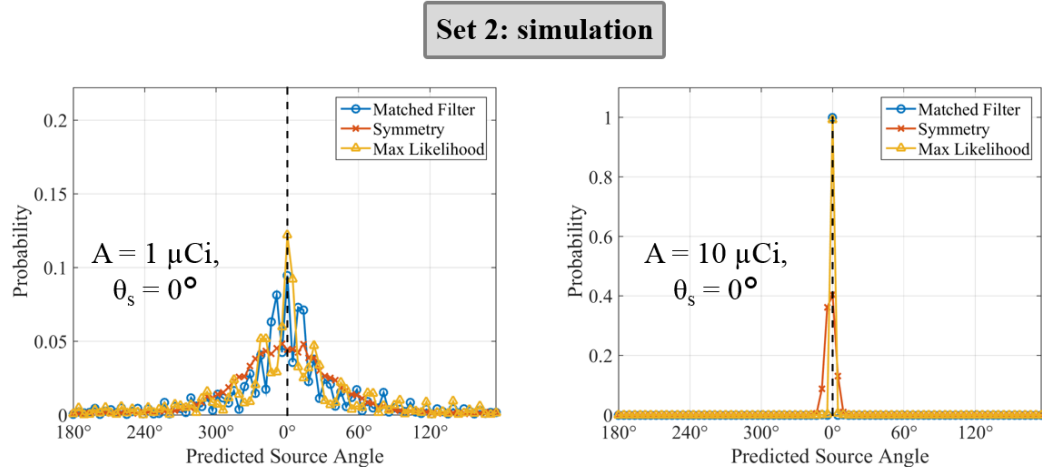
Figure 4.8: Histograms of the number of times each source angle was estimated by each of the three direction estimation methods, where the black dashed line indicates the true source angle. The number of times each angle was estimated is normalized by the total number of simulations run labeled as the probability.

4.2.2 Measurements

The accuracy of each of the direction estimation methods at zero altitude was studied using the parameters in Set 2 from Table 3.3, pictured in Figure 4.9. Five ^{137}Cs sources totaling 12.3 µCi were used, and twenty 60 s measurements
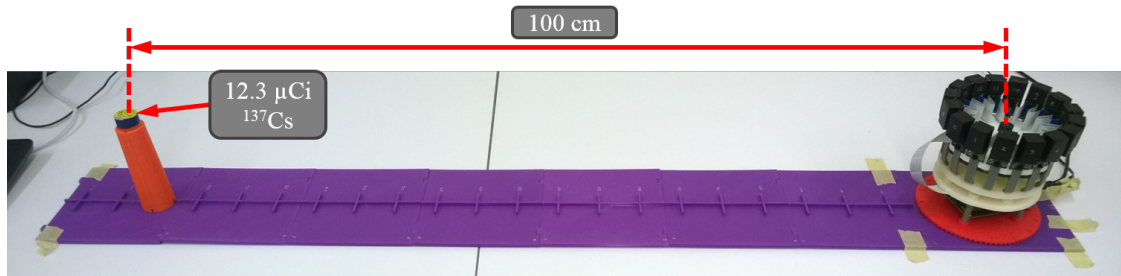
Figure 4.9: Photo of the setup used to take direction sensitivity data.

were taken at each of the source angles simulated above: 0°, 4.5°, 9°, 13.5°, and 18°. The total Radiation Compass count rate is shown in Figure 4.10, which does not completely follow the trend expected based on the total efficiency shown in Figure 4.5, but does only vary by 0.5 cps at most, indicating that the total count rate measured at each source angle is close to the count rates at other angles, as expected.

The direction estimation methods were then applied to each measurement and the MSE of each method recorded, shown in Figure 4.11. The MSE values for each of the three methods correspond to simulated MSE values for a source activity of approximately 2 µCi because the actual energy threshold for each of the detector panels, as discussed in Section 4.1.1, was 255 keV on average, and the MCNP simulations used an energy threshold of 20 keV. The MSE of each method were
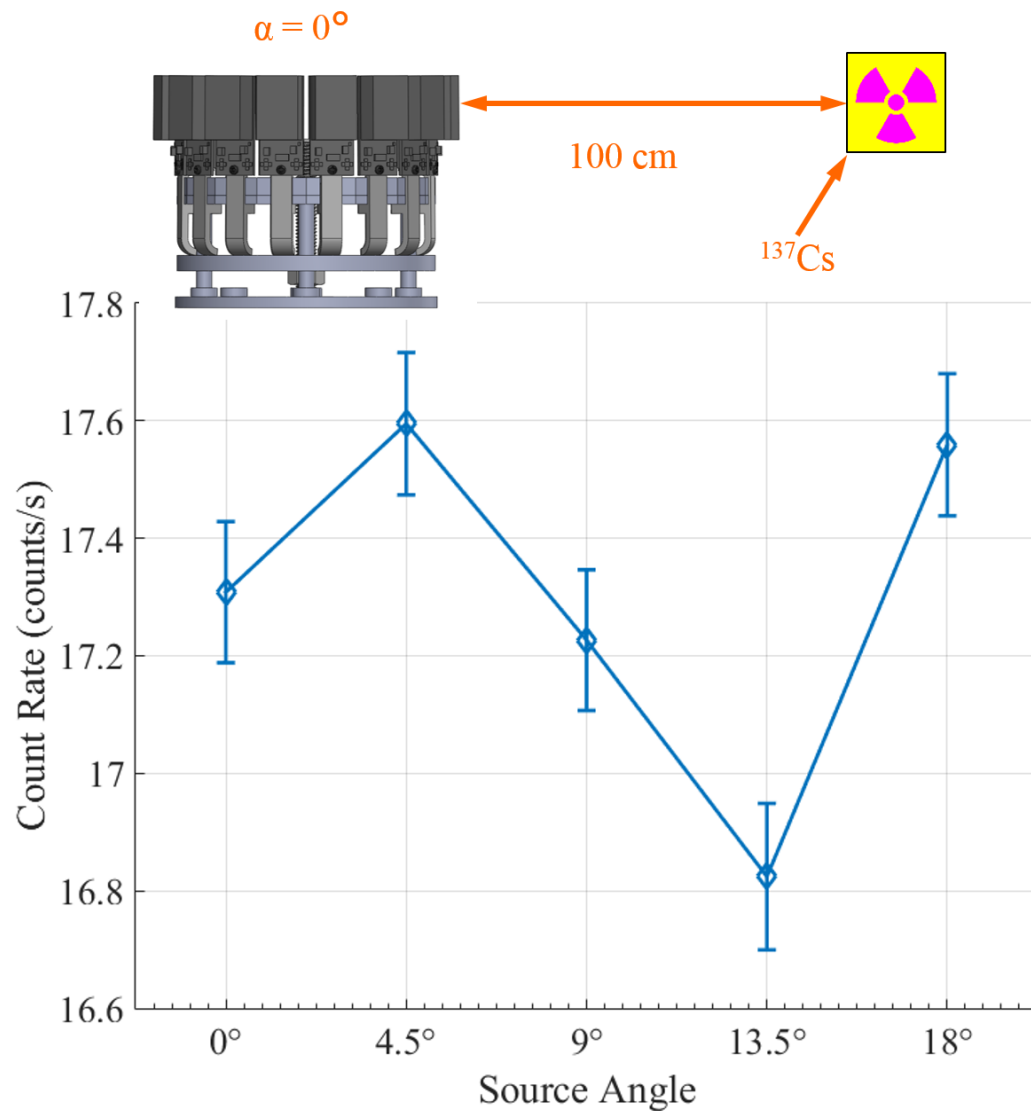
Figure 4.10: The measured total count rate of the Radiation Compass at the five source angles of interest.

summed over the five angles of interest to compare their overall performance. The Matched Filter method showed the lowest total MSE, indicating that it was the
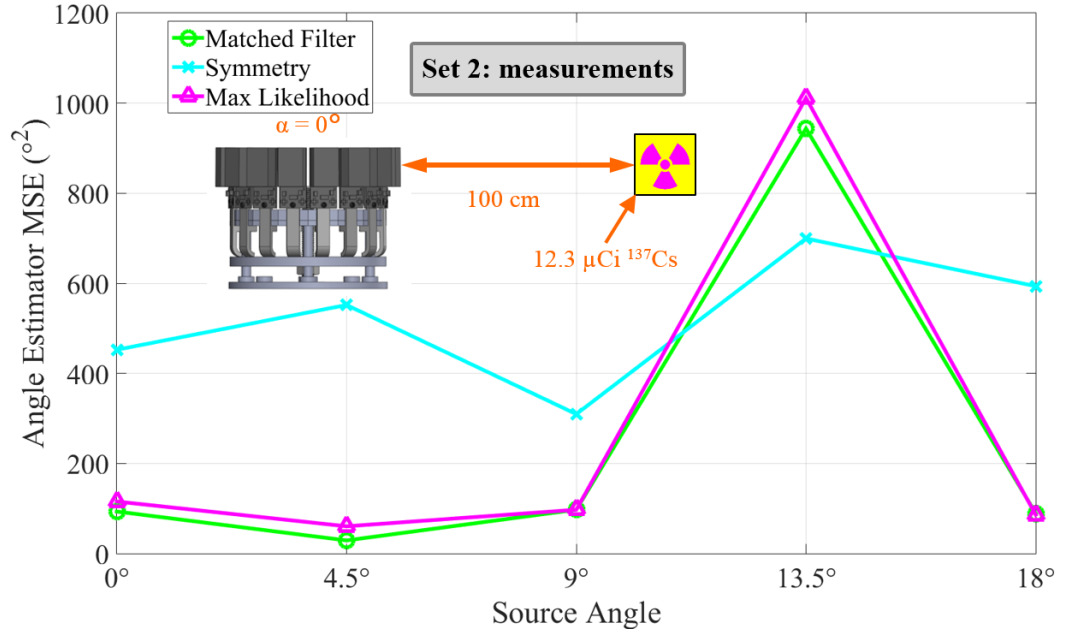
Figure 4.11: Measured mean squared error of each of the three direction estimation methods at each of the five source angles of interest.

best method used with the Radiation Compass, though the Maximum Likelihood method had similar MSE values.

The accuracy for each estimation method for each set of twenty measurements was quantified for the five source angles of interest using the absolute value of the bias, where the bias is:

$$Bias = \bar{\hat{\theta}} - \theta_s, \tag{4.3}$$

where $\bar{\hat{\theta}}$ is the mean estimated angle and θ_s is the true source angle. The precision for each estimation method for each set of twenty measurements was quantified

using the 95% confidence interval, calculated using the cumulative normal distribution function, where $\Phi(z) = P(Z \leq z) = 1 - \alpha/2 = 0.975$. The results of this analysis are listed in Tables 4.1 and 4.2. These results are also shown in Figure 4.12, where the black dashed line with the diamond at one end represents the true source angle, the triangle color-coded according to each estimation method shows the 95% angular confidence interval, and the darker colored, solid line indicates the mean estimated angle of the associated estimation method. The Maximum Likelihood method shows the best overall accuracy since it has the lowest bias values at three of the five source angles of interest, but the Matched Filter method shows the best overall precision since it has the lowest 95% confidence width at four of the five source angles of interest.

Table 4.1: Table of the absolute value of the bias of each estimation method for the measurements based on Set 2.

source	Estimator $|Bias|$		
angle, θ_s	Symmetry	Matched Filter	Max Likelihood
0°	10.8°	1.8°	0.9°
4.5°	5.7°	1.4°	0.7°
9°	6.1°	1.8°	0.5°
13.5°	6.0°	4.1°	7.0°
18°	11.8°	1.8°	3.8°

A comparison between the simulated and measured Radiation Compass response patterns for parameter Set 2 at each of the source angles of interest is shown in Figures 4.13 and 4.14, where the simulated responses, without any added background, are shown on top, the measured responses, with a background rate of 0.82 counts per second per panel, shown on the bottom, and dashed red
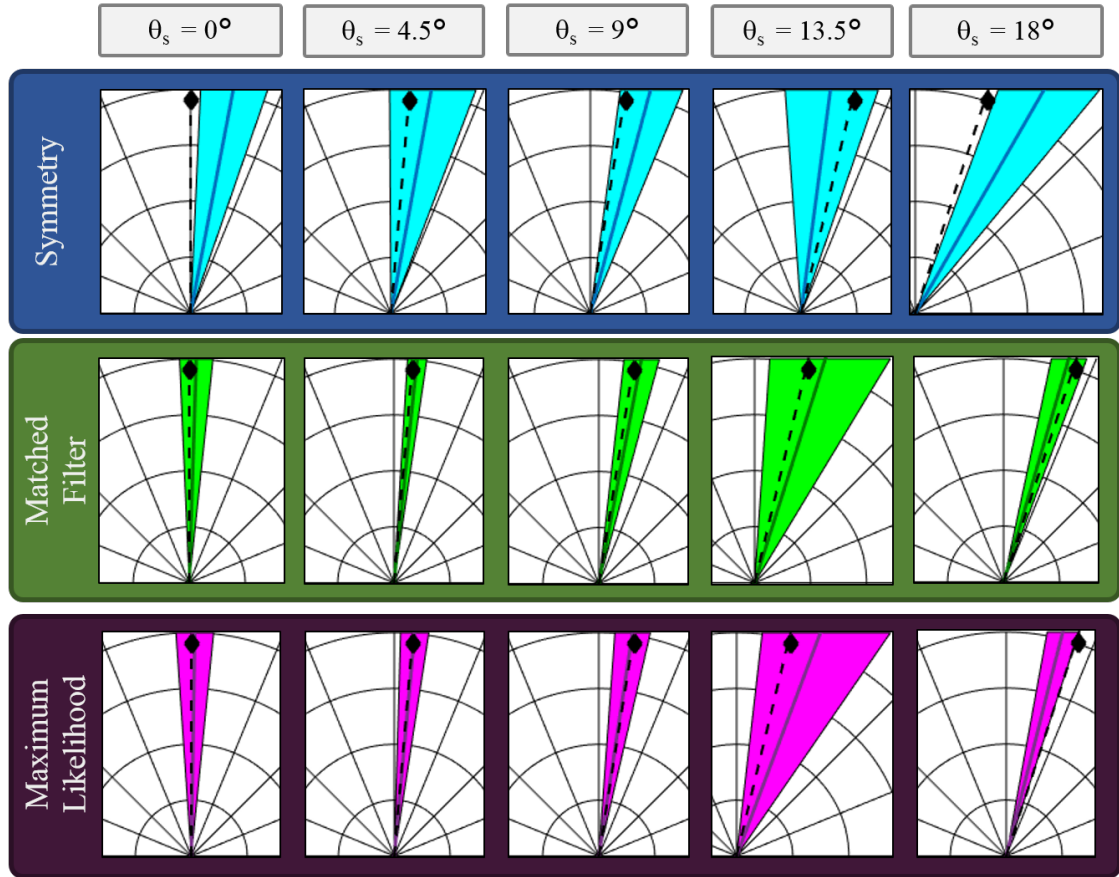
Figure 4.12: Radar plots showing the mean estimated angles and 95% confidence intervals for the measurements based on Set 2. The 95% confidence intervals are represented as triangles, each with a color corresponding to the estimation method labeled to the left. The mean estimated angle for each method at each angle is shown as a solid line in a darker shade of the confidence interval color. The true source angle is labeled as a black dashed line with a black diamond at one end.

lines show the true source angle. Figure 4.13 shows the detector response for one randomly-selected 60 s measurement from the set of twenty measurements. In each of these cases, the measured responses bear at best a passing resemblance to their simulated counterparts. Figure 4.14 shows the measured detector response

Table 4.2: Table of estimator method 95% confidence intervals for the measurements based on Set 2.

source	95% confidence interval		
angle, θ_s	Symmetry	Matched Filter	Max Likelihood
0°	[2.5°,19.0°]	[-2.5°,6.1°]	[-3.9°,5.7°]
4.5°	[-0.3°,20.8°]	[3.5°,8.4°]	[1.7°,8.8°]
9°	[7.6°,337.5°]	[6.4°,15.2°]	[4.1°,13.0°]
13.5°	[-4.1°,19.1°]	[3.9°,31.2°]	[6.5°,34.4°]
18°	[20.3°,39.4°]	[12.0°,20.4°]	[10.4°,18.0°]

pattern averaged over the twenty 60 s measurements. The averaged responses show better agreement with the simulated results, though they still appear less well-defined. The reason for the differences is likely because of the background present in the measured responses, as well as the fact that the energy threshold of the real detector was higher than that of the simulations.
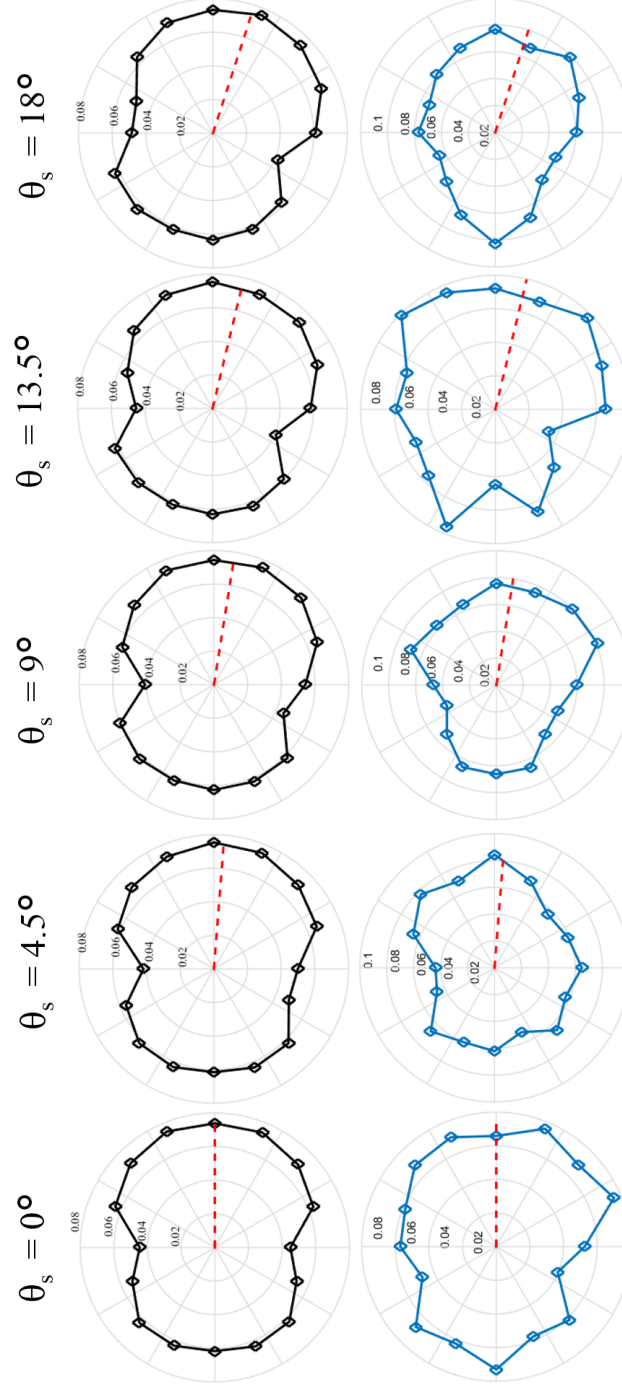
Figure 4.13: Comparison between simulated and measured detector response patterns for parameter Set 2 at each of the five source angles of interest. The simulated responses, without any added background, are shown in black across the top, and the measured responses, with a background rate of 0.82 counts per second per panel, are shown in blue across the bottom. The dashed red lines indicated the true source angles. The measured responses were taken from a single randomly-chosen 60 s measurement.
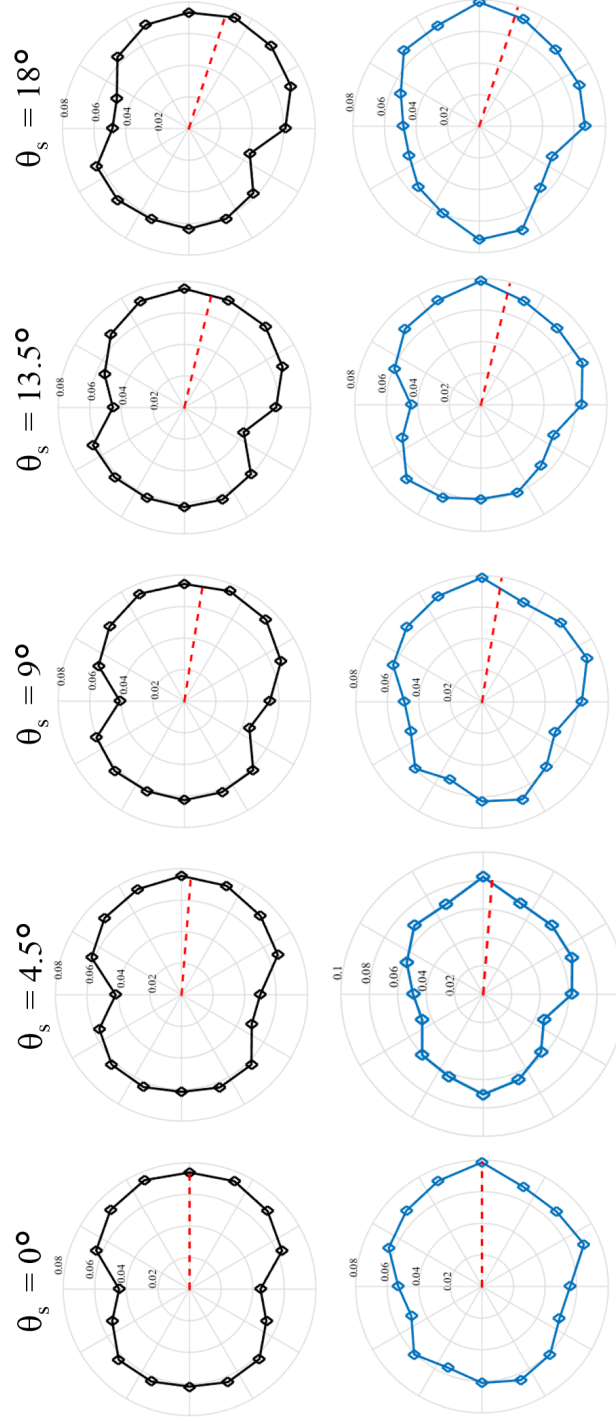
Figure 4.14: Comparison between simulated and measured detector response patterns for parameter Set 2 at each of the five source angles of interest. The simulated responses, without any added background, are shown in black across the top, and the measured responses, with a background rate of 0.82 counts per second per panel, are shown in blue across the bottom. The dashed red lines indicated the true source angles. The measured responses are the average values across all twenty 60 s measurements.

4.3   View Angle Sensitivity

4.3.1   Distance Study

4.3.1.1   Simulation

The sensitivity of the Radiation Compass view angle to different source distances was first studied using the simulation results of Set 3 from Table 3.3, as described in Section 3.3. Eleven distances from 0 cm to 100 cm in increments of 10 cm were simulated for three different view angles, 0°, 45°, and 90°, all at a source angle of 0°. Figure 4.15 shows the simulated efficiencies for the three view angles of interest over the eleven distances simulated.

Figure 4.15b shows the summed efficiencies of all detector panels over the eleven distances. The total Radiation Compass absolute efficiency at a view angle of 0° begins to equal that of the total absolute efficiency at a view angle of 45° at approximately 40 cm, within the error bars. Similarly, the total absolute efficiency at view angles of both 0° and 45° begins to equal the total absolute efficiency at a view angle of 90° at approximately 70 cm. The trend described above is expected since at large distances compared to the size of the panels, the difference in geometric efficiency of each panel compared to each other panel becomes very small.

Figure 4.15c shows the absolute efficiency of panel 0 over the eleven distances. The efficiency of panel 0 is expected to be at a maximum when the view angle is equal to the vertical angle between the source and the Radiation Compass center
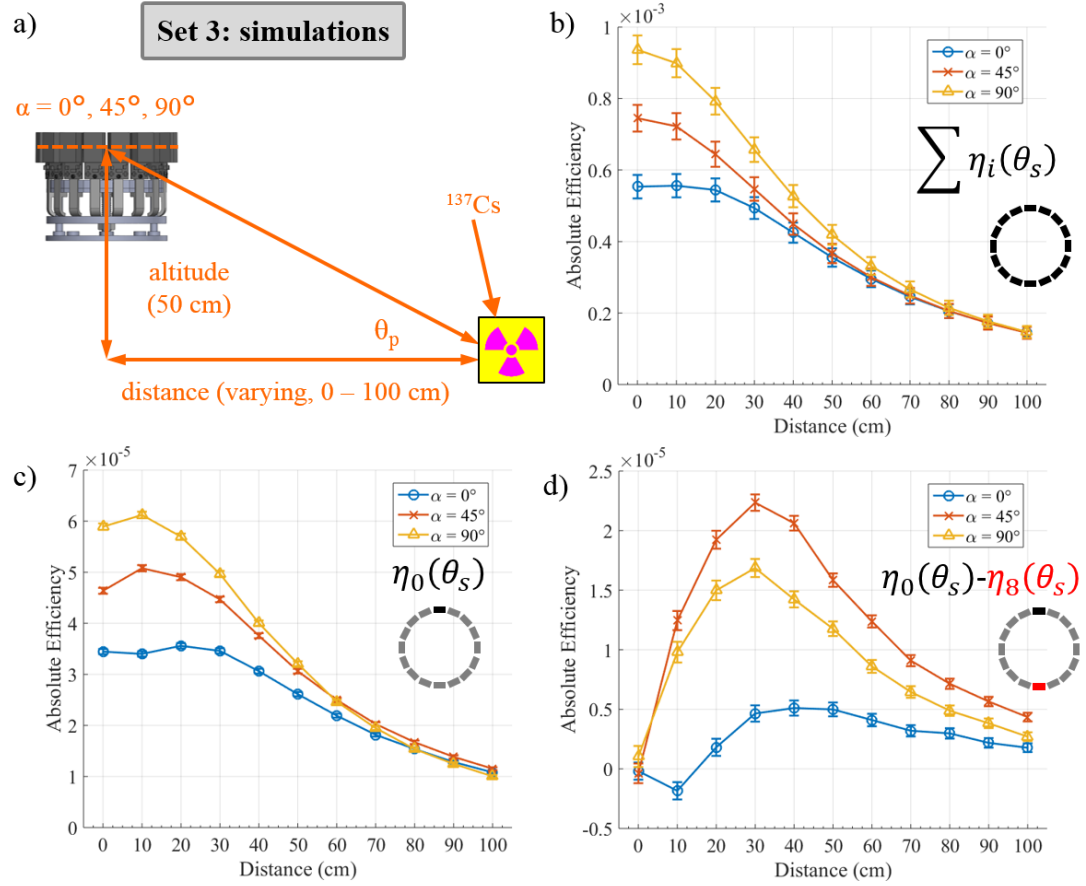
Figure 4.15: Simulated efficiency results for varying source distances and view angles based on parameter Set 3; a) the simulated geometry of the Radiation Compass; b) the Radiation Compass total absolute detector efficiency, comprising of the summed absolute efficiencies of all panels, at the three view angles of interest over the range of source distances; c) the absolute detection efficiency of panel 0 at the three view angles of interest over the range of source distances; d) the difference in absolute detection efficiency between panel 0 and panel 8. The insets in parts b), c), and d) show the formula for the values on the plots, as well as a diagram of the Radiation Compass detector panels.

point, θ_p. However, because the detector panels' rotation axis is not at the center of the BGO crystal, the absolute efficiency of detector panel 0 at a view angle of

45° begins to surpass that of detector panel 0 at a view angle of 90° at 60 cm, instead of 50 cm.

Figure 4.15d shows the absolute efficiency of panel 0 minus that of panel 8, which is opposite panel 0 on the Radiation Compass. The difference in absolute efficiencies for both the 45° and 90° view angles peak at 30 cm, indicating the greatest difference between the geometric efficiencies of panels 0 and 8. The difference in absolute efficiencies at a view angle of 0° is negative at 10 cm since the solid angle of the point source is subtended by the smallest face of the BGO in panel 0, but is subtended by both the largest and smallest faces of panel 8. All three view angles show a difference in absolute efficiencies of approximately zero at a distance of 0 cm, which is expected since the absolute efficiencies of all panels should be equal. At 100 cm, it is shown that the difference in absolute efficiencies between panels 0 and 8 remain greater than zero, indicating that the Radiation Compass retains directional sensitivity at this distance. Two additional simulations were carried out for view angles of 0° at a 50 cm altitude: one at a distance of 500 cm and one at a distance of 1000 cm. The Radiation Compass response patterns for these two distances, in addition to a 100 cm distance, are shown in Figure 4.16. These distances were simulated in order to assess the directional response of the Radiation Compass at distances over 100 cm. No measurements were taken at these distances since sources with sufficient activity were not available.

d = 100 cm,
α = 0°

d = 500 cm,
α = 0°
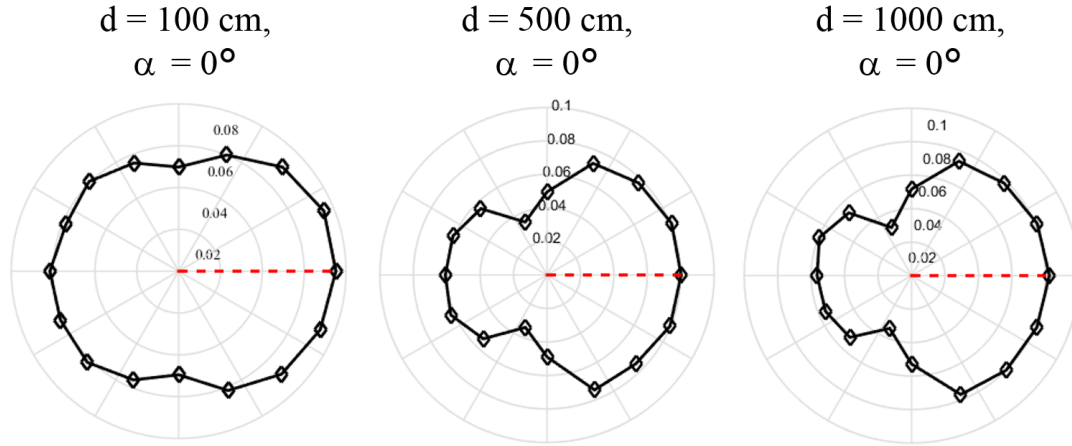
d = 1000 cm,
α = 0°

Figure 4.16: Simulated Radiation Compass response patterns for 100, 500, and 1000 cm distances at an altitude of 50 cm. Directional response patterns are still able to be observed at these distances.

4.3.1.2 Measurement

The sensitivity of the Radiation Compass view angle to different source distances was studied through measurement using the parameters in Set 3 from Table 3.3, pictured in Figure 4.17. Instead of an altitude of 50 cm, however, the Radiation Compass was positioned at an altitude of 51.5 cm. As with the simulations, eleven source distances were used, from 0 cm to 100 cm in 10 cm intervals, at three view angles: 0°, 45°, and 90°. A 9 µCi ^{137}Cs was used at a source angle of 0° for each distance, and each the time for each measurement was 5 minutes. Figure 4.18 shows the measured count rates for the three view angles of interest over the eleven distances measured. The trends shown in Figure 4.18 match closely with those shown in Figure 4.15, validating the trends in view angle sensitivity with relation to distance shown via simulation above. As mentioned previously, larger
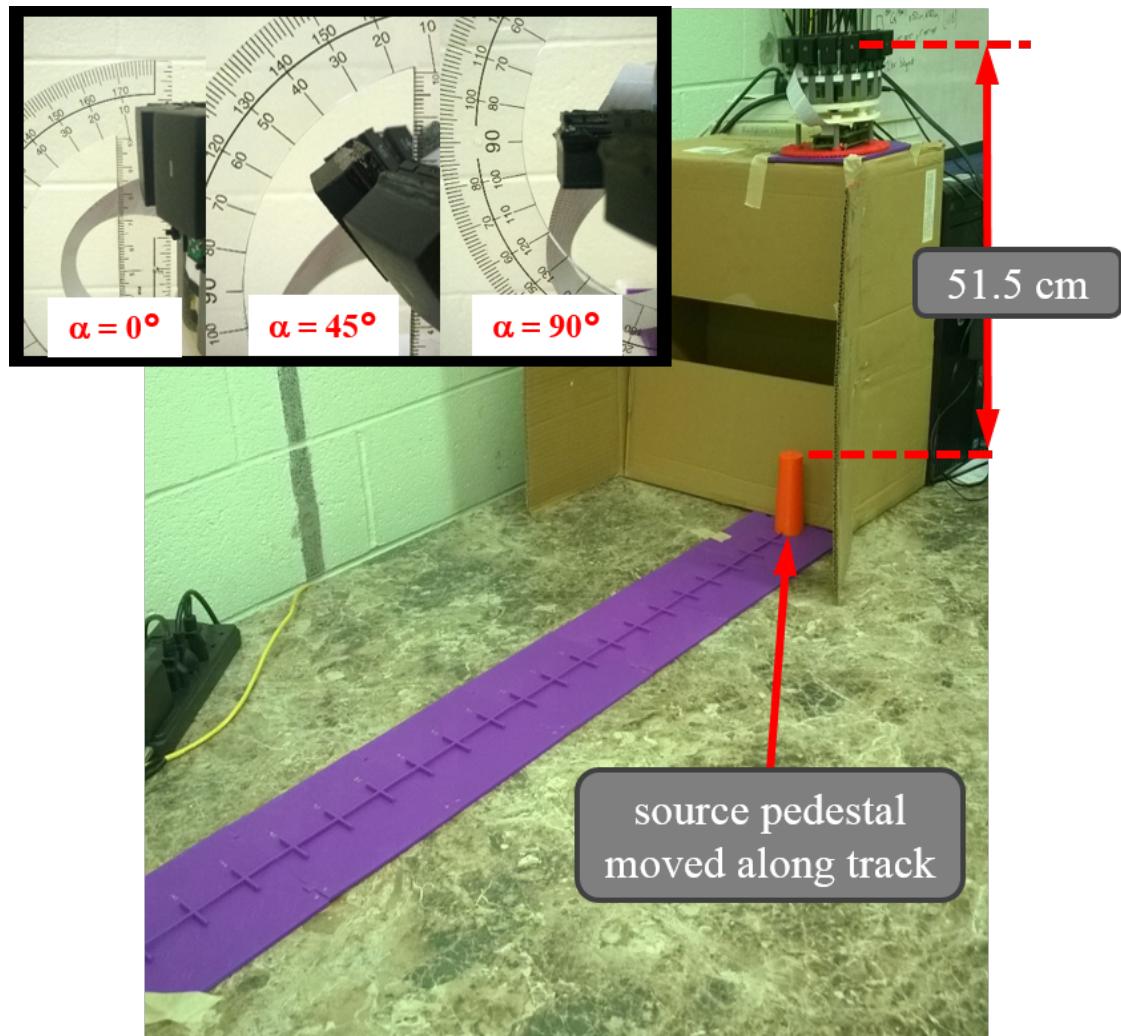
Figure 4.17: Photo of the setup for measuring the distance sensitivity of the Radiation Compass, with an inset showing the detector panels set at the three different view angles of interest.

source distances were not measured since sources with sufficient activity were not available.

Figure 4.18b shows the summed count rates of all detector panels over the
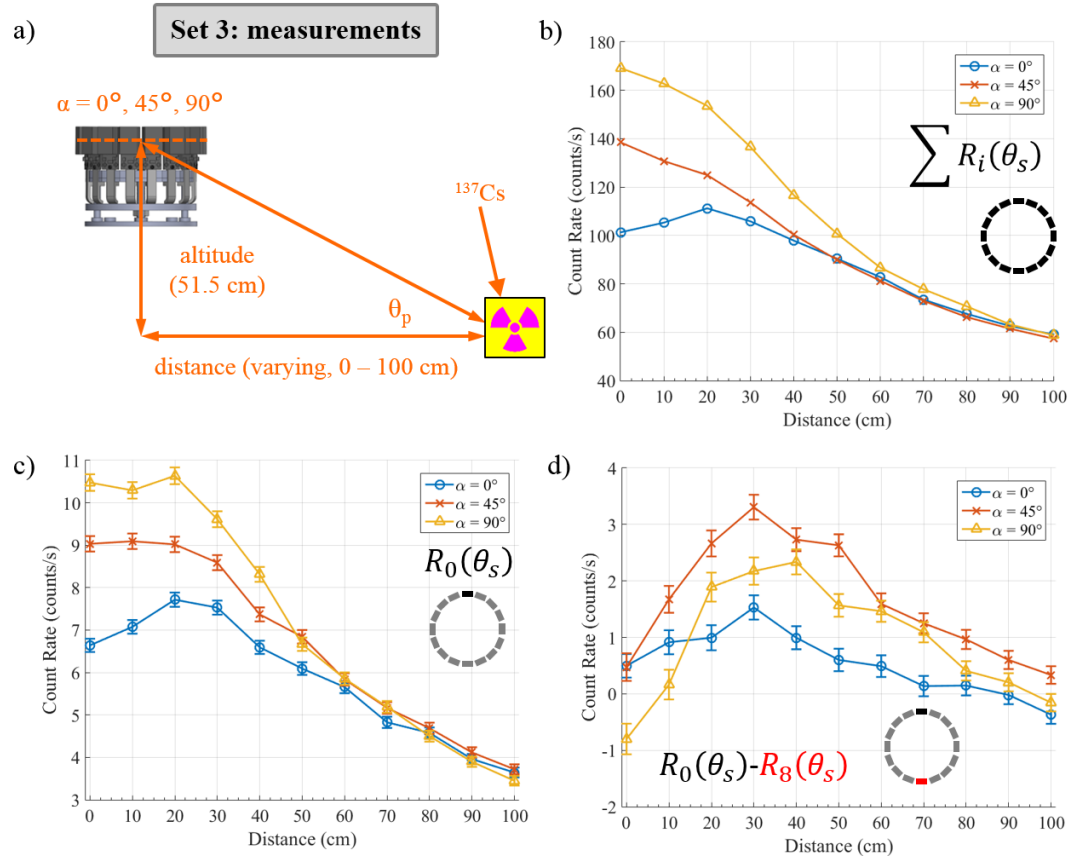
Figure 4.18: Measured count rate results for varying source distances and view angles; a) the measured geometry of the Radiation Compass; b) the Radiation Compass total count rate, comprising of the summed count rates of all panels, at the three view angles of interest over the range of source distances; c) the count rate of panel 0 at the three view angles of interest over the range of source distances; d) the difference in count rates between panel 0 and panel 8 at the three view angles of interest over the range of source distances. Errorbars in part b) are included in the size of the plotted markers. The insets in parts b), c), and d) show the formula for the values on the plots, as well as a diagram of the Radiation Compass detector panels.

eleven distances. The total Radiation Compass count rate at a view angle of 0° begins to equal that of the total absolute efficiency at a view angle of 45° at

approximately 50 cm. Similarly, the total absolute efficiency at view angles of both 0° and 45 ° begins to equal the total absolute efficiency at a view angle of 90° at approximately 90 cm. The larger distance of these intersection points compared to simulation is likely due to the increased thresholds of the measurements compared to the simulations.

Figure 4.18c shows the count rate of panel 0 over the eleven distances. The count rate of panel 0 is expected to be at a maximum when the view angle is equal to the vertical angle between the source and the Radiation Compass center point, θ_p. The measurements show that the count rate of panel 0 at a view angle of 45° begins to equal that at a view angle of 90° at 50 m, where the view angle is approximately equal to θ_p.

Figure 4.18d shows the count rate of panel 0 minus that of panel 8, which is opposite panel 0 on the Radiation Compass. The difference in absolute efficiencies for both the 45° and 90° view angles peak at 30 cm, indicating the greatest difference between the geometric efficiencies of panels 0 and 8. The difference in absolute efficiencies at a view angle of 0° is negative at 10 cm since the solid angle of the point source is subtended by the smallest face of the BGO in panel 0, but is subtended by both the largest and smallest faces of panel 8. All three view angles show a difference in absolute efficiencies of approximately zero at a distance of 0 cm, which is expected since the absolute efficiencies of all panels should be equal. At 100 cm, it is shown that the difference in absolute efficiencies between panels 0 and 8 remain greater than zero, indicating that the Radiation Compass retains directional sensitivity at this distance. Two additional simulations were

carried out for view angles of 0° at a 50 cm altitude: one at a distance of 500 cm and one at a distance of 1000 cm. The Radiation Compass response patterns for these two distances, in addition to a 100 cm distance, are shown in Figure 4.16. These distances were simulated in order to assess the directional response of the Radiation Compass at distances over 100 cm. As mentioned previously, no measurements were taken at these distances since sources with sufficient activity were not available.

A comparison between the simulated and measured Radiation Compass response patterns for parameter Set 3 at a set of view angles and distances of interest is shown in Figures 4.19, 4.20, and 4.21, where the simulated responses, without any added background, are shown on the left and the measured responses, measured for 5 minutes with a background rate of 0.82 counts per second per panel, are shown on the right of each figure. The dashed red lines show the true source angle. As mentioned in Section 4.3.1.2, the measured responses appear less distinct than the expected response patterns likely both because of the addition of background counts to the measured patterns and the higher energy thresholds of the radiation detector panels compared to the simulated threshold. The measured responses do follow the weight trends of the simulated response patterns, however. In all three figures 4.19, 4.20, and 4.21, the detector response grows more distinct as the source is moved further away from the center of the Radiation Compass. As expected, the detector response pattern at 45° shown in Figure 4.20, is the most distinct of the three view angles studied when the source is 50 cm from the Radiation Compass center point in terms of the greatest weight in panel 0.

$\alpha = 0°$, $d = 0$ cm

$\alpha = 0°$, $d = 50$ cm

$\alpha = 0°$, $d = 100$ cm
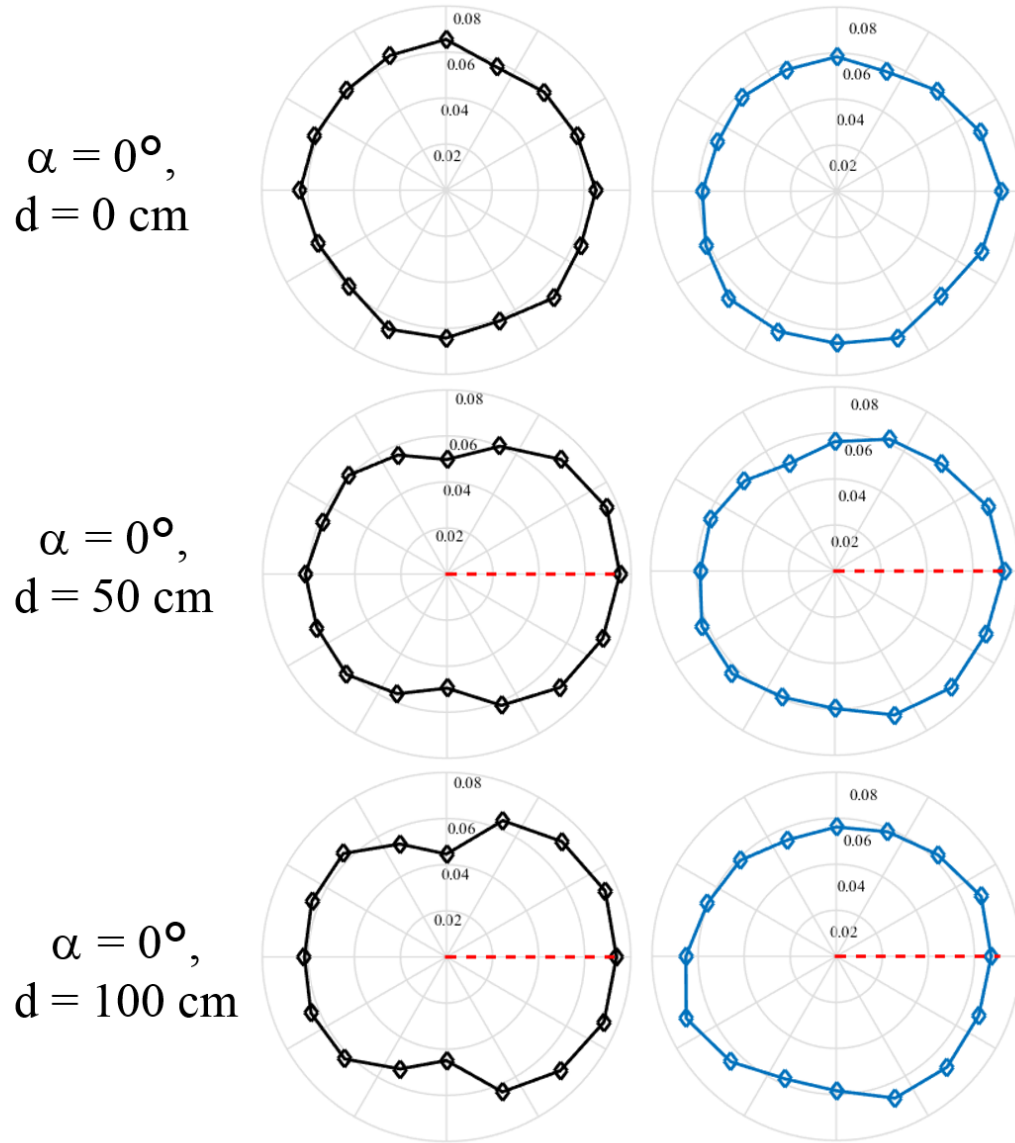
Figure 4.19: Comparison between simulated and measured detector response patterns for parameter Set 3 at a view angle of 0°, at three distances of interest. The simulated responses, without any added background, are shown in black across the left, and the measured responses, with a background rate of 0.82 counts per second per panel, are shown in blue across the right. The dashed red lines indicate the true source angles, which are not present in the two top plots since the source was centered below the Radiation Compass.

α = 45°,
d = 0 cm

α = 45°,
d = 50 cm

α = 45°,
d = 100 cm
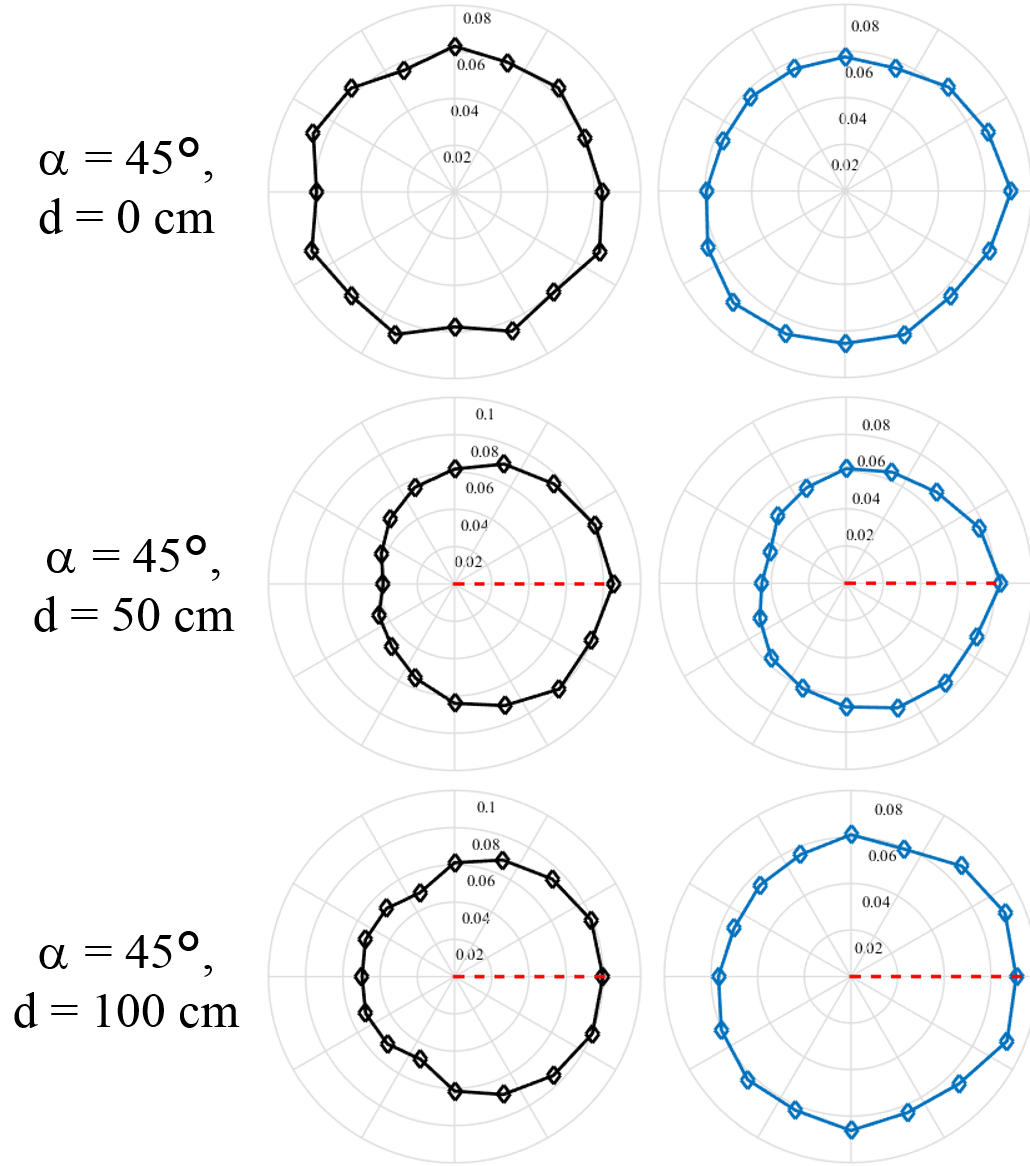
Figure 4.20: Comparison between simulated and measured detector response patterns for parameter Set 3 at a view angle of 45°, at three distances of interest. The simulated responses, without any added background, are shown in black across the left, and the measured responses, with a background rate of 0.82 counts per second per panel, are shown in blue across the right. The dashed red lines indicate the true source angles, which are not present in the two top plots since the source was centered below the Radiation Compass.

α = 90°,
d = 0 cm

α = 90°,
d = 50 cm

α = 90°,
d = 100 cm
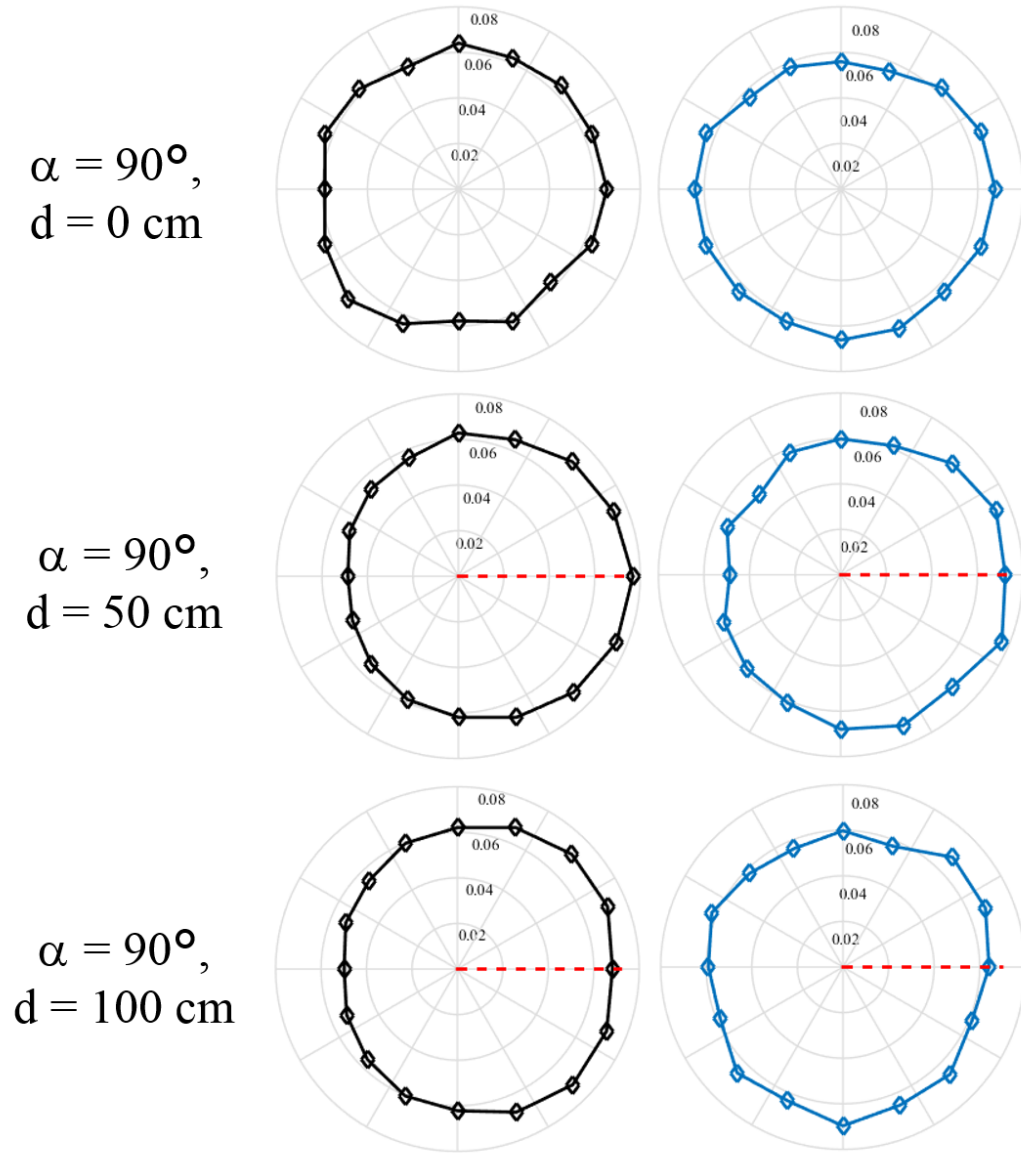
Figure 4.21: Comparison between simulated and measured detector response patterns for parameter Set 3 at a view angle of 90°, at three distances of interest. The simulated responses, without any added background, are shown in black across the left, and the measured responses, with a background rate of 0.82 counts per second per panel, are shown in blue across the right. The dashed red lines indicate the true source angles, which are not present in the two top plots since the source was centered below the Radiation Compass.

4.3.2 View Angle Study 1: 50 cm Distance

4.3.2.1 Simulation

The view angle sensitivity of the Radiation Compass was first studied using the simulation results of Set 4 from Table 3.3, as described in Section 3.3. Five view angles were simulated: 0°, 30°, 45°, 60°, and 90°. The source angle was held at 0°, and the altitude and distance both held at 50 cm. Figure 4.22 shows the simulated efficiencies for the five view angles of interest.

Figure 4.22b shows the summed efficiencies of all detector panels over the five view angles. The total Radiation Compass absolute efficiency continues to increase as the view angle increases, where it reaches a maximum at 90°. As explained in the section above, the increasing total absolute efficiency is due to the decreasing attenuation of the gamma ray flux by the detector panels closer to the source for those on the opposite side of the Radiation Compass.

Figure 4.22c shows the absolute efficiency of panel 0 over the five view angles of interest. The efficiency of panel 0 is expected to be at a maximum when the view angle is equal to the angle between the source and the Radiation Compass center point, θ_p, which should be 45 ° in this case. However, because the detector panels' rotation axis is not at the center of the BGO crystal, the absolute efficiency of detector panel 0 reaches maximum absolute efficiency at a view angle of 90°.

Figure 4.22d shows the absolute efficiency of panel 0 minus that of panel 8, which is opposite panel 0 on the Radiation Compass. The absolute efficiency difference between the two panels is largest at 45° and 60° when error bars are

Figure 4.22: Simulated efficiency results for varying view angles at a fixed distance and altitude based on Set 4; a) the simulated geometry of the Radiation Compass; b) the Radiation Compass total absolute detector efficiency, comprising of the summed absolute efficiencies of all panels, over the five view angles of interest; c) the absolute detection efficiency of panel 0 over the five view angles of interest; d) the difference in absolute detection efficiency between panel 0 and panel 8 over the five view angles of interest. The insets in parts b), c), and d) show the formula for the values on the plots, as well as a diagram of the Radiation Compass detector panels.

considered.

4.3.3 Measurement

The view angle sensitivity of the Radiation Compass was studied through measurement using the parameters in Set 4 from Table 3.3, pictured in Figure 4.23. Instead of an altitude of 50 cm, however, the Radiation Compass was positioned
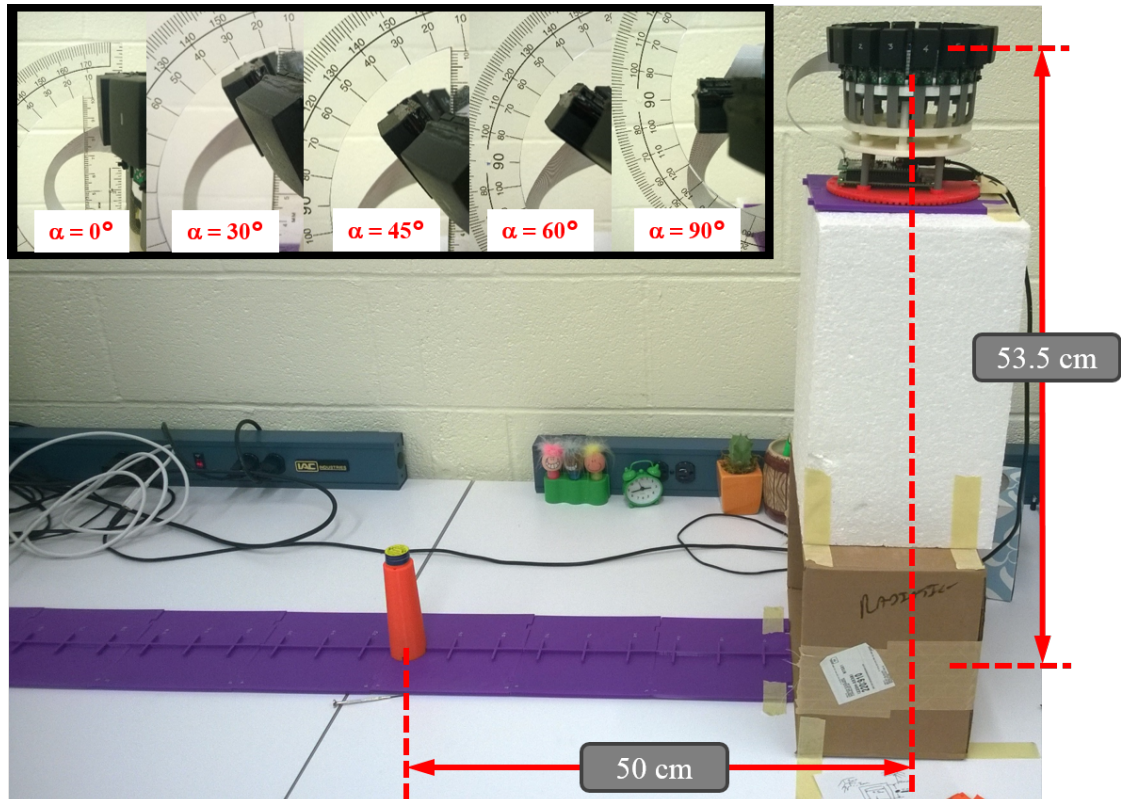
Figure 4.23: Photo of the setup for studying the view angle sensitivity of the Radiation Compass at a source distance of 50 cm, with an inset showing the detector panels set at the five different view angles of interest.

at an altitude of 53.5 cm. As with the simulations, five different view angles were used: 0°, 30°, 45°, 60°, and 90°. A 12.3 µCi ^{137}Cs was used at a source angle of 0° at a fixed distance of 50 cm. Five 5-minute measurements were taken at each view

angle. Figure 4.24 shows the measured count rates over the five view angles of interest measured, averaged over the five measurements for each view angle. The trends shown in Figure 4.24 match those shown in Figure 4.22. Differences are likely due to the difference in energy thresholds between the simulations and measurements. However, they give some validation to the distance sensitivity trends shown via simulation above.

A comparison between the simulated and measured Radiation Compass response patterns for each of the source angles of interest is shown in Figure 4.25, where the simulated responses are shown on top and the measured responses shown on the bottom. The dashed red lines show the true source angle. The measured responses appear less distinct than the expected response patterns likely both because of the addition of background counts to the measured patterns and the higher energy thresholds of the radiation detector panels than were simulated.
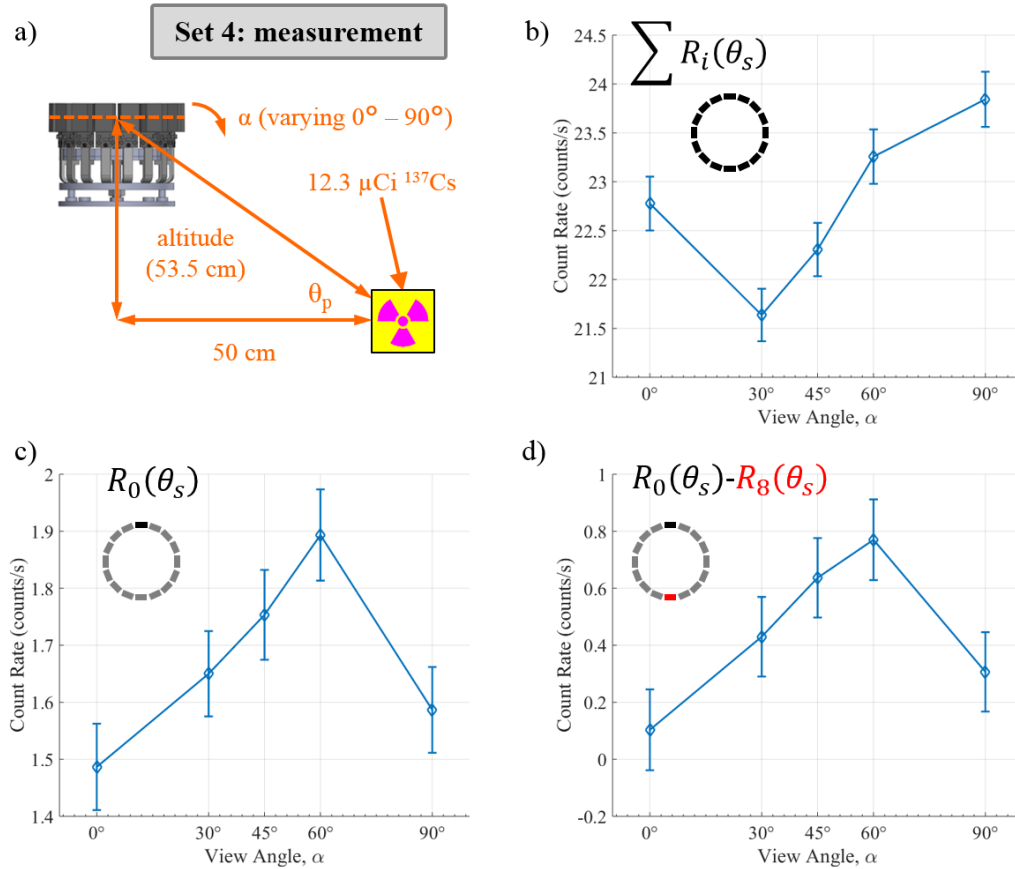
Figure 4.24: Measured count rate results for varying view angles at a fixed distance and altitude based on parameter Set 4; a) the measured geometry of the Radiation Compass; b) the Radiation Compass total count rate, comprising of the summed count rates of all panels, at the five view angles of interest; c) the count rate of panel 0 at the five view angles of interest; d) the difference in count rates between panel 0 and panel 8 at the five view angles of interest. The insets in parts b), c), and d) show the formula for the values on the plots, as well as a diagram of the Radiation Compass detector panels.
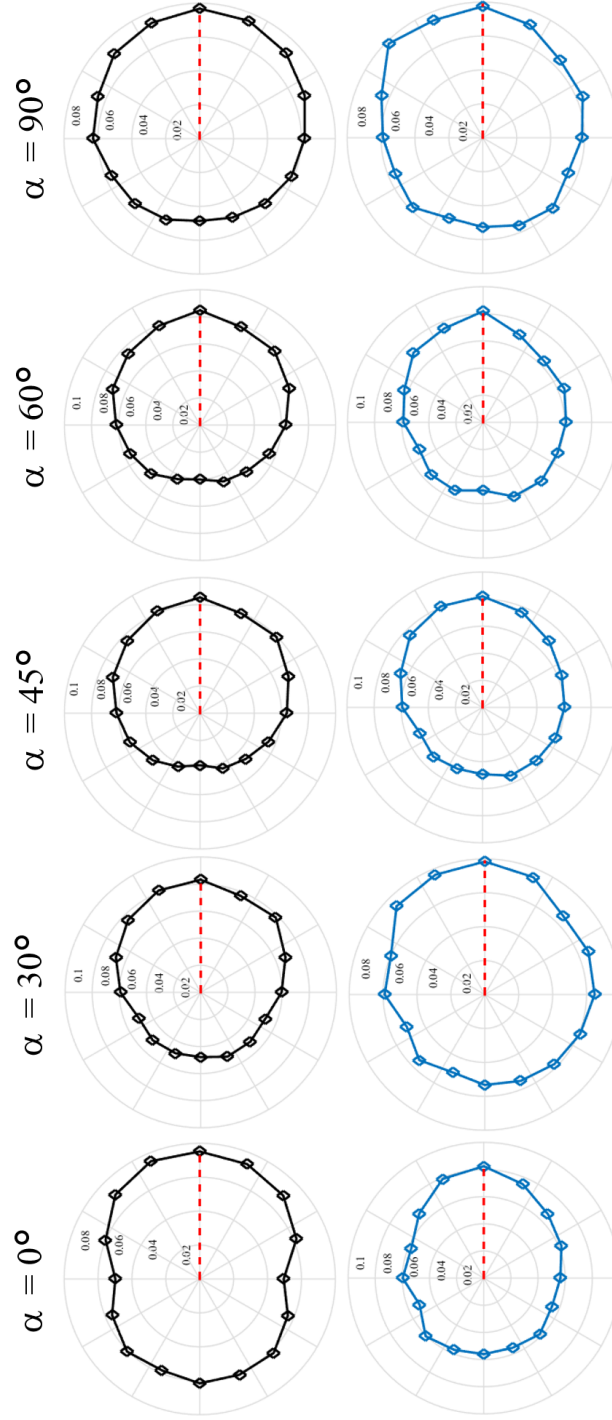
Figure 4.25: Comparison between simulated and measured detector response patterns for parameter Set 4 at the five view angles of interest. The simulated responses, without any added background, are shown in black across the top, and the measured responses, with a background rate of 0.82 counts per second per panel, are shown in blue across the bottom. The dashed red lines indicate the true source angles.

4.3.4   View Angle Study 2: 100 cm Distance

4.3.4.1   Simulation

The view angle sensitivity of the Radiation Compass was further studied using the simulation results of Set 5 from Table 3.3, as described in Section 3.3. The same five view angles from Set 4 were again simulated: 0°, 30°, 45°, 60°, and 90°. The source angle was held at 0°, the altitude held at 50 cm and the distance now held at 100 cm. Figure 4.26 shows the simulated efficiencies for the five view angles of interest.

Figure 4.26b shows the summed efficiencies of all detector panels over the five view angles. Though there is some slight variation in the absolute efficiency at different view angles, the total absolute efficiency of the Radiation Compass is relatively constant across the five angles when considering the error bars.

Figure 4.26c shows the absolute efficiency of panel 0 over the five view angles of interest. As in the case of a source 50 cm from the Radiation Compass center point, the efficiency of panel 0 is expected to be at a maximum when the view angle is equal to the angle between the source and the Radiation Compass center point, θ_p. However, the simulations show that the absolute effiiency of panel 0 is at a maximum at view angles of 30°, 45°, and 60°, considering error bars. There is, however, a significant difference between the absolute effiiency at these three view angles and the absolute efficiency at view angles of 0° and 90°.

Figure 4.26d shows the absolute efficiency of panel 0 minus that of panel 8, which is opposite panel 0 on the Radiation Compass. The absolute efficiency
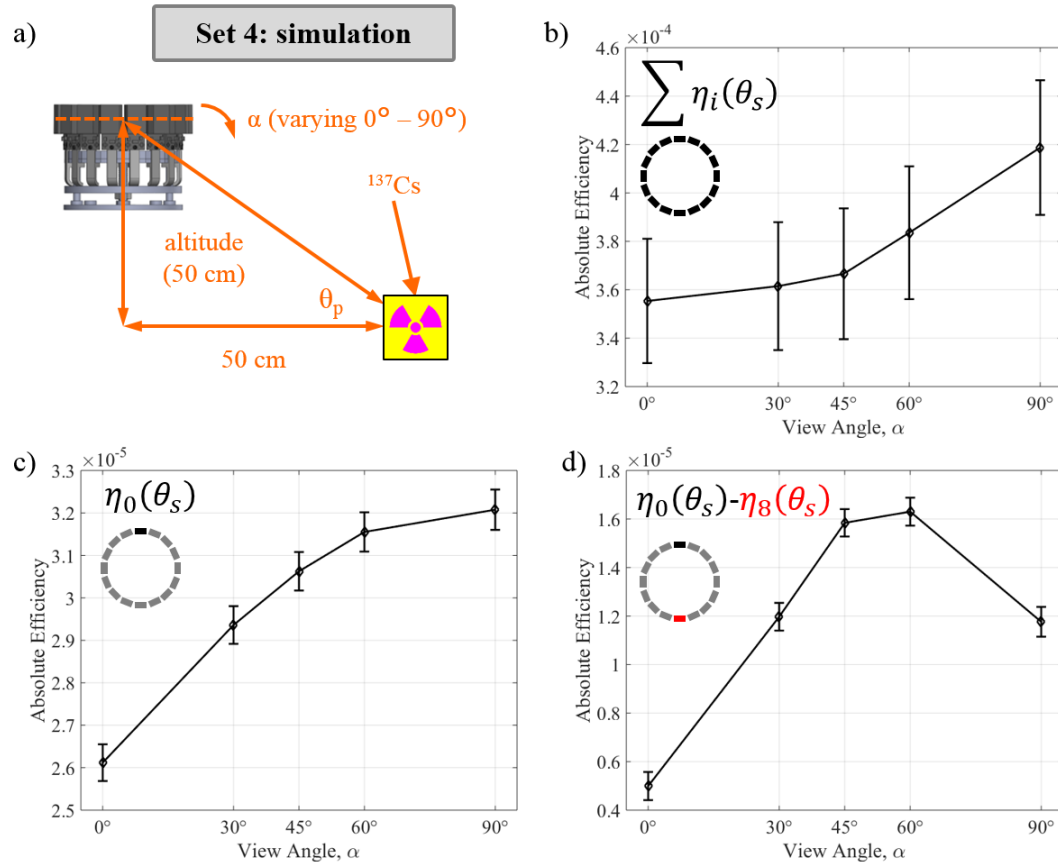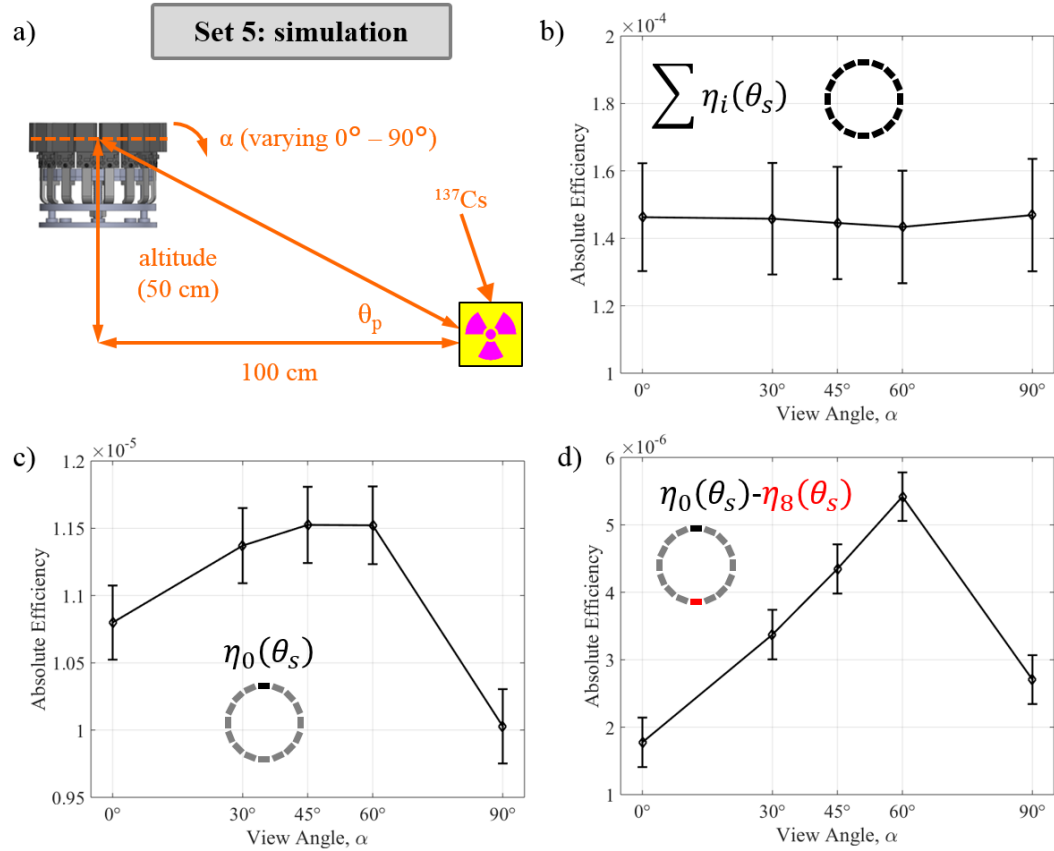
Figure 4.26: Simulated efficiency results for varying view angles at a fixed distance and altitude based on parameter Set 5; a) the simulated geometry of the Radiation Compass; b) the Radiation Compass total absolute detector efficiency, comprising of the summed absolute efficiencies of all panels, over the five view angles of interest; c) the absolute detection efficiency of panel 0 over the five view angles of interest; d) the difference in absolute detection efficiency between panel 0 and panel 8 over the five view angles of interest. The insets in parts b), c), and d) show the formula for the values on the plots, as well as a diagram of the Radiation Compass detector panels.

difference between the two panels reaches its maximum at a view angle of 60°.

Each of the three estimation methods was implemented on data simulated for

each of the five view angles. As described in Section 3.3.2, the source angle estimated by each method was recorded for all 10,000 simulations and the MSE calculated for each method. Plots of MSE versus source strength for each estimation method and view angle are shown in Figure 4.27, and plots of MSE versus view angle for each estimation method at 10 µCi is shown in Figure 4.28. An example of the convergence of the estimation methods for increasing source activities at a view angle of 30° is shown in Figure 4.29.

Figure 4.27 shows the effect of the view angle on the MSE of each estimator. The MSE of all three methods at a view angle of 0°is higher than their MSE at the other five view angles. The MSE of the three estimation methods is on the same order of magnitude at view angles of 45°, 60°, and 90°, with the Matched Filter method clearly outperforming the Symmetry and Maximum Likelihood methods at view angles of 45° and 60°. However, at a view angle of 30° the Matched Filter method shows a significantly smaller MSE compared to the Symmetry and Maximum Likelihood methods, as well as compared to other view angles, demonstrating the value of changing the view angle in more accurately estimating the source direction.

Figure 4.28 shows that at 10 µCi, the Matched Filter method shows the smallest MSE at all view angles except 90°, but no view angle shows the smallest MSE for all three methods. As shown in Figure 4.27, the Matched Filter method shows a significantly smaller MSE at a view angle of 30° compared to the Matched Filter MSE at other view angles, as well as compared to the MSE of the other two estimators.
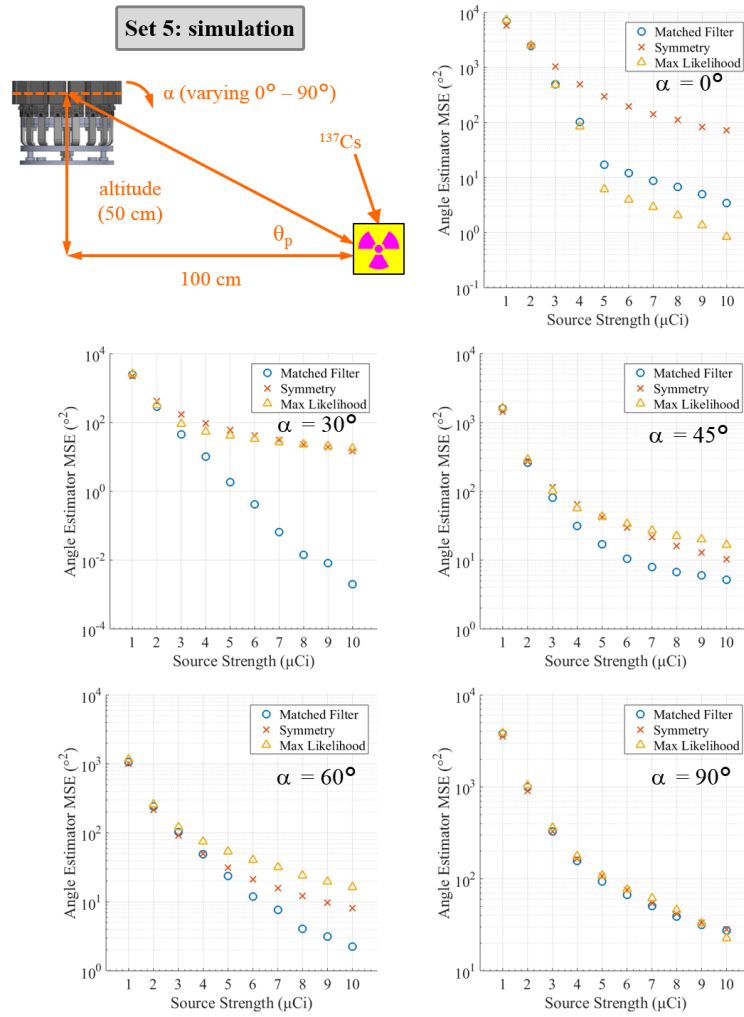
Figure 4.27: Simulated mean squared error of each of the three estimation methods over ten source activities, simulated at five different view angles.
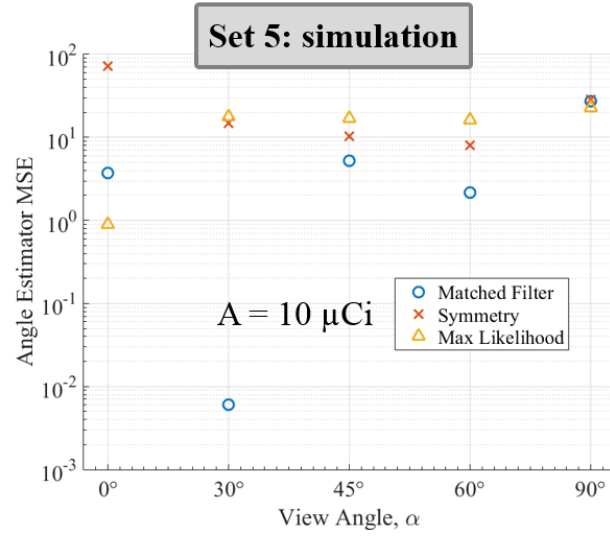
Figure 4.28: Simulated mean squared error of each of the three estimation methods over five different view angles, at 10 µCi.
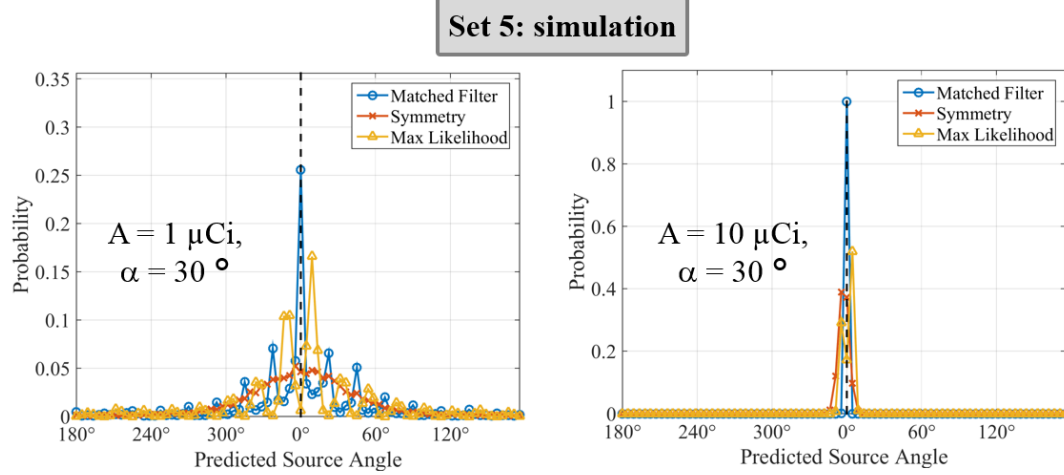
Figure 4.29: Histograms of the number of times each source angle was estimated by each of the three direction estimation methods, where the black dashed line indicates the true source angle. The number of times each angle was estimated is normalized by the total number of simulations run labeled as the probability.

4.3.5 Measurements

The accuracy of each of the direction estimation methods for the five view angles of interest was studied through measurement using the parameters in Set 5 from Table 3.3, pictured in Figure 4.30. Instead of an altitude of 50 cm, however,
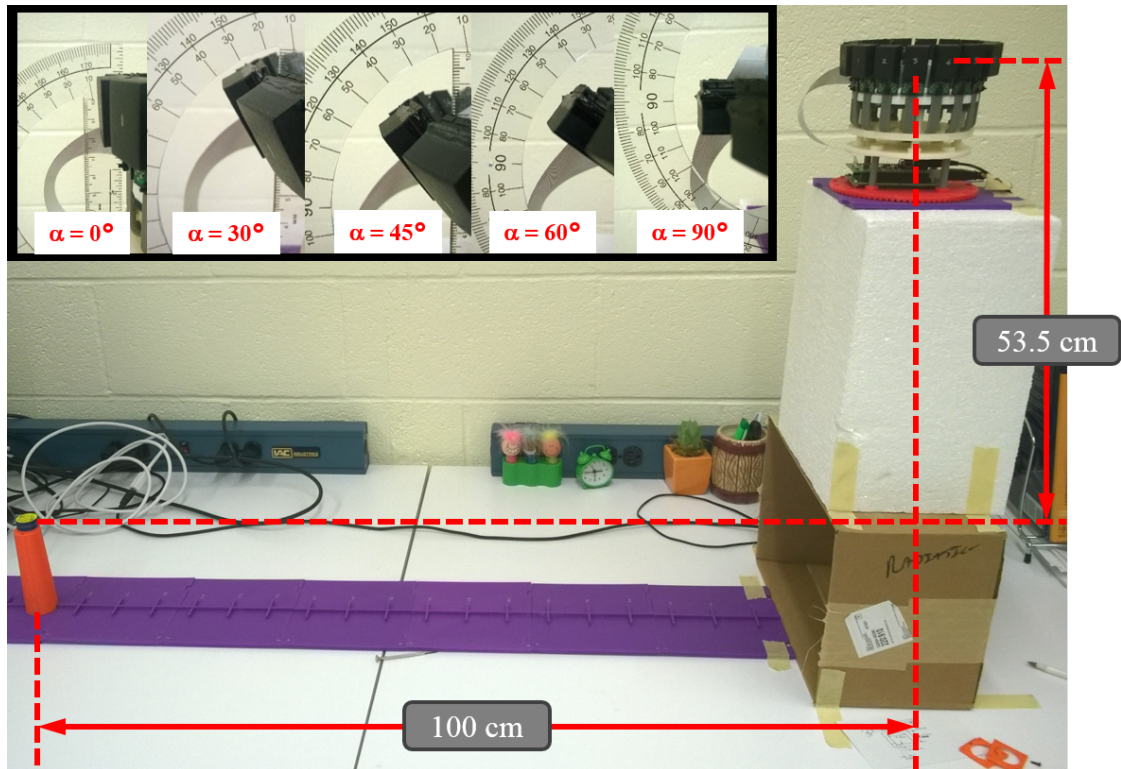
Figure 4.30: Photo of the setup used to investigate the view angle sensitivity at a source distance of 100 cm, with an inset showing the detector panels set at the five different view angles of interest.

the Radiation Compass was positioned at an altitude of 53.5 cm. As with the simulations, five different view angles were used: 0°, 30°, 45°, 60°, and 90°. In order to show the effect of changing the view angle on the count rate, one measurement

at each source angle was performed for 15 minutes using a 12.3 µCi ^{137}Cs source at a source angle of 0°. Figure 4.31 shows the measured count rates over the five view angles of interest measured. The trends shown in Figure 4.31 do not match those shown in Figure 4.26 well, but do show that the highest count rate observed in panel 0 was at a view angle of 30°, when the view angle is equal to the angle between the ground and a line connecting the source to the Radiation Compass center.

To measure the MSE of each estimator method at each view angle, a 12.3 µCi ^{137}Cs was used at a source angle of 0° at a fixed distance of 100 cm, and ten 3-minute measurements were taken at each view angle. The direction estimation methods were then applied to each measurement and the MSE of each method recorded, shown in Figure 4.32. The Matched Filter method again showed the lowest total MSE across all five view angles.

The accuracy for each estimation method for each set of ten measurements was quantified for the five view angles of interest using the absolute value of the bias, where the bias is:

$$Bias = \bar{\hat{\theta}} - \theta_s, \tag{4.4}$$

where $\bar{\hat{\theta}}$ is the mean estimated angle and θ_s is the true source angle. The precision for each estimation method for each set of ten measurements was quantified using the 95% confidence interval, calculated using the cumulative normal distribution function, where $\Phi(z) = P(Z \leq z) = 1 - \alpha/2 = 0.975$. The results of this analysis
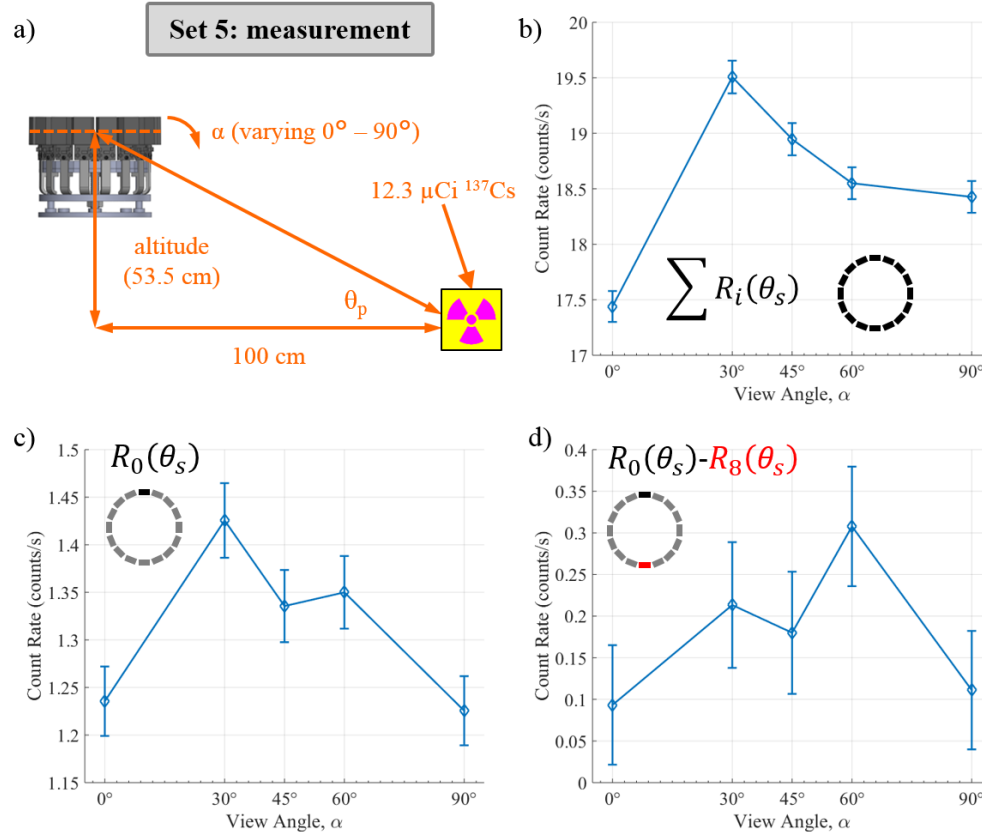
Figure 4.31: Measured count rate results for varying view angles at a fixed distance and altitude based on parameter Set 5; a) the measured geometry of the Radiation Compass; b) the Radiation Compass total count rate, comprising of the summed count rates of all panels, at the five view angles of interest; c) the count rate of panel 0 at the five view angles of interest; d) the difference in count rates between panel 0 and panel 8 at the five view angles of interest. The insets in parts b), c), and d) show the formula for the values on the plots, as well as a diagram of the Radiation Compass detector panels.

are listed in Tables 4.3 and 4.4, and shown in Figure 4.33. The Matched Filter method shows the best overall accuracy since it has the lowest bias values at three of the five view angles of interest, and shows the best overall precision since it has
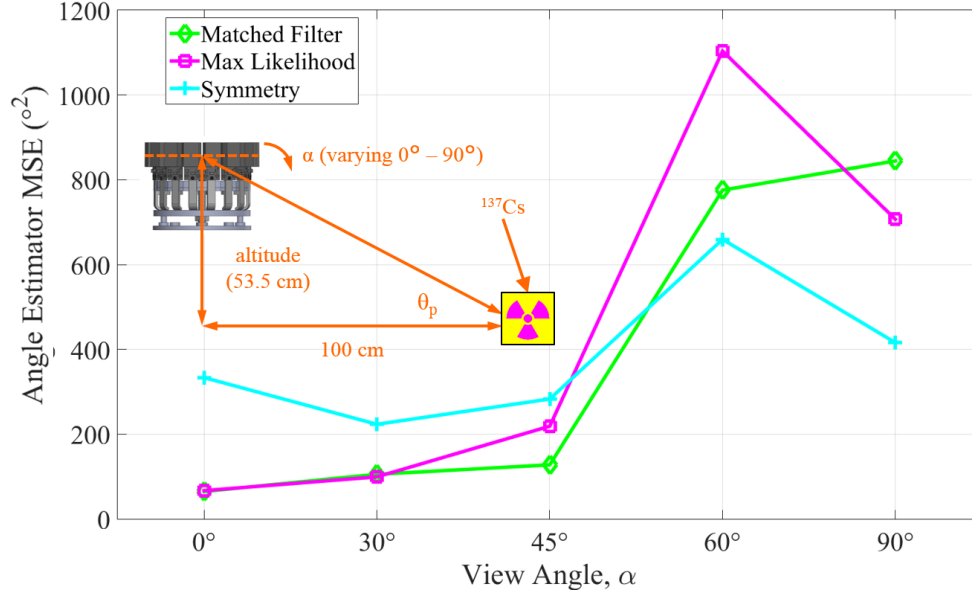
Figure 4.32: Measured mean squared error of each of the three direction estimation methods at each of the five view angles of interest.

the lowest 95% confidence width at three of the five view angles of interest.

Table 4.3: Table of the absolute value of the bias of each estimation method for the measurements based on Set 5.

view angle, α	Estimator $|Bias|$		
	Symmetry	Matched Filter	Max Likelihood
0°	16.8°	1.8°	0.5°
30°	6.0°	4.5°	5.0°
45°	14.2°	5.0°	7.2°
60°	9.1°	5.9°	4.1°
90°	3.1°	2.3°	5.9°

A comparison between the simulated and measured Radiation Compass response patterns for each of the view angles of interest is shown in Figure 4.34, where the simulated responses are shown on top and the measured responses shown
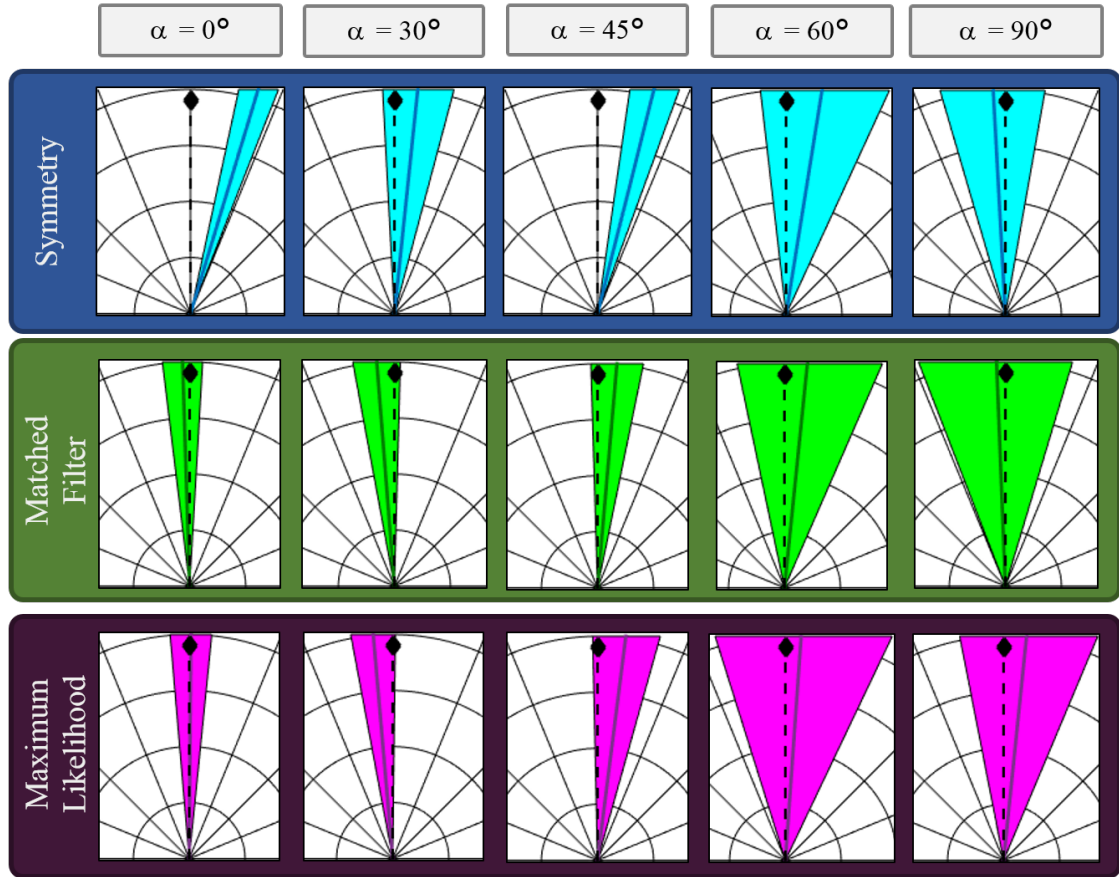
Figure 4.33: Radar plots showing the mean estimated angles and 95% confidence intervals for the measurements based on Set 5. The 95% confidence intervals are represented as triangles, each with a color corresponding to the estimation method labeled to the left. The mean estimated angle for each method at each angle is shown as a solid line in a darker shade of the confidence interval color. The true source angle is labeled as a black dashed line with a black diamond at one end.

on the bottom. The dashed red lines show the true source angle, which was held at 0° for all measurements. The measured response patterns shown were generated using the 15 minute measurements mentioned above. As discussed previously, the measured responses appear less distinct than the expected response patterns likely

Table 4.4: Table of estimator method 95% confidence intervals for the measurements based on Set 5.

view	95% confidence interval		
angle, α	Symmetry	Matched Filter	Max Likelihood
0°	[12.2°,21.5°]	[-6.9°,3.3°]	[-4.9°,5.8°]
30°	[-3.0°,14.9°]	[-10.5°,1.5°]	[-10.6°,0.7°]
45°	[8.2°,20.1°]	[-1.7°,11.6°]	[-1.2°,15.6°]
60°	[-6.5°,24.8°]	[-11.9°,23.6°]	[-17.5°,25.6°]
90°	[-16.3°,10.1°]	[-21.2°,16.7°]	[-11.1°,22.8°]

both because of the addition of background counts to the measured patterns and the higher energy thresholds of the radiation detector panels than were simulated.
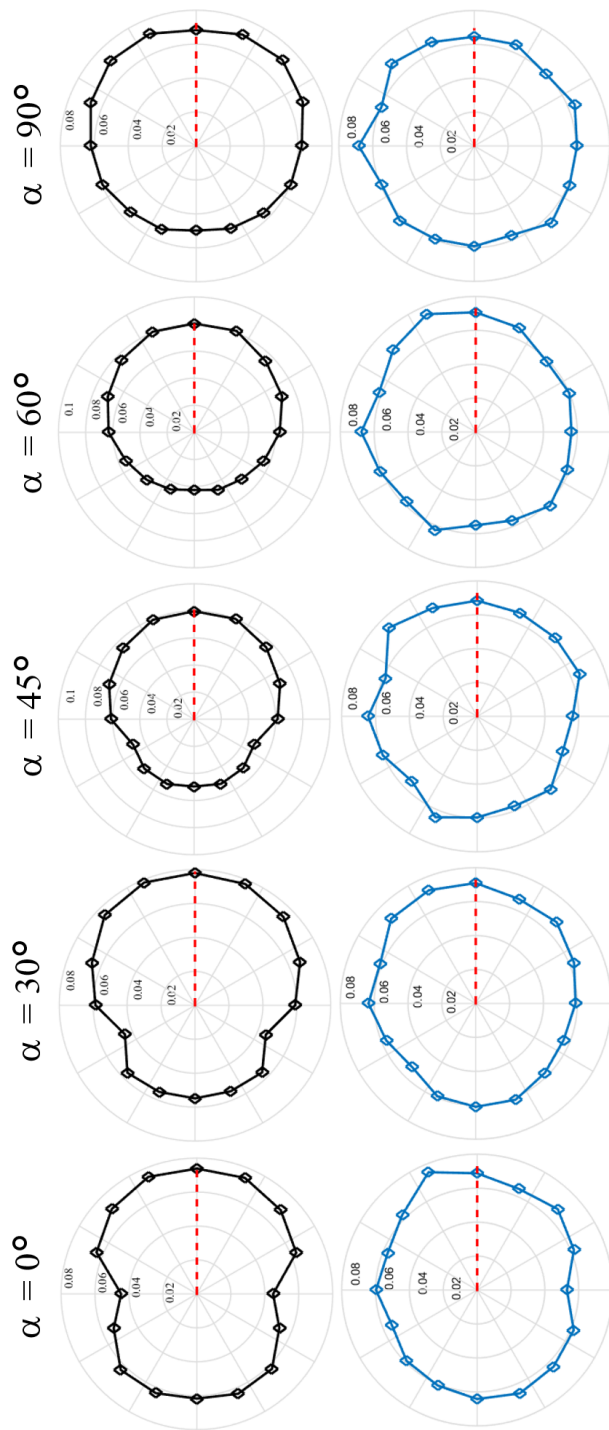
Figure 4.34: Comparison between simulated and measured detector response patterns for parameter Set 4 at each of the five view angles of interest. The simulated responses, without any added background, are shown in black across the top, and the measured responses, with a background rate of 0.82 counts per second per panel, are shown in blue across the bottom. The dashed red lines indicated the true source angles.

Chapter 5: Conclusions

5.1   Current Work

The Radiation Compass is a direction-sensitive radiation detector designed to be used with an low-altitude, low-cost unmanned aerial vehicle for radiological source searches. It was designed to be efficient, low-cost, and lightweight, as well as direction sensitive, in order to be able to locate radiological sources quickly and autonomously. Such a system is advantageous since it has increased gamma ray detection efficiency compared to high-altitude radiological search system, can effectively be used in motion, is low-cost, and is unmanned. Other current systems that can be used to search for radiological sources require human operators, are expensive, or are not suited to a faster, dynamic search methodology, such as Compton imagers, large arrays of radiation detectors, and radiation portal monitors.

The Radiation Compass prototype assembled for this work is based around sixteen radiation detector panels arranged in an evenly-spaced circular pattern. The direction sensitivity of the circular configuration is derived from the principles of the active mask, where radiation detectors positioned closer to a radiation source attenuate the radiation flux emitted by the source such that any detector positioned behind those closest to the source are exposed to a lower radiation flux. The circular arrangement of radiation detector panels leads to a detector response that

is dependent on the angle of the source relative to the center of the Radiation Compass, and unique for each angle. Each of the panels had a detection element composed of a BGO crystal and a SiPM. The SiPM was surface-mounted to a PCB, which also mounted the preamplifier and comparator. The PCBs were daisy-chained together using flat, flexible cables, allowing the detector signals to be read out in parallel.

The digital pulses generated by the panel comparators were tallied in parallel, in real-time using a FPGA. The FPGA was part of a digital counting module that was responsible for counting the detector panel pulses, communicating with a PC via USB connection, and generating the supply voltages for the SiPM, preamplifier, and comparator. The FPGA communication with the PC was facilitated via the host interface in the FPGA firmware and the MATLAB application programming interface. A graphical user interface was also implemented in MATLAB to allow the user to change run settings, control the FPGA recording state machine, and observe the detector panel counts tallied by the FPGA.

The radiation detector panels were mounted on an articulation platform that holds each of the sixteen panels in their circular arrangement, as well as allows the detector panels to rotate in unison via an arrangement of levers, springs, and movable plates. The rotation of the detector panels affords the Radiation Compass a degree of distance sensitivity by changing the geometric efficiency, thus changing the radiation detection efficiency. The articulation platform was rapidly prototyped and assembled using a combination of low-cost, lightweight, low-atomic number plastic and aluminum components, as well as custom-designed 3-D printed

parts.

Three direction-estimation methods were implemented and compared using the Radiation Compass. The first was the Symmetry method, where the detector panel positions relative to the Radiation Compass center point were weighted by the count rate observed in each panel. The weighted positions were then used to find a vector of symmetry that served as the directional indicator. The second method was the Matched Filter method, where measured detector responses were convolved through a library of expected detector responses obtained through simulation. The estimated direction corresponded to the maximum value resulting from the convolution. Finally, the Maximum Likelihood method was used, which also compared measured detector responses to expected responses, but instead calculated the probability of observing each response for each detector panel. The product of these responses for each source angle in the response library was then calculated, with the greatest product corresponding to the estimated source angle.

Several sets of simulations and measurements were undertaken in order to characterize the direction-sensitivity of the Radiation Compass as well as the effect of changing the view angle. The system performance was characterized based on simulations and laboratory measurements. The Radiation Compass was found to be able to detect the presence of a 10 µCi ^{137}Cs source at 100 cm in under 8 seconds at a total background count rate of 25.5 counts per second. The Matched Filter method was shown to have the best overall performance. The Radiation Compass was shown to be able to estimate the direction of a 12.3 µCi ^{137}Cs at a background rate of 13.12 counts per second 100 cm from the center point with an

accuracy of of 1.8° and a 95% confidence interval width of 8.6° using the Matched Filter method. The view angle sensitivity and direction estimation performance were also studied at an altitude of 50 cm and a source distance of 100 cm. The Matched Filter method was able to estimate the direction of a 12.3 μCi ^{137}Cs at a background rate of 13.12 counts per second 100 cm from the center point at an altitude of 50 cm with an accuracy of of 1.8° and a 95% confidence interval width of 10.2° in three minutes.

5.2   Future Work

5.2.1   Radiation Detector Panels

Improvements to the detector elements of the radiation detector panels, namely in lowering the energy threshold, can be made by adjusting the position and number of SiPMs used. In the prototype assembled for this work, only one SiPM was used coupled to one of the large faces of the BGO crystal. The light collection efficiency of the system could be improved by instead mounting two SiPMs at one of the 15 x 8 mm^2 faces of the BGO. The SiPMs would be mounted on a separate board that would in turn be mounted at 90° to the radiation detector panel PCB. Such a setup would ensure that reflector plates would not need to be used to completely wrap the BGO crystals since the two SiPMs would be able to nearly completely cover one side of the crystal.

In addition, newer models of SiPM can be used that posses greater fill-factor

and PDE. The SensL C- and J-series are good candidates [70, 71], both of which still have peak PDE sensitivity at 420 nm. The C-series is essentially a lower-noise version of the B-series used in this work, with a dark current of the C-series more than 16 times less than that of the B-series. The dark count rate of the C-series is also almost 18 times less than that of the B-series. The J-series is the newest design, based on through-silicon via (TSV) technology, allowing for an increased fill factor. Combined with the p-on-n silicon manufacturing, the J-series is able to achieve a PDE of 51% at 420 nm and has dark current and count rates 3 and 10 times less, respectively, than the B-series, though not as low as those of the C-series.

The resistor and capacitor values used on the radiation detector panels were chosen because of the dark current generated by the SiPM and the DC bias scheme used on the detector panels. The DC bias scheme allows the dark current of the SiPM to be transferred to the preamplifier input, generating a voltage offset at the preamplifier output. The offset limits the dynamic output range of the operation amplifier of the preamplifier circuit. An alternative bias scheme using an AC-coupling capacitor should be investigated for use in future revisions of the detector panel design. The AC-coupled scheme routes the dark current directly to ground, and blocks all DC components of the SiPM output from the preamplifier input, eliminating the DC offset and significantly reducing noise. In combination with using more recent SiPM models covering one of the 15 x 8 mm^2 sides, the AC bias scheme should allow the detector panels to achieve a lower energy threshold, and thus increased radiation detection sensitivity.

5.2.2   Articulation Array

Though the articulation array designed and used in this work is perhaps the simplest design, it could be made more vertically compact through the use of gears. Helical gears, specifically, could be used most effectively with a central drive shaft since a central gear could be used to turn a gear on each panel at a right angle of rotation. Such a design is illustrated in Figure 5.1, where item 104 is the central helical gear, and items 105 are the panel helical gears.
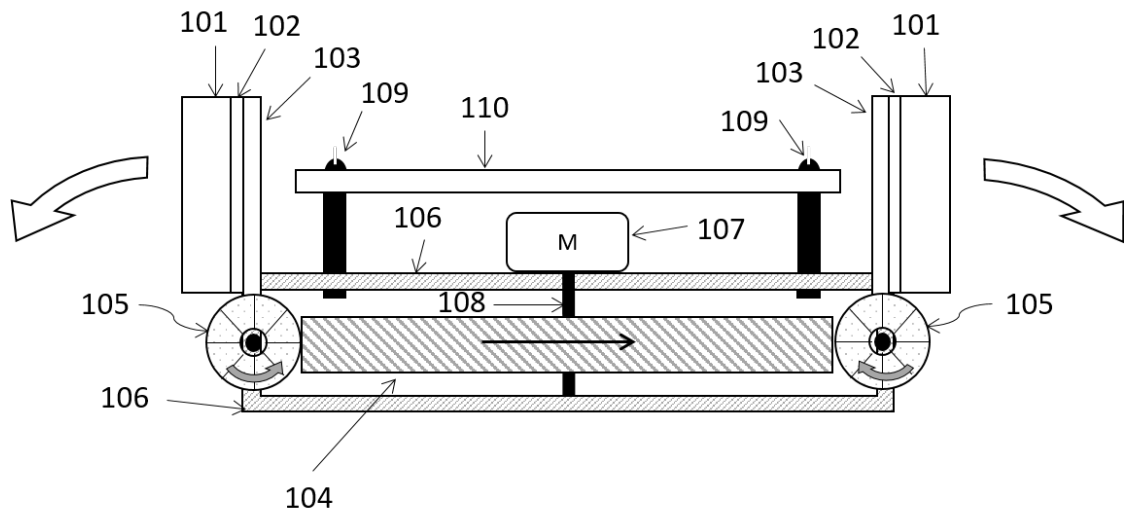
Figure 5.1: Illustration of the helical-gear design for the articulation platform [72].

Also seen in Figure 5.1 as item 107 is stepper motor that would ideally be used to rotate the central helical gear. The stepper-motor would be required for the articulation platform's use on an unmanned aerial vehicle. The stepper motor should be lightweight and low power, and would be used in a coordinated fashion with the unmanned vehicle's flight controller and the search algorithm.

The articulation platform would be bolted to the bottom of the UAV chassis by the articulation plate. The UAV landing struts would need to set the chassis off the ground high enough to avoid letting the articulation platform hit the ground when landed. Using the more compact helical gear design would reduce the height required of the landing struts.

5.2.3 System Development

The final stage of the project would be the development of the complete radiological search system, complete with UAV, Radiation Compass, and a compact, low-cost, lightweight gamma ray spectrometer. A revised version of the digital counting module would need to be designed and assembled that would ideally be integrated into the UAV flight controller. An alternative would be to implement the FPGA firmware and Matched Filter method in the UAV flight controller or separate microcontroller, though parallel inputs would be required in order to accurately tally the comparator pulses from the detector panels.

A low-power, low-cost, compact, lightweight gamma spectrometer prototype has previously been developed at Oregon State University [73] and is well-suited for use as the spectrometer in the complete radiological search system design. The prototype weighed 340 g, including the wireless network card, which would not be necessary in the radiological search system, and was 63.5 x 38.1 mm^2. It used a 6 x 6 x 10 mm^3 CsI(Tl) crystal coupled to a single SiPM, as well as a FPGA-based digital pulse processor, and was able to achieve 5.9% FWHM energy resolution at 662

keV. Long-distance wireless communication with the spectrometer, the Radiation Compass, and the UAV could be facilitated by small, lightweight modules such as the Xbee [74].

Finally, field trials using the complete system would be undertaken to assess the system performance in finding point sources, distributed sources, and contaminated fields. The results of these trials would be revision of search algorithms and detector design incorporating the dynamic nature of the system and optimizing for source localization efficincy and speed. The system should be tested in a variety of environments, varying from struture-less fields to urban areas to assess its performance and usefulness in various radiological search scenarios.

Bibliography

[1] Aerial Measuring System. `http://www.nnsa.energy.gov/aboutus/ourprograms/emergencyoperationscounterterrorism/respondingtoemergencies-0-0`. Accessed: November 16, 2015.

[2] Radiological Assistance Program. `http://www.nnsa.energy.gov/aboutus/ourprograms/emergencyoperationscounterterrorism/respondingtoemergencies/firstresponders-0`. Accessed: November 16, 2015.

[3] Nuclear Emergency Support Team (NEST). Technical report, 2013. Accessed: November 16, 2015.

[4] Emergency Response. `http://www.nnsa.energy.gov/aboutus/ourprograms/emergencyoperationscounterterrorism`. Accessed: November 16, 2015.

[5] Nuclear Security. `http://www.dhs.gov/topic/nuclear-security`. Accessed: November 16, 2015.

[6] F N Flakus. Detecting and measuring ionizing radiation - a short history. *IAEA Bulletin*, 23(4):31–36, December 1982.

[7] R Hofstader. Alkali Halide Scintillation Counters. *Physical Review*, 74(1):100–101, May 1948.

[8] G F Knoll. *Radiation Detection and Measurement*. John Wiley & Sons, Hoboken, USA, third edition, 2000.

[9] R B Murray and F J Keller. Recombination Luminescence from Vk Centers in Potassium Iodide. *Physical Review*, 137(3A):942–948, February 1965.

[10] J T Randall and M H F Wilkins. Phosphorescence and electron traps I. The study of trap distributions. *Proceedings of the Royal Society of London A*, 184(999):365–389, November 1945.

[11] R McIntyre. Theory of Microplasma Instability in Silicon. *Journal of Applied Physics*, 32(6):983–995, November 1961.

[12] R Haitz. Model for the Electrical Behavior of a Microplasma. *Journal of Applied Physics*, 35(5):1370–1376, November 1964.

[13] D Renker. Geiger-mode avalanche photodiodes: history, properties and problems. *Nuclear Instruments and Methods A*, 567(1):48–56, November 2006.

[14] S Vasile. High Gain Avalanche Photodiode Arrays for DIRC Applications. *IEEE Transactions on Nuclear Science*, 46(4):848–852, August 1999.

[15] J Ninkovic. Recent developments in silicon photomultipliers. *Nuclear Instruments and Methods A*, 580(2).

[16] B Dolgoshein V Balagura, P Buzhan, M Danilov, L Filatov, E Garuttic, M Grolle, A Ilyina, V Kantserova, V Kaplina, A Karakasha, F Kayumova, S Klemind, V Korbelc, H Meyerc, R Mizukb, V Morgunovb, E Novikovb, P Pakhlovb, E Popovaa, V Rusinovb, F Sefkowc, E Tarkovskyb, and I Tikhomirov. Status report on silicon photomultiplier. *Nuclear Instruments and Methods A*, 563(2):368–376, July 2006.

[17] V Saveliev and V Golovin. Silicon avalanche photodiodes on the base of metal-resistor-semiconductor (MRS) structures. *Nuclear Instruments and Methods A*, 442(1):223–229, March 2000.

[18] M McClish, P Dokhale, J Christian, C Stapels, and K S Shah. Characterization and scintillation studies of a solid-state photomultiplier. *Nuclear Instruments and Methods A*, 572(3):1065–1070, 2007.

[19] A G Stewart, V Saveliev, S J Bellis, D J Herbert, P J Hughes, and J C Jackson. Performance of 1-mm^2 Silicon Photomultiplier. *IEEE Journal of Quantum Electronics*, 44(2):157–164, March 2008.

[20] E Rutherford. *Radio-activity*. Cambridge University Press, London, UK, 1904.

[21] R M Keyser and T R Twomey. Performance of a Radiation Portal Freight Monitor based on Integrated Germanium Detector Modules. Institute of Nuclear Materials Management 2010 Annual Meeting, 2010.

[22] H3D, Ann Arbor, MI. *Polaris-H Gamma-Ray Imaging Spectrometer*. Accessed: November 16, 2015.

[23] C E Lehner, Z He, and F Zhang. 4π Compton Imaging Using a 3-D Position-Sensitive CdZnTe Detector Via Weighted List-Mode Maximum Likelihood. *IEEE Transactions on Nuclear Science*, 51(4):1618–1624, August 2004.

[24] W Wang, W R Kaye, J Kim, F Zhang, and Z He. Improvement of Compton imaging efficiency by using side-neighbor events. 2010 IEEE Nuclear Science Symposium Conference Record, 2010.

[25] R B Vilim and R T Klann. Source localization using multiple units of a tight-pitched detector array, 2015.

[26] R Vilim and R Klann. RadTrac: A System for Detecting, Localizing, and Tracking Radioactive Sources in Real Time. *ANS Nuclear Technology*, 168(1):61–73, October 2009.

[27] R Vilim, R Klann, S C de la Barrera, P L Vilim, and I A Ross. Tracking of weak radioactive sources in crowded venues. 2009 IEEE Nuclear Science Symposium Conference Record, 2009.

[28] Radmap rollout. `http://engineering.berkeley.edu/magazine/spring-2013/radmap-rollout`, 2013. Accessed: November 16, 2015.

[29] K Vetter. Multi-sensor radiation detection, imaging, and fusion. *Nuclear Instruments and Methods A*, 805:127–134, January 2016.

[30] T Aucott, M S Bandstra, V Negut, D H Chivers, R J Cooper, and K Vetter. Routine Surveys for Gamma-Ray Background Characterization. *IEEE Transactions on Nuclear Science*, 60(2):127–134, April 2013.

[31] T Aucott, M S Bandstra, V Negut, J C Curtis, D H Chivers, and K Vetter. Effects of Background on Gamma-Ray Detection for Mobile Spectroscopy and Imaging Systems. *IEEE Transactions on Nuclear Science*, 61(2):127–134, April 2014.

[32] L E Sinclair, R Fortin, and F A Marshall. Reconstruction of the Spatial Distribution of Radioactive Contamination from Aerial and Directional-Truckborne Survey. 2015 IEEE Nuclear Science Symposium, 2015.

[33] S E Cook, R J Corner, P R Groves, and G J Grealish. Use of airborne gamma radiometric data for soil mapping. *Australian Journal of Soil Research*, 34(1):183–194, 1996.

[34] E A Miller, S M Robinson, K K Anderson, J D McCall, A M Prinke, J B Webster, and C E Seifert. Adaptively Reevaluated Bayesian Localization (ARBL): A novel technique for radiological source localization. *Nuclear Instruments and Methods A*, 784(1):332–338, June 2015.

[35] D Hanna, L Sagineres, P J Boyle, and A M L McLeod. A directional gamma-ray detector based on scintillation plates. *Nuclear Instruments and Methods A*, 797(1):13–18, 2015.

[36] J C Farmer. Surface with two paint strips for detection and warning of chemical warfare and radiological agents, 2013.

[37] J G Barnes and T R Austin. Aircraft having an integrated radiation detection system and method therefor, 2011.

[38] J G Barnes and T R Austin. Unmanned underwater vehicle integrated radiation detection system, 2013.

[39] A Zoglauer, M Galloway, M Amman, P N Luke, and S E Boggs. Aerial Standoff Detection with the High Efficiency Multimode Imager (HEMI). 2010 IEEE Nuclear Science Symposium Conference Proceedings, 2010.

[40] Imitec. `http://imitec.co.uk/`, 2014. Accessed: November 16, 2015.

[41] J W MacFarlane, O D Payton, A C Keatley, G Scott, H Pullin, R A Crane, M Smilion, I Popescu, V Curlea, and T B Scott. Lightweight aerial vehicles for monitoring, assessment and mapping of radiation anomalies. *Journal of Environmental Radioactivity*, 136:127–130, October 2014.

[42] P G Martin, O D Payton, J S Fardoulis, D A Richards, Y Yamashiki, and T B Scott. Low altitude unmanned aerial vehicle for characterising remediation effectiveness following the FDNPP accident. *Journal of Environmental Radioactivity*, 151:58–63, January 2016.

[43] R Ballard. *Archaeological Oceanography*. Princeton University Press, Princeton, USA, 2008.

[44] Mars Exploration Rovers. `http://mars.jpl.nasa.gov/mer/overview/`. Accessed: November 16, 2015.

[45] Meet DARPAs WildCat: A free-running quadruped robot that will soon reach 50 mph over rough terrain. `http://www.extremetech.com/extreme/168008-meet-darpas-wildcat-a-free-running-quadruped-robot-that-will-soon-re`, 2013. Accessed: November 16, 2015.

[46] Global Hawk. `http://www.northropgrumman.com/Capabilities/GlobalHawk/Pages/default.aspx?utm_source=PrintAd&utm_medium=Redirect&utm_campaign=GlobalHawk+Redirect`, 2015. Accessed: November 16, 2015.

[47] Rotary Wing Vs Fixed Wing UAVs. `http://www.uavinsider.com/rotary-wing-vs-fixed-wing-uavs/`, 2013. Accessed: November 16, 2015.

[48] How GPS works. `http://www.gps.gov/multimedia/poster/`, 2013. Accessed: November 16, 2015.

[49] S Bertrand, J Marzat, M Carton, C Chaix, P Varela, R Waroux, G DeFerron, and R Laurel. A low-cost system for indoor motion tracking of unmanned aerial vehicles. 2011 Seventh International Conference on Intelligent Sensors, Sensor Networks and Information Processing, 2011.

[50] W Burgard, C Stachniss, K Arras, and Maren Bennewitz. Introduction to Mobile Robotics: SLAM: Simultaneous Location and Mapping. `http://ais.informatik.uni-freiburg.de/teaching/ss12/robotics/slides/12-slam.pdf`, 2014. Accessed: November 16, 2015.

[51] SensL. *B-Series: Fast, Blue-Sensitive Silicon Photomultiplier Sensors*, 2013. Accessed: September 10, 2013.

[52] Saint-Gobain. *BGO Bismuth Germanate Scintillation Material*, 2014. Accessed: November 16, 2015.

[53] Materials Index: Bismuth Germanate ($Bi_4Ge_3O_{12}$). `http://www.hilger-crystals.co.uk/materials-index/bismuth-germanate.html`, 2014. Accessed: November 16, 2015.

[54] EGX-350 Desktop Engraver. `http://www.rolanddg.com/product/3d/sculpture/egx-350/spec.html`, 2015. Accessed: November 16, 2015.

[55] Saint-Gobain. *Detector Assembly Materials*, 2014. Accessed: November 16, 2015.

[56] Blackout Materials. `http://www.thorlabs.us/newgrouppage9.cfm?objectgroup_id=190`, 2015. Accessed: November 16, 2015.

[57] SolidWorks. `http://www.solidworks.com/`, 2015. Accessed: November 16, 2015.

[58] Makerbot Replicator 2. `https://store.makerbot.com/replicator2.html`, 2015. Accessed: November 16, 2015.

[59] Makerbot PLA Filament. `https://store.makerbot.com/filament/pla`, 2015. Accessed: November 16, 2015.

[60] Opal Kelly. *XEM6001 Users Manual*, 2015. Accessed: September 10, 2015.

[61] MATLAB. `http://www.mathworks.com/products/matlab/?refresh=true`, 2015. Accessed: November 16, 2015.

[62] I G Myung. Tutorial on Maximum Likelihood Estimation. *Journal of Mathematical Psychology*, 47(1):90–100, February 2003.

[63] R Vilim, R Klann, and J Thomas. Integrated Treatment of Detector Arrays for Source Tracking. *Nuclear Technology*, 175(1):314–325, July 2011.

[64] D O North. An analysis of the factors which determine signal/noise discrimination in pulsed-carrier systems. *Proceedings of the IEEE*, 51(7):1016–1027, 2016.

[65] A Oppenheim and G Verghese. Signals, Systems and Inference. `http://ocw.mit.edu/courses/electrical-engineering-and-computer-science/6-011-introduction-to-communication-control-and-signal-processing-spring-20 readings/MIT6_011S10_chap14.pdf`, 2010. Part of MIT Open Courseware, Ch 14.

[66] Monte Carlo Code Group. `https://mcnp.lanl.gov/`, 2010. Accessed: November 18, 2015.

[67] Chart of Nuclides. `http://www.nndc.bnl.gov/chart/`. Accessed: November 25, 2015.

[68] H Stark and J Woods. *Probability, Statistics, and Random Processes for Engineers*. Prentice Hall, Upper Saddle River, USA, fourth edition, 2011.

[69] L A Currie. Limits for qualitative detection and quantitative determination, application to radiochemistry. *Analytical Chemistry*, 40(3):586–593, March 1968.

[70] SensL. *C-Series: Low-Noise, Fast, Blue-Sensitive Silicon Photomultiplier Sensors*, 2014. Accessed: November 29, 2015.

[71] SensL. *J-Series: High-Density Fill Factor Silicon Photomultipliers*, 2015. Accessed: November 29, 2015.

[72] A T Farsoni and E M Becker. A system and method for locating radiation sources, 2015. PCT Patent Application No. PCT/US2015/027622.

[73] E M Becker and A T Farsoni. Wireless, low-cost, FPGA-based miniature gamma ray spectrometer. *Nuclear Instruments and Methods A*, 761(11):99–104, October 2014.

[74] Xbee: Connect devices to the cloud. `http://www.digi.com/lp/xbee`. Accessed: November 28, 2015.